Degree of Doctor of Philosophy in
Electronics and Telecommunications

Doctorate School in
Information and Communication Technologies

XXV Cycle

University of Modena and Reggio Emilia

Department of Engineering "Enzo Ferrari"

Ph.D. Dissertation

Hollow core fibers for terahertz applications

Candidate:
Valerio Setti

Advisor:
Prof. Luca Vincetti

The Director of the School:
Prof. Giorgio Matteo Vitetta

Dottorato di Ricerca in
Electronics and Telecommunications

Scuola di Dottorato in
Information and Communication Technologies

XXV Ciclo

Universita' Modena e Reggio Emilia

Dipartimento di Ingegneria "Enzo Ferrari"

Tesi per il conseguimento del titolo di dottore di ricerca

Fibre a nucleo cavo per applicazioni nella gamma dei terahertz

---

Candidato: Valerio Setti

Relatore: Prof. Luca Vincetti

Il Direttore della Scuola: Prof. Giorgio Matteo Vitetta

Abstract

This thesis concerns with the development of a low loss, broadband and flexible waveguide for terahertz (0.1 THz - 10 THz) applications. In recent years THz sources and detectors have undergone a great development thus suggesting an increasing number of possible applications, such as imaging or sensing. However, the lack of a broadband low-loss waveguide preclude real implementations. Classical metal or solid core waveguides can not be used for this purpose, owing to the limited conductivity of metals and the prohibitively high absorption of dielectrics in the THz range. Since air is one of the most transparent dielectrics for the THz radiation, many innovative fibers designs have been proposed in the literature with the goal to maximize the amount of field that propagates in air at the expense of that in the dielectric. In this sense hollow core waveguides offer an interesting solution because a high percentage of the THz radiation is confined in an airy core.

The fiber proposed in this thesis is an hollow core fiber whose cladding is based on a lattice of dielectric tubes. Since only one turns of tubes around the core is enough to give reasonably low leakage loss, the whole structure is also very compact ($<$ 1 cm for the overall diameter) and potentially flexible. This strongly simplifies the manufacturing of the fiber: no stack and draw process is required and the whole waveguide can be assembled manually starting from the stand alone cladding tubes.

In order to improve the fibers performances in terms of low propagation loss and wide transmission bandwidths, a theoretical analysis of the confinement is given first. A new theoretical model able to predict fiber's transmission properties is

proposed. It is based on the observation that the spectral properties of the microstructured fiber can be derived from those of the cladding tubes. Since tube waveguides can be described analytically, this model allows to determine how the geometrical and physical features of the microstructured cladding affect the spectral behavior of the whole waveguide. General guidelines for the design of this kind of fibers are then given.

Perturbations to the ideal structure are then investigated in order to evaluate their effect on the performance of the fiber. Since very often cladding tubes are obtained from a previous drawing process, shape alterations are considered first. It is shown that the circular case allows to obtain wider transmission bandwidths and lower losses, suggesting that the drawing process of the tubes must be carefully controlled. Other perturbations, such as elliptical core shapes or bending are also taken into account. The former is of key importance for most of the proposed THz applications since they are based on the propagation of pulses with unknown polarizations. Core's ellipticity may cause undesired echoes in the system thus compromising performances. Also bending loss plays a central role in most of the THz setups since flexible waveguides are required. Through a detailed numerical analysis it is shown that the proposed fiber is actually strongly robust against both of these kind of perturbations.

Finally, manufacturing and characterization of two different kind of microstructured waveguides is shown, starting from polymethylmethacrylate and Zeonex tubes, respectively. The whole structure is assembled manually and, thanks to the its self sustain feature, no gluing or further drawing steps are required. An heat-shrink tube is used for the jacket in order to preserve the flexibility of the fiber. Experimental data for the straight case confirm that propagation loss is strongly reduced with respect to the absorption of the bulk material used in the cladding. For example, a 31 and 272 times reduction at 0.375 and 0.828 THz respectively is shown for the PMMA case, giving propagation loss of 0.3 dB/cm and 0.16 dB/cm. Bending characterization confirms that this waveguide can be used in a real flexible THz setup with bending radii down to few tenth of centimeters without any visible reduction of the transmission spectrum.

Contents

Chapter 1

Introduction

1.1 Terahertz: applications and devices

The terahertz (THz) spectral range includes all the waves with a frequency that range from 0.3 THz to 3 THz (tera = 10^{12}), which correspond to wavelengths of $[1 - 0.1]$ mm. Falling in between microwave and infrared spectral regions, it shares features with both of them. On one hand the working wavelength is reasonably small so that THz waves can be used for imaging down to sub millimeter resolutions. On the other hand, photon energy (E_p) is extremely low ($E_p < 12.4$ meV when $f < 3$ THz) which means that the THz radiation can be used safely without any concern about the ionization of the sample. These features make THz technologies very interesting for high resolution imaging both for industrial and biological applications, such as those shown in Figs. 1.1 (a) and (b).

Likewise microwave radiation, THz waves can also penetrate many non conducting materials, even though the penetration depth is smaller. Moreover, dielectric materials exhibit very different absorption spectra and refractive indices in the THz range, which makes it possible to identify them through a simple transmission or reflection analysis. These features can be used for both the identification of unknown materials and security purposes, as shown in Fig. 1.1 (c).

Being above the microwave spectral region, potential applications for the THz radiation include also high frequency and broadband communications. Unfortu-

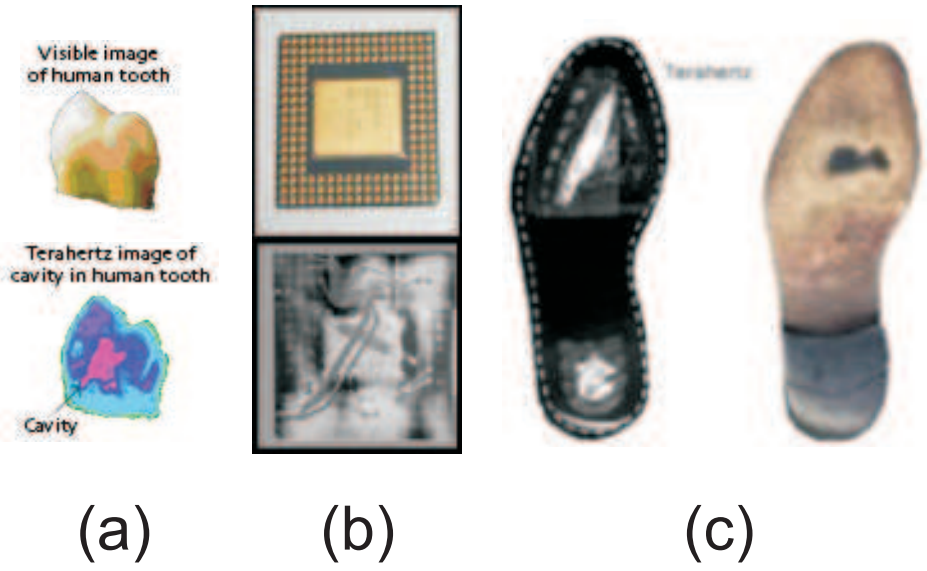

Figure 1.1: Comparison between the visible and THz image of a human tooth (a), bottom side of an integrated circuit device (b) and a ceramic knife hidden inside a shoe (c) . All the images belong to TeraView Ltd. (www.teraview.com).

nately THz waves are strongly absorbed from the water vapor which is present in the earth's atmosphere as shown in Fig. 1.2, thus limiting long range transmissions. However, THz networks can be profitably used for short distance or satellite broadband communications.

Of course, all these possible scenarios, rely on proper sources and detectors for the THz radiation. Despite of being in the middle between microwaves and infrared spectral regions, both frequency multiplication and lasers suffer from strong limitations for the THz spectral range due to their physical characteristics [1]. On one hand, frequency multiplication generally starts from a sinusoidal source at a few tenth of gigahertz (giga = 10^9), which is then frequency multiplied though non-linear devices. However, the output power rapidly decreases as the initial signal passes through the various stages, giving a very weak output signal and limiting the maximum working frequency to a few hundreds of GHz [2]. Classic lasers, on the other hand, can not be used owing to the very low photon energy which is required for THz generation. Owing to the fact that E_p must be

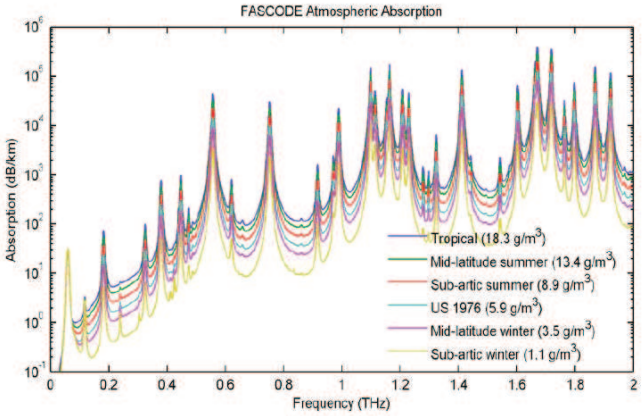

Figure 1.2: Atmosphere's absorption spectrum measured on different places of earth. Peaks are due to water vapor absorption. This graph belongs to Zomega Terahertz Corp. (www.zomega-terahertz.com).

higher than E_{BG} (where E_{BG} is the bandgap energy of the laser's semiconductor) this imposes strong limits on both the semiconductor that can be used and the working temperature as well. Indeed, with such small E_{BG}, at room temperature the thermal energy of the atoms in the system is enough to destroy all the population inversion in the active region of the laser substrate. Even though quantum cascade lasers have been proposed in the literature as an improvement of classic laser sources allowing for the generation of electromagnetic radiation at (virtually) any desired frequency, they are still limited to extremely low working temperatures (below 100 K) in the THz range [3, 4].

For this reasons many new devices have been developed specifically for the THz spectral region, such as photoconductive antennas [5–7], four wave mixing devices [8–11], Raman based molecular modulation devices [12], resonant diodes [13, 14], just to cite a few.

Photoconductive antennas are widely used in THz Time Domain Spectroscopy (THz-TDS) setups for the characterization of bulk materials [15], waveguides [16, 17] and innovative devices [18]. Dealing with the generation of pulses, they are very interesting as sources because they allow a broadband (a few THz in general) characterization of the samples with both phase and amplitude informa-

tion. Therefore these kind of antennas are used in chapter 6 to characterize an hollow core waveguide.

1.2 Terahertz waveguides

All these improvements in both THz sources and detectors allow for a broadband and reasonably high power generation and detection of THz radiation. However, one of the main problems that still limits the application of these technologies is the absence of a low loss waveguide with broadband features. Being the THz spectral region in the middle between the microwave and the infrared one, former setups were based on either metal waveguides or solid core fibers. However, these classical waveguides can not be used for this purpose, owing to the limited conductivity of metals and the absence of highly transparent dielectrics in the terahertz range. For example, polymethylmethacrylate, which a polymer commonly used for the fabrication of solid core fibers in the infrared spectral region [19], has an absorption rate of 100 dB/cm at 1 THz [20]. Even Zeonex or Topas, which are two of most transparent dielectrics in the THz range, have absorptions rates of 1.81 and 1 dB/cm respectively at 1 THz [16, 20]. On the other hand, metals at THz frequencies strongly reduce their conductivity with respect to their low-frequency values [21, 22]. Aluminum, for example, which is supposed to be a good conductor at low frequencies, almost halves its conductivity in the THz range. This means that if two aluminum waveguides with identical wavelength to core size ratios are taken into account, one for microwaves frequencies and one for THz, the latter will have propagation loss roughly 17 dB/m higher than the former [23].

Since air is one of the most transparent dielectrics in the terahertz spectral region, former setups were based on free space propagation. This solution strongly limits the flexibility of the setup and makes the system extremely sensitive to the surrounding environment. Despite these problems, this suggested new ways for the design of terahertz waveguides: increase the amount of field power that propagates in air.

1.2.1 Improvement of classical metal waveguides

First attempts rely on either the partial removal of the dielectric layer in solid core fibers or its complete removal in metal waveguides. Parallel plates waveguides with air between the two metal electrodes represent an example of this improvement. Even though this solution brings some interesting features, such as zero pulse dispersion or sub-wavelength core size [24], there are various drawbacks that must be taken into account. First of all the absence of a dielectric material between the two metal electrodes strongly limits the mechanical stability of the structure, thus limiting the maximal length of the waveguide to few centimeters. Moreover, the absence of field confinement in both transverse directions, allow for extra propagation losses due to field divergence [25]. Solutions to overcome this problem have been proposed, such as slightly concave parallel plates [25], however these are generally optimized for a specific frequency (even though improvements extends to some hundreds of GHz).

Another important limitation of all metal waveguides is the high rigidity of the structure, which prevent their application in flexible THz setups. Solutions to this problem have been proposed in the literature based mainly on single or multi metal wires waveguides [26–29]. Even though single wire waveguides allow a potentially low propagation loss (in the order of 0.26 dB/cm at 0.3 THz [26]), they suffer from a very low coupling efficiency, high bending loss and extremely high sensitivity to the surrounding environment [26, 30]. Bending capabilities are partially improved in two or multi-wire waveguides. In general they are an interesting solution for low loss waveguiding in the lower part of the THz spectrum, but their losses rapidly increase with frequency [29, 31]. Even in this case, a dielectric sustain must be considered to guarantee the mechanical stability of structure, thus increasing propagation loss due to dielectric's absorption. Innovative designs have been proposed in which the dielectric material within the metal wires is replaced with air in order to limit absorption effects [28, 29].

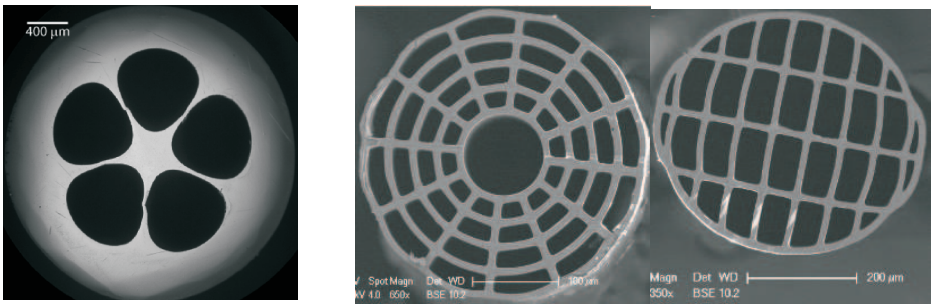

Figure 1.3: (a) Cross section of the suspended core fiber proposed in [16]. (b) Cross section of two porous fibers proposed in [34].

1.2.2 Improvement of classical solid core dielectric waveguides

Various improvements have been proposed also for solid core fibers. Former solutions for step index fibers tried to use air as the external cladding while increasing the amount of evanescent field propagating outside the core [32]. However, these microwires are strongly limited by the absorption of the dielectric material used in the rod core. Slight improvements can be obtained by using a core size which is much smaller than the working wavelength. However this cause the guided mode to have a large spatial extension in the transverse direction thus giving an extremely high sensitivity to the surrounding environment and high bending loss.

A possible solution to this problem is given by suspended core fibers [16, 33], whose typical structure is shown in Fig. 1.3 (a). In this case the rod core is suspended in the middle of an external hollow core tube by means of very thin dielectric struts. The main advantage of the external tube is the reduction of the sensibility to the surrounding environment. However, performances of suspended core fibers are still limited by the absorption of the dielectric material.

Porous fibers have also been proposed in the literature as a possible way to overcome the dielectric absorption [34, 35]. Some structure examples are shown in

Fig. 1.3 (b) for clearness. Their structure is very similar to the step-index fibers shown above, but in this case some airy regions are introduced in the core. Total internal reflection is still the confinement mechanism, but in this case the overlap with the dielectric material and, thus, the absorption are much reduced. However, the airy regions inside the core area, introduce an effective refractive index for the core which is generally much lower than that of the dielectric material used. As a consequence, the guided core mode is not tightly confined in the core region, making it highly sensitive to both the surrounding environment and to bend induced losses [33].

1.2.3 Hollow core fibers

In recent years hollow core waveguides have been proposed as a very promising solution for low propagation loss waveguiding in the terahertz range. Differently from the waveguides shown in the previous section, in these fibers the core region is made of air and only the cladding region is built from dielectric materials. Since the electromagnetic radiation is strongly inside the hollow core region, only a negligible amount of it overlaps with the dielectric material in the cladding and, therefore, absorption is strongly reduced. However, being the core refractive index lower than the cladding one, total internal reflection can not be used as a confinement mechanism for the electromagnetic radiation. Two different confinement mechanism have been proposed in the literature to overcome this problem: photonic band gap (PBG) or inhibited coupling (IC). It must be noticed, however, that for both of these mechanisms the confinement of the electromagnetic radiation inside the core region is not perfect [36]. Therefore, hereinafter propagation loss will be composed by two terms:

- absorption loss, which is due to the dielectric materials used in the waveguide (as for classical waveguides);
- leakage loss, which accounts for the power radiated out of the waveguide due to the non perfect confinement of the electromagnetic radiation inside the core region.

PBG is based on a periodic arrangement of the refractive index in the cladding in such a way to obtain a frequency dependent core-cladding reflection for the electromagnetic radiation that is confined inside the hollow core [37, 38]. By adjusting the geometrical and physical parameters of the cladding it is possible to have an almost perfect confinement of the THz radiation inside the hollow core. However, in general, this can be achieved only for narrow frequency regions, thus limiting the transmission bandwidths that can be achieved [39]. Moreover, in order to achieve the band gap effect for the guided core mode, the fundamental lattice that constitute the cladding needs to be repeated several times. This limits the minimum overall size that can be achieved for the waveguide, thus compromising its flexibility and its applications in THz setups [40].

Since most of the applications proposed for the terahertz range require wide transmission bandwidths and flexibility, most of the waveguides that have been proposed in the literature rely on the IC confinement mechanism. As it will be shown in the following chapters, it is based on the coupling between the core mode itself and the cladding modes. Many different structures have been proposed in the literature ranging from the stand alone tube waveguides [41–44] to microstructured fibers [17, 45, 46]. Being the structure of the stand alone tube waveguide extremely simple, their main advantage is that they can be easily obtained with drawing processes starting from drilled cylindrical preforms. The main limitation of these waveguides is that the electromagnetic radiation is not tightly bounded inside the core so they suffer of higher leakage loss compared to the inhibited coupling fibers shown in the next section with the same core size [47]. Larger core dimensions are required for low loss but these cause many high order modes to propagate inside the hollow core [44]. In order to overcome this problem, metallic coatings were proposed [41]. However complex depositions techniques are required in order to obtain very thin metallic layers so as to not affect the flexibility of the final structure.

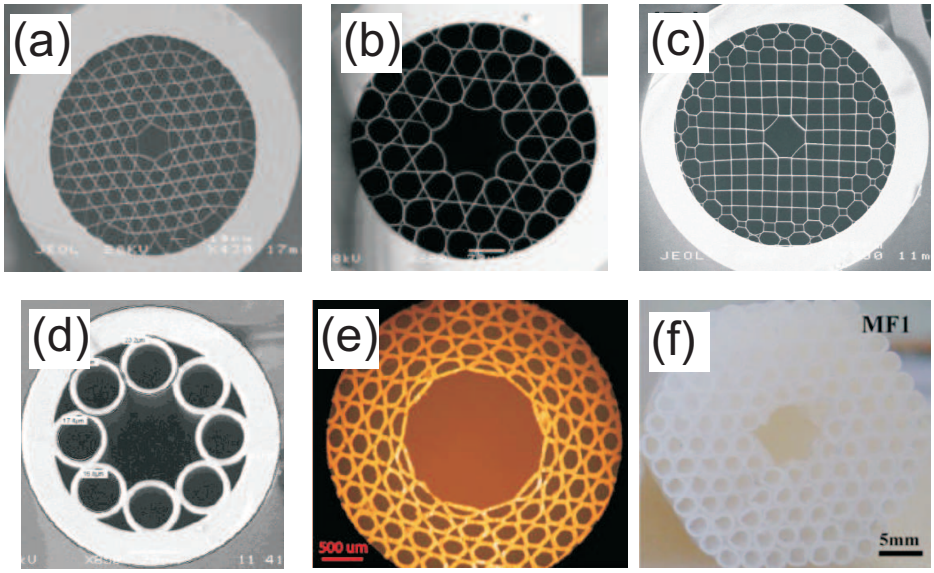

Figure 1.4: Examples of kagome (a,b) [36, 46], square lattice (c) [50] and circular tube lattice (d) [51] fibers for the visibile/IR spectral regions. A kagome (e) [17] and a triangular tube lattice fiber (f) [52] for the THz range.

1.3 Inhibited coupling hollow core fibers

Inhibited coupling hollow core fibers offer an interesting solution to the problems mentioned above. The higher confinement of the electromagnetic radiation inside the hollow core with respect to the stand alone tubes allows a smaller core size to be taken into account and it makes the guided core mode less sensitive to the surrounding environment [17, 36, 45, 46].

These kind of fibers were first introduced for the visible and infrared (IR) spectral regions [36, 48–50]. Their claddings are more complex and, in general, they are obtained from multiple drawing steps, with the so called stack-and-draw technique. Some typical structures are shown in Figs. 1.4(a), (b) and (c). Depending on the pattern with which the tubes are arranged to form the microstructured cladding, two different structures were proposed:

- kagome fiber, obtained from a triangular displacement of the tubes [36, 48];

- square lattice fibers [49, 50].

Due to the surface tension during the drawing step, in both cases circular shape of the cladding tubes is lost and the final claddings seem to be be formed by an intersection of slab dielectric waveguides.

Their transmission spectra are formed by a periodic alternation (in frequency) of high and low transmission regions. Due to the cladding shape, former theoretical models tried to investigate the confinement mechanism of these fibers by modeling the cladding as an intersection of simple dielectric slabs [49], which are well known in the literature. The main limitation of these models was that, even though they were able to predict the spectral position of the high loss regions, they were unable to justify and predict the spectral width of these high loss regions.

Kagome fibers have recently been proposed also for the terahertz spectral range [17] and its structure is shown in Fig. 1.4(e). Obviously, owing to the larger working wavelength of the THz spectral region with respect to the IR one, bigger core sizes were required to guarantee reasonable leakage loss values. As a consequence, in [52] it was shown that microstructured fibers based on a triangular lattice of tubes can be assembled manually without any further drawing step. The final structure, named tube lattice fiber (TLF) hereinafter, is reported on Fig. 1.4(f). It is very similar to the kagome one proposed for the IR, but in this case the circular shape of the cladding tubes was preserved.

The purpose of this thesis is to investigate the spectral properties of these hollow core fibers in order to define general design rules for a low loss and broadband waveguiding in the THz spectral range. Therefore, in chapter 2 the confinement mechanism of TLFs is investigated. It is shown that the properties of the whole microstructured cladding can be inferred from those of the single tubes that constitute the cladding. Since the stand alone tube is well known in the literature [53, 54], this greatly simplifies the development of a theoretical model for the waveguiding mechanism.

Recently, a very similar hollow core fiber (see Fig. 1.4(d)) has also been proposed in the literature for the IR spectral range in which the cladding is composed by a

circular arrangement of circular tubes around the hollow core [51]. In that paper it is suggested that its confinement mechanism can be analyzed by means of the scattering of a plane wave from a hollow tube. The model proposed in this thesis is absolutely equivalent and, at the same time, is also more general. In chapter 4, for example, it is shown that perturbations in the cladding tubes can easily been taken into account via a coupled mode theory. A similar analysis would be much harder to be analytically investigated with the model shown in [51].

In order to compare the performance of kagome and TLFs, in chapter 3 kagome fibers are modeled as a triangular lattice of hollow tubes with hexagonal shape. Both TLFs and kagome fibers are seen as belonging to the general family of TLFs in which the cladding is composed by a triangular lattice of polygonal tubes each of which has an arbitrary number of sides. It is shown that the propagation loss performance of the microstructured fiber are highly sensitive to the shape of the tubes used in the cladding and that the circular case allows to obtain better performance in terms of both minimum propagation loss and transmission bandwidth.

In order to understand the causes of higher loss in kagome fibers with respect to TLFs, in chapter 4 a thorough numerical and theoretical analysis of TLFs with polygonal tubes in the cladding is proposed. As for the analysis of TLFs in chapter 2, also in this case the investigation starts with the study of the spectral properties of the stand alone polygonal tube and the comparison with its circular counter part. It is shown that the polygonal shape is extremely detrimental causing extra loss peaks in the confinement loss spectrum of the guided core modes. By using coupled mode theory and by viewing the polygonal shape as a perturbation of the ideal circular one, a theoretical model is finally proposed which is able to predict the spectral position of these extra loss peaks. With similar analytical considerations, the same model is then extended also for the analysis of TLFs with polygonal cladding tubes. It proves that the higher propagation loss of kagome fibers with respect to TLFs is due to the hexagonal shape of the cladding tubes which causes a dense spectrum of undesired extra loss peaks over the entire transmission spectrum.

Chapter 5 is entirely dedicated to the analysis of perturbations in the TLFs, in particular:

- elliptical core shape,
- bending loss,
- confinement loss dependency on scaling.

Core ellipticity may be caused by a non perfect displacement of the cladding tubes around the hollow core during the manufacturing of the fiber. This is an important aspect especially for pulsed applications, such as THz time domain spectroscopy, since undesired echoes may appear at the output of the fiber thus compromising the performance of the system. However, numerical analysis shows that, in general, TLFs are not much sensitive to this kind of perturbation and only minimal differences in performance are found between the two polarizations of the fundamental mode are found.

Also the analysis of bending loss is extremely important for practical applications since the goal of this thesis is to propose a THz waveguide that should be used in dynamic setups. It is shown that the propagation loss of the guided core mode in TLFs is affected by two different effects during the bending: a reduction of the transmission window bandwidth and some extra loss peaks which appear for tight bending radii. A theoretical model is finally proposed in order to quantify both of these effects and to define the tolerance of the proposed TLFs to the bending in real applications.

All the theoretical models presented through this thesis are absolutely general and they are not limited to the THz range. This means that, through a proper geometrical scaling of the TLF's structure, the same fiber can be used also for other applications, such as visible or IR. Even though the confinement mechanism in not perturbed by the scaling, in general propagation loss changes. It is shown that, in general, the propagation loss of TLFs scale more rapidly than in kagome or other classic hollow core fibers.

Finally in chapter 6 a TLFs is manufactured starting from polymethylmethacrylate (PMMA) tubes and manually assembled. An external jacket made from an

heat shrink tube allows the final structure to be extremely flexible and mechanically stable. As a consequence both straight and bending characterizations are performed. For the straight case it is shown that the hollow core greatly reduces the propagation loss with respect to the absorption caused by PMMA. A 31 times reduction at 0.375 THz and 272 times reduction at 0.828 THz are obtained. In the bending characterization of the fiber's samples, bending radii down to 10 cm are reached. As expected from the numerical analysis of the previous chapters, a reduction of the transmission bandwidth appears in the bent fiber, but its effect is negligible in the first transmission window even for bending radii as tight as $R_b = 10$ cm. Moreover, also the second transmission window is highly immune to extra losses for bending radii down to $R_b = 30$ cm.

In conclusion, theoretical and experimental results reported on this thesis confirm that the tube lattice fiber proposed in this thesis can readily been used for THz applications. On one hand, all the various proposed guidelines allow for the design of a THz fiber with low propagation loss and broadband waveguiding features. On the other one, the manufacturing procedure proposed in chapter 6 allows to obtain a flexible structure which can be used in many practical THz setups, such as imaging or bending.

Most of the results shown in these thesis are taken from other author's publications in journals [55–61] and conferences [62–73].

Chapter 2

Waveguiding mechanism in Tube Lattice Fibers

The purpose of this chapter is to introduce to the inhibited coupling waveguiding mechanism in both the stand alone tube and in tube lattice fibers (TLFs). Despite the very different cladding shape, it will be shown that in both cases the confinement of the electromagnetic radiation inside the hollow core can be predicted by considering the coupling between the core and cladding modes: high loss regions are ascribable to high coupling conditions between these two modes. In order to formulate a theoretical model to predict the spectral behavior of both kind of fibers, it is thus necessary to have an analytical description for both core and cladding modes.

For the core modes, the analytical description given in [54] is used for both kind of waveguides since it is valid in general for an hollow core fiber. Cladding modes, on the contrary, are differentiated owing to the different geometries under analysis. For the stand alone dielectric tube cladding modes can be described analytically from the results shown in [53]. For the microstructured fiber, on the contrary, it is shown that the cladding modes can be approximated by a composition of those of the stand alone tube. This allows an accurate but also simple description of the cladding modes of the microstructured fiber.

Former models that have been proposed in the literature for the kagome and square lattice fibers approximate the cladding structure as an intersection of slab waveguides [36, 74]. Even though this solution greatly simplifies the analysis of the cladding modes, being able to predict the spectral position of high loss regions, it lacks any information about the spectral width of these high loss regions. Some improvements have been also been proposed in the literature, but they are mainly empirical [49] or numerical [46, 75–78].

On the contrary, the model proposed in this thesis is able to predict with high accuracy core modes' dispersion curves, spectral position and width of the high loss regions and conditions to ensure the existence of low loss spectral regions by simply starting from the properties of the tubes in the cladding. The same model is then finally used also used to improve the tradeoff between propagation loss and effectively single mode operation.

All the numerical analysis has been performed through a modal solver based on the finite element method (FEM) [79].

2.1 Circular tube fiber

The cross section of a *circular tube fiber* (CTF) is depicted in Fig. 2.1(a). r_{ext}, r_{int}, and t are external and internal radii and the thickness of the tube, respectively. The tube is made of dielectric material with refractive index n_H. Inside and outside the tube the medium is air with refractive index equal to $n_L = 1$. The analysis of the CTF is very important not only because it has been recently proposed as a simple and low loss THz waveguide [44, 80], but also because, as it will be shown later in this chapter, the dielectric modes of more complex microstructured hollow core fibers can be obtained directly by the modes of the single tube one.

In the CTF there are two different kind of confined modes: the modes here called "airy" in analogy with kagome lattice fibers [48], whose power is mainly confined inside the air core, and the "dielectric" modes, whose power is mainly located inside the dielectric. Since the effective index of the airy modes is lower than n_L

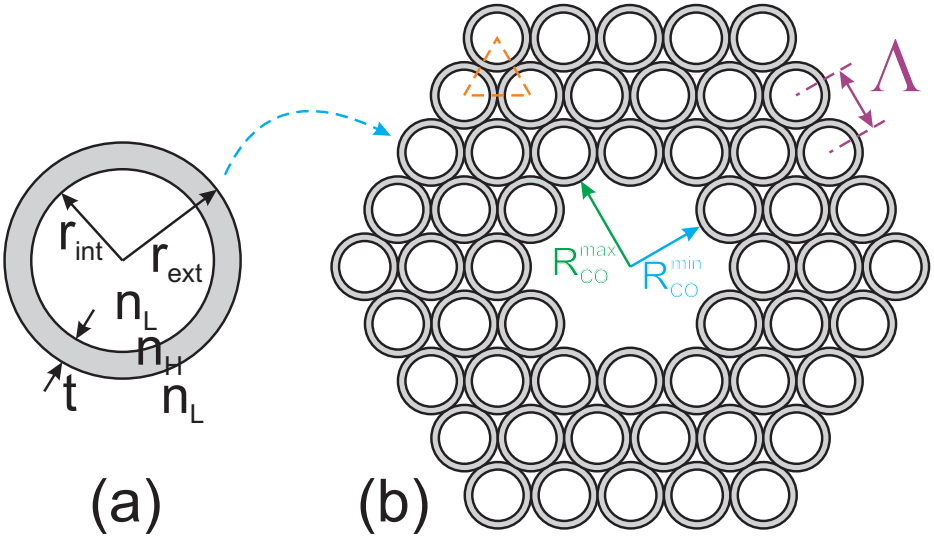

Figure 2.1: (a) Cross section of the stand alone tube waveguide along with its physical and geometrical parameters. (b) Cross section of a TTLF-CT with 3 rings tubes around the hollow core.

and the tube is surrounded by air, they are leaky. Modal intensity and electric field distributions of the lowest order modes are reported in Fig. 2.2. Dealing with all dielectric waveguides, both airy and dielectric modes can be classified as hybrid (HE or EH) or transverse (TE or TM) [81]. Additionally each mode is provided with two subscripts, ν and μ: the former indicates the numbers of periods in the azimuthal direction, whereas the latter is for the number of maxima and minima in the radial direction. Their dispersion curves are shown in Fig. 2.3 in terms of the normalized frequency F:

$$F = \frac{2t}{c} f \sqrt{n_H^2 - n_L^2}. \tag{2.1}$$

Dispersion curves of the dielectric modes have been obtained from their characteristics equations [53], whereas leakage loss and dispersion curves of the airy modes have been numerically computed. The discontinuities in the dispersion curves of the airy modes are due to the coupling with dielectric modes which causes anti-crossings and high leakage loss. Similar coupling has been observed in hollow core photonic band gap fibers between core and surface modes [82] and

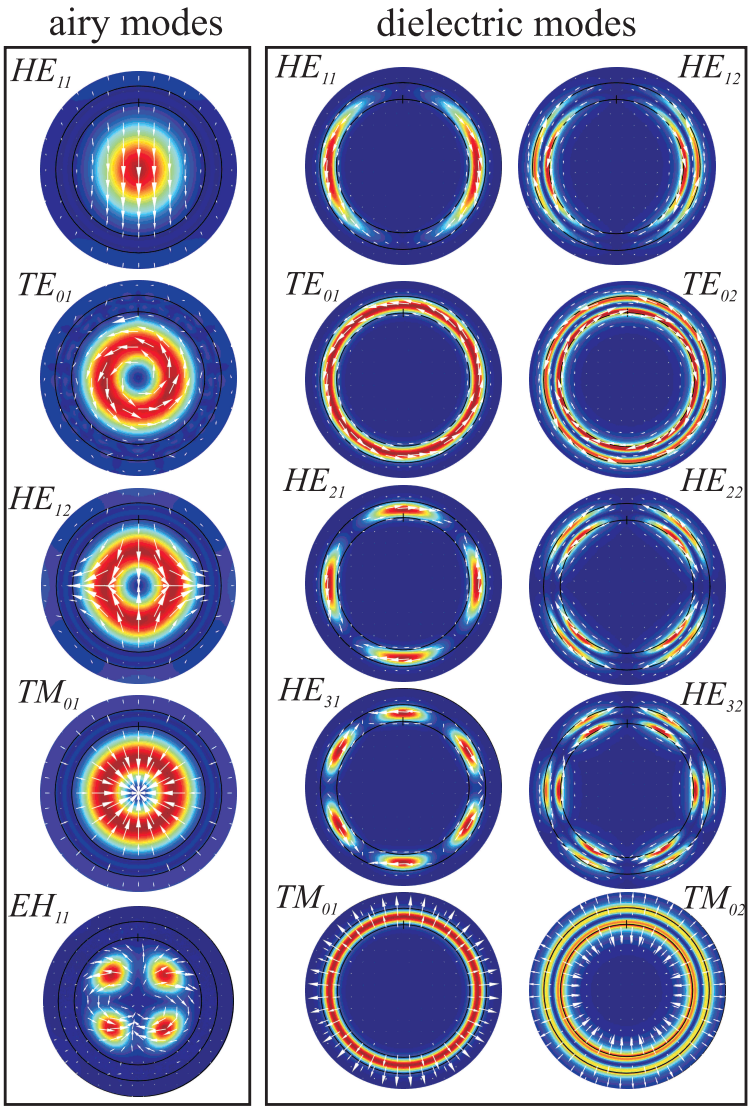

Figure 2.2: Modal intensity and electric field distributions of the lowest order airy and dielectric modes for a stand alone tube waveguide.

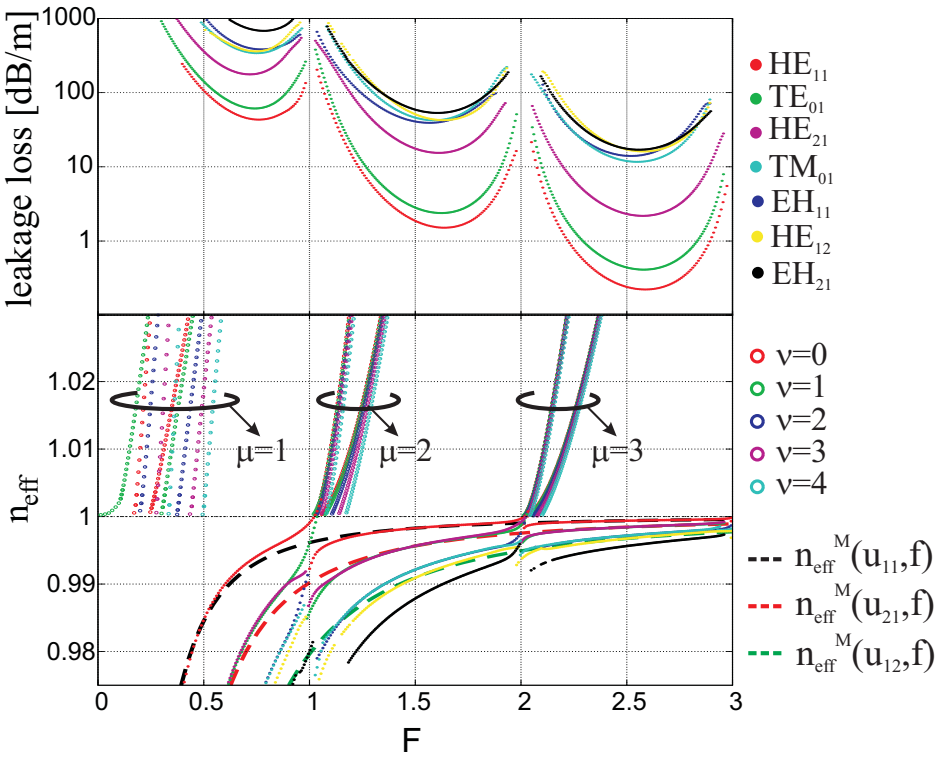

Figure 2.3: Top: leakage loss for the lowest order airy modes of the tube waveguide. Middle: dispersion curves for the dielectric modes with $\nu = \{1, 2, 3\}$ and $\mu = \{0, 1, 2, 3, 4\}$. Bottom: dispersion curves for the airy modes of the tube waveguide along with their Marcatili's approximation. A tube waveguide with $n = 1.44$ and $\rho = 0.9$ was considered for these curves.

in W fibers between core and discrete lossy cladding modes [83]. Since the effective indices of the airy modes are closed to n_L, coupling occurs when dielectric modes approach their cut-off frequencies.

Far from resonances, airy and dielectric modes are decoupled and this allows the former to be strongly confined inside the hollow core with a negligible intensity inside the dielectric layer. This suggests that their characteristics do not significantly depend on cladding parameters. In Fig. 2.3 the numerical dispersion curves of the airy modes are approximated with the Marcatili's formula [54]:

$$n_{eff}^{M}(u_{\nu\mu}, f) = 1 - \frac{1}{2}\left(\frac{u_{\nu\mu}c}{2\pi f R}\right)^2, \tag{2.2}$$

where R the air core radius and $u_{\nu\mu}$ is the μ-th root of the equation $J_{\nu-1}(u) = 0$. A part from the anticrossing frequencies, an overall excellent agreement is found in Fig. 2.3 between the analytical expression given by Eq. (2.2) and the numerical values.

The normalized cut-off frequencies of the $HE_{1,\mu}$ dielectric modes are

$$F_c = \mu - 1. \tag{2.3}$$

Equation (2.3) corresponds exactly to the cutoff conditions of the $TE_{\mu-1}$ modes of a slab waveguide with width t or, equivalently, to transverse resonance condition. In former models they were used to predict high loss regions in kagome fibers [36, 48, 76], square lattice fibers [49, 50] and also in pipe waveguides [44]. The main limitation of these models is that they cannot predict how the cladding parameters influence the spectral width of high loss regions. This is extremely important for IC fibers in general, since one of the main goal is to achieve broadband transmission windows. Moreover, the TE_1 mode of the slab waveguide has a cutoff normalized frequency at $F_c = 0$ ($f = 0$ Hz). This means that the previous model are not even able to justify the high loss regions found at low frequencies ($F \to 0$) in all the IC fibers proposed in the literature. A possible improvement for this former model was to consider also the TM modes of the slab waveguide by introducing an "effective" cutoff condition [49]. However, due to the empirical nature of this method, it is extremely application dependent and it can only hardly been extended to other waveguides with different cladding

parameters.

Figure 2.3 highlights that a part from the $HE_{1,\mu}$ modes, for each value of the μ parameter the dielectric tubes supports also $TE_{0,\mu}$, $TM_{0,\mu}$ and many other $HE_{\nu,\mu}$ and $EH_{\nu,\mu}$ modes. This means that there are many different modes with different number of periods in the azimuthal direction, but with the same number of peaks in the radial one. For sake of clearness, in Fig. 2.3 only dielectric modes with low azimuthal dependence ($\nu \leq 4$) were reported. According to the coupling theory [84], thanks to the low spatial dependence, these are the only dielectric modes which can couple to the core ones.

Figure 2.3 shows that, even though these dielectric modes share the same μ parameter, their cutoff frequencies increase with the ν value. Moreover, this spreading of the cutoff values is connected to the μ parameter: the lower the μ value, the higher the spreading. Therefore $\mu = 1$ represent the worst case, since cutoff frequencies of dielectric modes with $\mu \leq 4$ are spread between $F = 0$ and $F = 0.5$, which explains the increase of the propagation loss for the airy modes at low frequencies.

Dielectric modes' cutoffs can thus be used to estimate high loss spectral width. In general, normalized cutoff frequencies depend only on the ratio ρ between inner and outer tube radius [53]:

$$\rho = \frac{r_{int}}{r_{ext}} = 1 - \frac{t}{r_{ext}}, \tag{2.4}$$

and the refractive index n_H of the tube (N_L is assumed to be always air). Figure 2.4 shows the normalized cut-off frequencies of the dielectric modes with low azimuthal dependence ($\nu \leq 4$) versus ρ for three different values of the dielectric refractive index $n_H = \{1.44, 2.0, 2.5\}$. As ρ is reduced ($\rho \to 0$) the cut-off frequencies spread out over a wider range. For each transmission window, there exists always a critical ρ value, named ρ_c, at which curves with different μ values cross each other. For $\rho < \rho_c$ there are no cutoff free spectral regions for that specific transmission window. In general, since spreading depends on radial index μ, ρ_c reduces as μ increases. On the contrary, as shown in Fig. 2.4 these ρ_c values do not depend significantly on the refractive index of the tube.

Therefore, from a performance point of view, high ρ values ($\rho \to 1$) are much

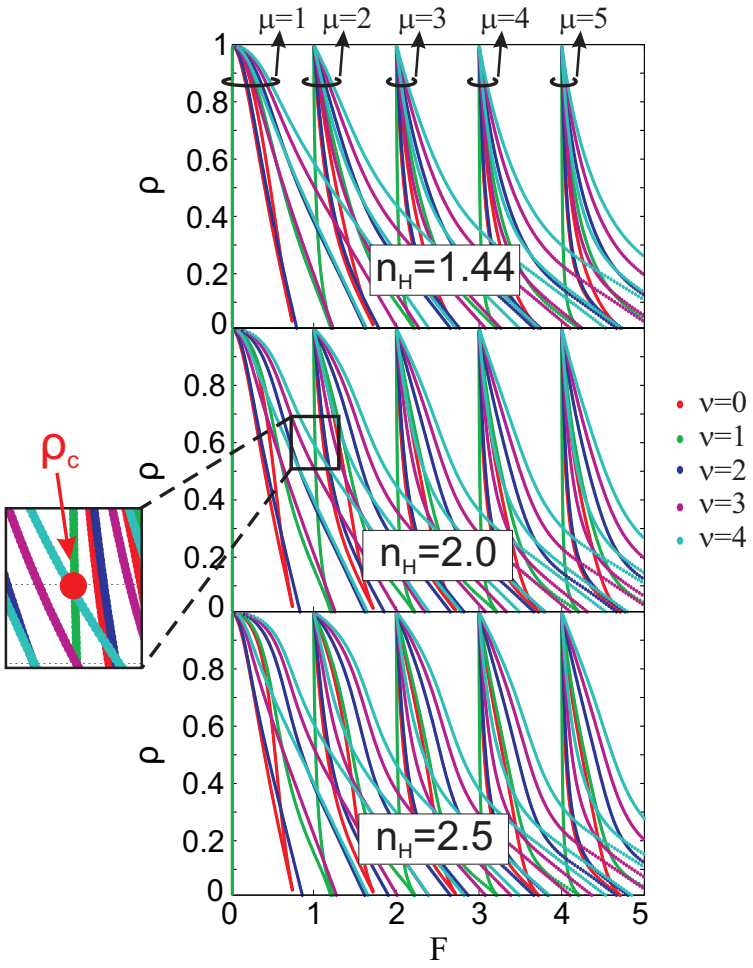

Figure 2.4: Normalized cut-off frequencies versus the inner and outer diameter ratio ρ, for three different dielectric refractive indices: $n_H = \{1.44, 2.0, 2.5\}$.

more appealing in order to obtain wide transmission bandwidths. Here, however, the spreading of the dielectric modes is much more sensitive to the value of n_H which is used for the tube. In general, the lower the refractive index of the dielectric material, the lower the spreading of the dielectric modes and, thus, the wider the transmission bandwidth.

Finally, it should be noted that when $\rho \to 1$, the spreading of the cutoff frequencies tends asymptotically to the expression given in Eq. (2.3). This means that this model and the ones that were previously proposed in the literature are perfectly equivalent for very thin structures. Indeed $\rho \approx 1$ means $t/r_{ext} \approx 0$ according to Eq. (2.4). However the purpose of this model is to extend the previous ones also to the cases in which $\rho < 1$ which are more interesting from a manufacturing point of view.

2.2 Triangular tube lattice fiber with circular tubes

The typical cross section of a triangular tube lattice fiber with circular tubes (TTLF-CT) is reported in Fig. 2.1(b). The hollow core is obtained by removing the seven innermost tubes. Since the tubes surrounding the core are centered on the vertices and on the middle points of a hexagon with side length 2Λ, the core shape is approximately a hexagon whose apothem R_{co}^{max} and radius R_{co}^{min} are:

$$R_{co}^{max} = 2\Lambda - r_{ext} \tag{2.5}$$

$$R_{co}^{min} = \sqrt{3}\Lambda - r_{ext}. \tag{2.6}$$

The analysis of the waveguiding mechanism here proposed does not depend by the number of tube rings surrounding the core, thus, for sake of simplicity, hereinafter a fiber with two rings of tubes is considered. The guiding mechanism is the same of kagome and square lattice fibers recently developed for visible and near infrared applications [85]. In this kind of fibers the cladding does not exhibit photonic band gap. Cladding modes can be still classified in dielectric and hole modes as shown in Fig. 2.5(b) and (c) respectively. Intensity and electric field distribution of the lowest order core modes are reported in Fig. 2.5(a). The field confinement inside the hollow core is due to the weak coupling between the core

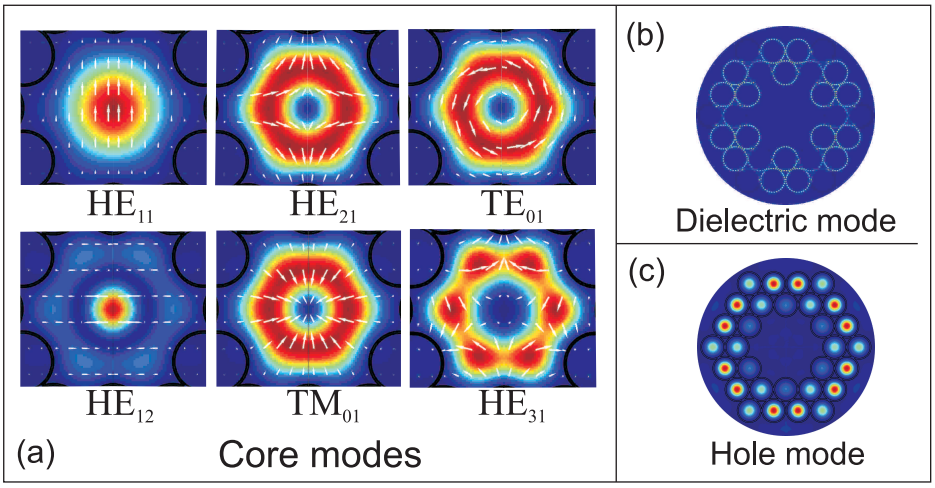

Figure 2.5: (a) Intensity and electric field distribution of the lowest order core modes of the TTLF-CT shown in Fig. 2.1. (b)-(c) Examples of dielectric and hole modes.

modes and the dielectric modes [36, 48–50, 76]. Core modes can propagate with low loss if the difference between their effective indices with those of dielectric modes is high enough (phase matching condition) and the field overlap is low. Figure 2.6 shows the propagation characteristics of the first 14 core modes (considering that some modes have a doublet polarization). The leakage loss quickly increases at the resonances with dielectric modes and the dispersion curves are perturbed by the anti-crossing phenomenon. As in the single tube waveguide, this occurs when dielectric modes are closed to the their cut-off frequencies. Far from them, the differences between effective indices of core and dielectric modes are high enough to give low coupling and, thus, low leakage loss. The irregular spectral behavior of the leakage loss in the low loss regions is due to the weak coupling of the core modes with dielectric modes having high azimuthal dependence whose cutoff falls in this range of frequencies. The high order mode (HOM) with the lowest leakage loss is the TE_{01} mode.

Since the core modes are highly confined within the core, it is reasonable to think that their dispersion characteristics are similar to those of the airy modes of the tube waveguide shown in the previous section. In Fig. 2.6, the curves obtained

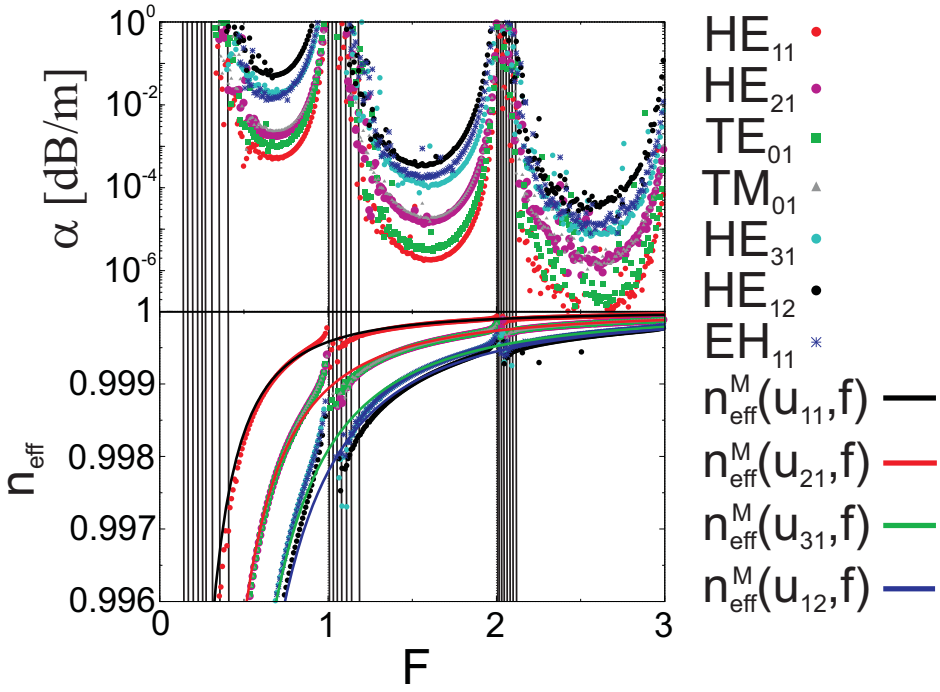

Figure 2.6: Dots represent numerical leakage loss (top) and effective index (bottom) of the lowest order core modes of a triangular tube lattice fiber. The curves in the bottom graph are the Marcatili's approximations for the dispersion curves of the core modes.

through Eq. (2.2) with core radius $R = (R_{co}^{max} + R_{co}^{min})/2$ are reported with solid lines. Also in this case an overall excellent agreement is found between the analytical curve and the numerical values, with discrepancies being limited only to the resonant frequencies.

Theoretical models that have been proposed in the literature for similar solid core fibers and photonic band gap fibers [86–88] were based on the analysis of the single elements forming their cladding. Together with the cladding modes images that have been reported in Fig. 2.5(b) and (c), this suggests that even the cladding modes of the TTLF-CT can be derived starting from those of a single CTF considered alone. This greatly simplifies the analysis of the proposed TTLF-CT since it is reduced to the investigation of a much simpler CTF. Even though the relative coupling between two adjacent tubes is neglected in this model for simplicity, the validity of the model is confirmed by the results reported in Fig. 2.7. On the top, the dispersion curves of the TTLF-CT's dielectric modes are compared with those of a CTF around the normalized frequency $F = 1$. The green crosses refer to all the dielectric modes of the TTLF-CT in the considered frequency range, whereas the red dots highlights only dielectric modes with $\mu = 2$ and $\nu \leq 4$. On the same figure, also the dispersion curves of the dielectric modes a stand alone CTF have been reported for comparison. This stand alone tube is absolutely identical to the ones that compose the cladding of the TTLF-CT under analysis, and its dielectric modes have been computed analytically. Despite some splittings in the red dotted curves due to the weak coupling between TTLF-CT's dielectric modes, the agreement is good.

The effective indices of the hole modes are reported on the bottom of Fig. 2.7. Red points show effective indices of the HE_{11}-like hole modes, whereas the dashed black line approximate the numerical dispersion through Eq. (2.2) by setting $R = r_{int}$ and u_{11}.

As a former step for the validation of the model is given in Fig. 2.6. Vertical solid lines that have been added to the propagation loss graph represent the cutoff normalized frequencies of the dielectric modes of a CTF with $\nu \leq 4$. In general, an excellent agreement is found between these vertical lines and the high propa-

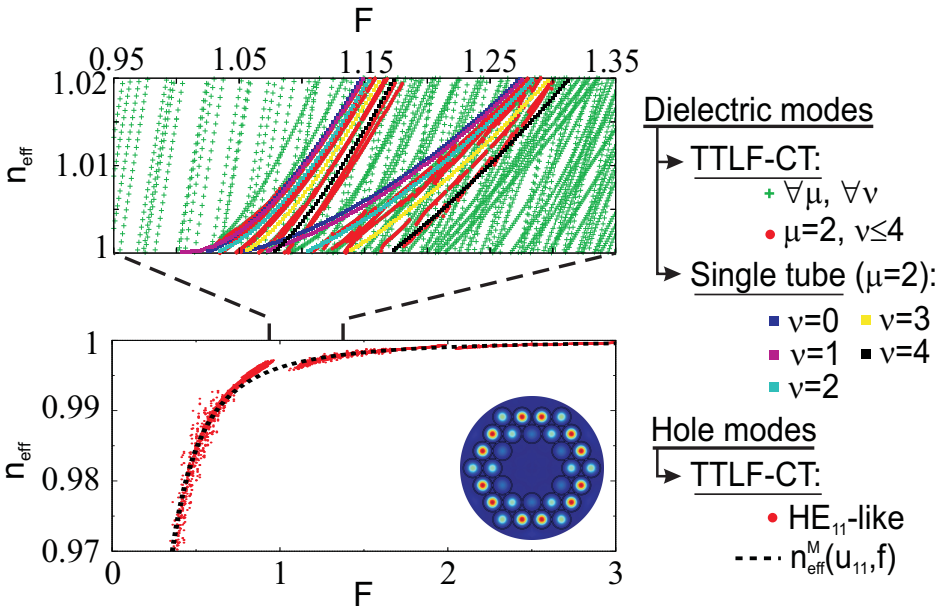

Figure 2.7: Effective indices of cladding modes versus the normalized frequency F of a TTL fiber with $\rho = 0.9$. Top: dielectric modes around $F = 1$ with high (green crosses) and low (red dots) azimuthal dependence. Squares show effective index of the dielectric modes with $\mu = 1$ and $\nu = \{0, 1, 2, 3, 4\}$ of the single tube waveguide computed analytically. Bottom: dispersion curves of the HE_{11}-like hole modes (red points)and their Marcatili's approximation computed with Eq. (2.2) where $R = r_{int}$.

gation loss regions. In particular, these vertical lines are not only able to predict the spectral position of the resonances between core and dielectric modes, but they give also an rough estimation for the spectral width of the high loss region. The effectiveness of the model is then verified by varying the geometrical and physical parameters of the cladding tubes. As pointed out in the previous section, the ρ parameter for the cladding tubes must be high enough in order to have spectral regions which are free of low azimuthal order dielectric modes cutoffs. As shown in Fig. 2.4, this value is about $\rho_c = 0.65$ and $\rho_c = 0.45$ for the first and second transmission windows, respectively. In Fig. 2.8 the leakage loss of the FM is reported for three different values of ρ and $n = 1.44$.

As expected from the results shown in Fig. 2.4, with $\rho = 0.4$ there are no low loss regions in the considered normalized frequency range and the dispersion curves exhibit several anti-crossing perturbations due to coupling with dielectric cladding modes. By increasing the ratio to $\rho = 0.65$, a low loss region clearly appears between $F = 1$ and $F = 2$, whereas it is only slightly sketched between $F = 0$ and $F = 1$. Finally, with $\rho = 0.75$ the two low loss regions are clearly depicted and the anti-crossing perturbations are mainly concentrated around $F = 1$ and $F = 2$.

As a final test for the proposed model, Fig. 2.9 compares dispersion and propagation loss curves for three TTLF-CTs with the same geometrical dimensions for the cladding tubes ($\rho = 0.9$), but different refraction indices, $n_H = \{1.44, 2.0, 2.5\}$. Even in this case, the behavior of the high loss regions is correctly predicted from the curves shown in Fig. 2.4: the higher the refractive index, the wider the high loss regions. The difference in the minimum propagation loss and dispersion curves among different n_H values can readily been explained by observing that Eq. (2.1) depends on n_H, whereas Eq. (2.2) not. Therefore, once F is fixed in Eq. (2.1) and n_H is increased, the absolute frequency f is reduced. In turn, a reduction of the working frequency in Eq. (2.2) for the same value of core size R, cause a reduction of the effective index and, thus, an increase in the leakage loss.

Finally, it is important to point out that the model which has been developed

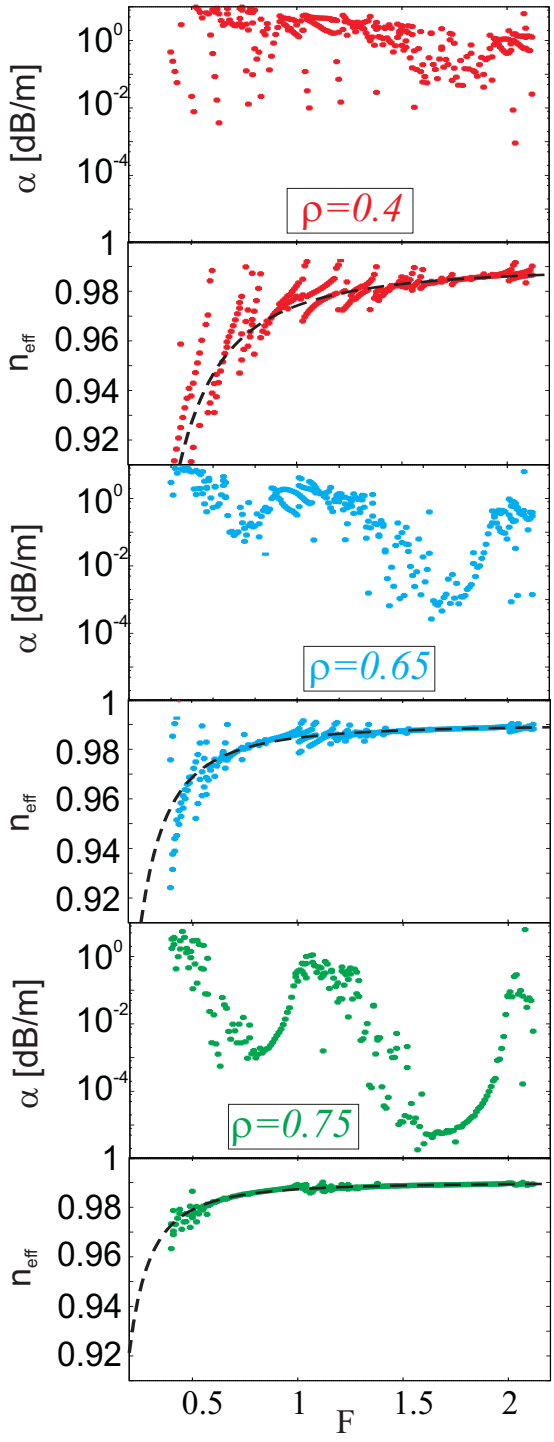

Figure 2.8: Leakage loss and dispersion curves for $n = 1.44$ and three different values of the ratio ρ: 0.4 (red dots), 0.65 (blue dots), and 0.75 (green dots). Dashed black lines show dispersion curves given by Eq. (2.2) with u_{11} and $(R_{co}^{max} + R_{co}^{min})/2$ being R_{co}^{max} and R_{co}^{min} computed through Eq. (2.5).

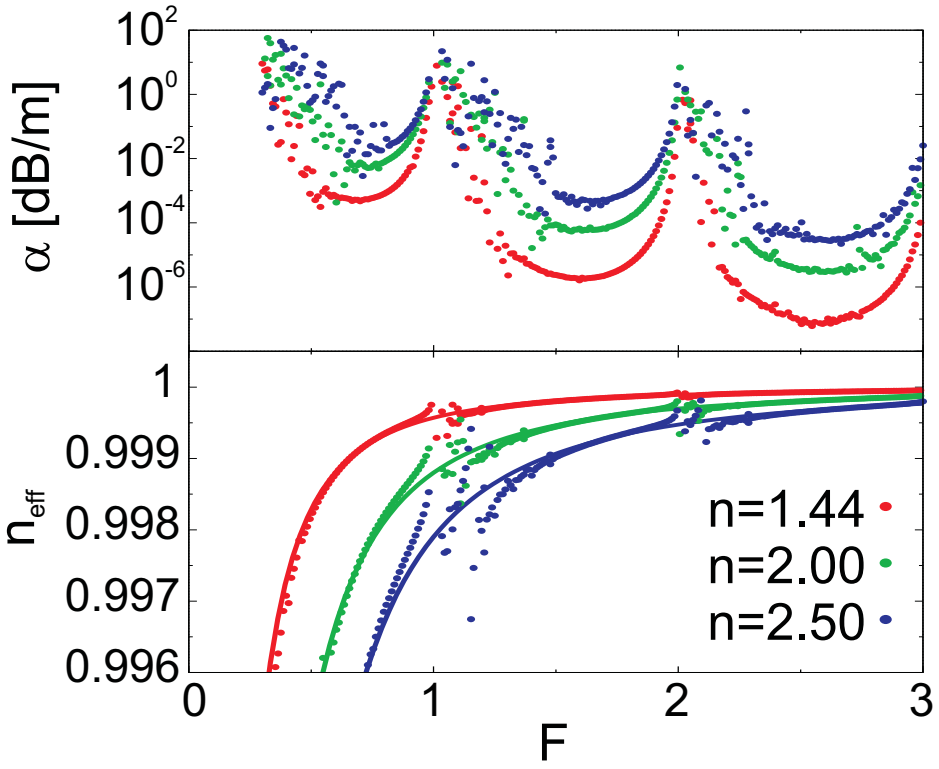

Figure 2.9: Leakage loss (top) and dispersion curves (bottom) for $\rho = 0.9$ and three different values of the refractive index n: 1.44 (red), 2.0 (green), and 2.5 (blue). Solid black lines shows dispersion curves computed through Eq. (2.2) with $(R_{co}^{max} + R_{co}^{min})/2$ being R_{co}^{max} and R_{co}^{min} computed through Eq. (2.5).

in this section does not depend on a particular arrangement of the tubes in the cladding. This assumption will be exploited in the next section in order to design effectively single mode hollow core fibers.

2.3 Effectively single mode fiber design

In hollow core fibers, the overlap between the core mode and dielectric material plays a key role in determining absorption loss. This is true especially in THz region where no highly transparent dielectric material exist [15]. In order to reduce the absorption caused by the dielectric materials in the cladding, the hollow core size must be significantly larger than the working wavelength. Unfortunately this makes the fibers multimoded [89], thus strongly limiting the performance of the fiber for both pulsed application and data transmission. A way to reduce the detrimental effects caused by high order modes is to impair them by increasing the differential loss:

$$\Delta\alpha = \alpha_{FM} - \alpha_{HOM}, \tag{2.7}$$

where α_{FM} and α_{HOM} are the propagation loss of the fundamental core mode and those of the high order mode with the lowest loss, respectively. A simple decrease of the core size through a reduction of r_{ext} can not be applied since this would affect also the propagation loss of the fundamental core mode [89]. Indeed, as shown in the previous section, this would cause a reduction in the ρ parameter of the cladding tubes and, in turn, a reduction of the transmission windows bandwidth followed by an increase of the minimum achievable propagation loss. The purpose of this section is to show that, by using the proposed model, it is possible to improve the tradeoff between $\Delta\alpha$ and α_{FM}, simply by changing the arrangement of the tubes around the core.

A technique to increases HOMs' loss without affecting the FM one is to couple them with the hole modes of the cladding. A similar technique has already been proposed in the literature for both solid and hole assisted fibers [90] and HC-PBG fibers [91] in order to obtain effectively single mode operation. Since both HOMs and hole modes' dispersion curves are well approximated by their

respective Marcatili's formulas as given in Eq. (2.2)), it is reasonable to suppose that once the phase matching condition is achieved, this is verified over a wide frequency range.

Two rings of tubes were used in the TTLF-CT considered in the previous chapter. However, due to the dielectric materials used in the cladding, when the TTLF-CT is considered for the THz spectral range, the absorption loss dominates over the leakage loss even if the cladding is reduced to only one ring of tubes [89]. This opens up for the use of new geometries for the arrangement the tubes in the cladding. In particular, as shown in Fig. 2.10, it is possible to obtain a circular tube lattice fiber (CTLF) by arranging N tubes on a circular pattern with a distance Λ between their centers. The relationship between tubes' external radius r_{ext} and fiber core radius R_{co} depends on N. With some simply geometrical considerations, it is possible to show that:

$$R_{co} = \frac{\Lambda}{2\sin\left(\frac{\pi}{N}\right)} - r_{ext}. \tag{2.8}$$

By starting from that observed in the previous sections, the effective index of the HOM with lowest loss, namely the TE_{01}, can be estimated as:

$$n_{HOM}^{TE_{01}} = 1 - \frac{1}{2}\left(\frac{u_{21}c}{2\pi f R_{co}}\right)^2. \tag{2.9}$$

Similarly, the effective index of the HE_{11}-like hole modes can be estimated as:

$$n_{holes}^{HE_{11}} = 1 - \frac{1}{2}\left(\frac{u_{11}c}{2\pi f r_{int}}\right)^2. \tag{2.10}$$

By equating Eq. (2.9) and (2.10), it is possible to obtain the the number N of tubes which are necessary to guarantee the phase matching condition between core mode TE_{01} and the HE_{11}-like hole modes:

$$N = \frac{\pi}{\arcsin\left[\frac{\Lambda}{2r_{ext}}\frac{1}{1+\rho\frac{u_{21}}{u_{11}}}\right]}. \tag{2.11}$$

A plot of Eq. 2.11 versus ρ for three different values of $\Lambda/(r_e xt)$ is reported in Fig. 2.11. For reasonably high values of the ρ parameter, i.e. $0.8 \leq \rho < 1$, the optimum N value can be rounded to $N = 7$.

To bear out this prediction, three different kind of fibers have been considered:

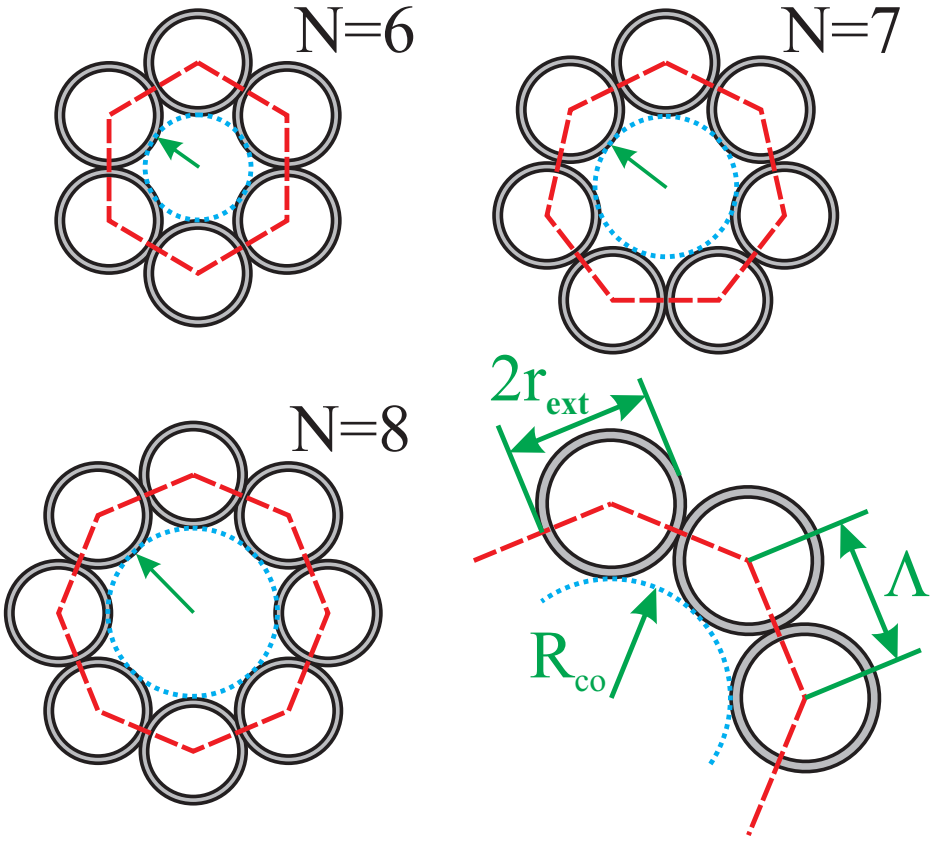

Figure 2.10: Fibers geometries obtained by arranging $N = \{6, 7, 8\}$ tubes on a circular pattern. Geometrical dimensions for a generic arrangement have also been reported.

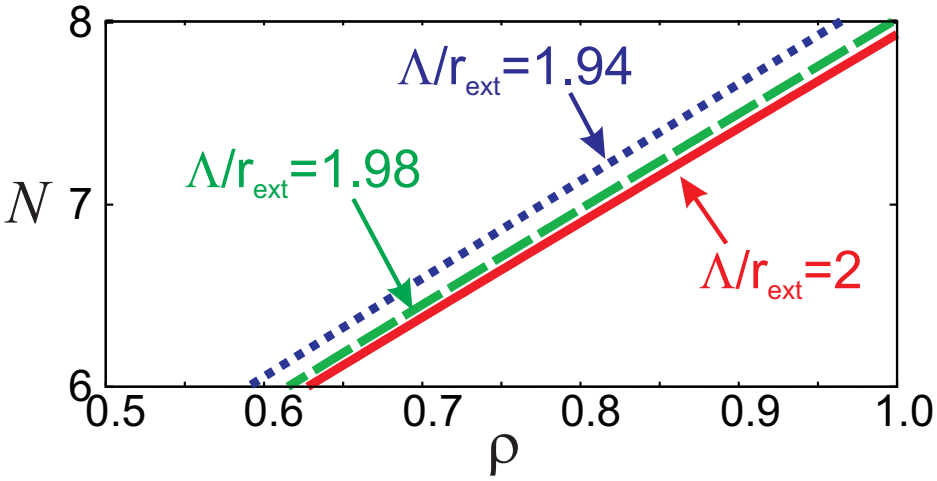

Figure 2.11: Optimum number of tubes in the cladding of a tube lattice fiber in order to guarantee the resonance between the TE_{01} core mode and the HE_{11}-like hole modes according to Eq. (2.11).

a TTLF-CT fiber and two CTLF-CTs with $N = 7$ and $N = 8$, respectively. The dielectric material has been assumed to be Teflon, with a complex refractive index $n_H = n_H^r - jn_H^i$. In the THz spectral region Teflon dispersion is negligible [15, 92–95], therefore $n_H^r = 1.44$ will be assumed for all the considered frequencies. On the contrary, several values have been reported in the literature for the imaginary part. At $f = 1$ THz, n_H^i varies from $0.69 \cdot 10^{-3}$, corresponding to about 120 dB/m [93], to $4.5 \cdot 10^{-3}$ corresponding to 870 dB/m [15]. In the present analysis a $n_H^i = 1.2 \cdot 10^{-3}$ has been assumed corresponding to 220 dB/m [94, 95]. By fixing $t = 0.1$ mm, the first low loss region centered around 1.2 THz and the resonance for $\mu = 2$ is at $f = 1.45$ THz. In the three fibers, the tube diameters have been chosen to have the same core radius R_{co}. In order to evaluate only the leakage loss, firstly a lossless material has been considered by assuming $n_H^i = 0$. In Fig. 2.12 leakage loss and dispersion curves of the FM and the first four HOMs are reported in case of $R_{co} = 1.2$ mm. The dispersion curves are approximately the same for the three fibers, according to the theory. Also the minimum of the leakage loss of the FM does not significantly change among different fibers. On the contrary, according to the theory, the leakage loss

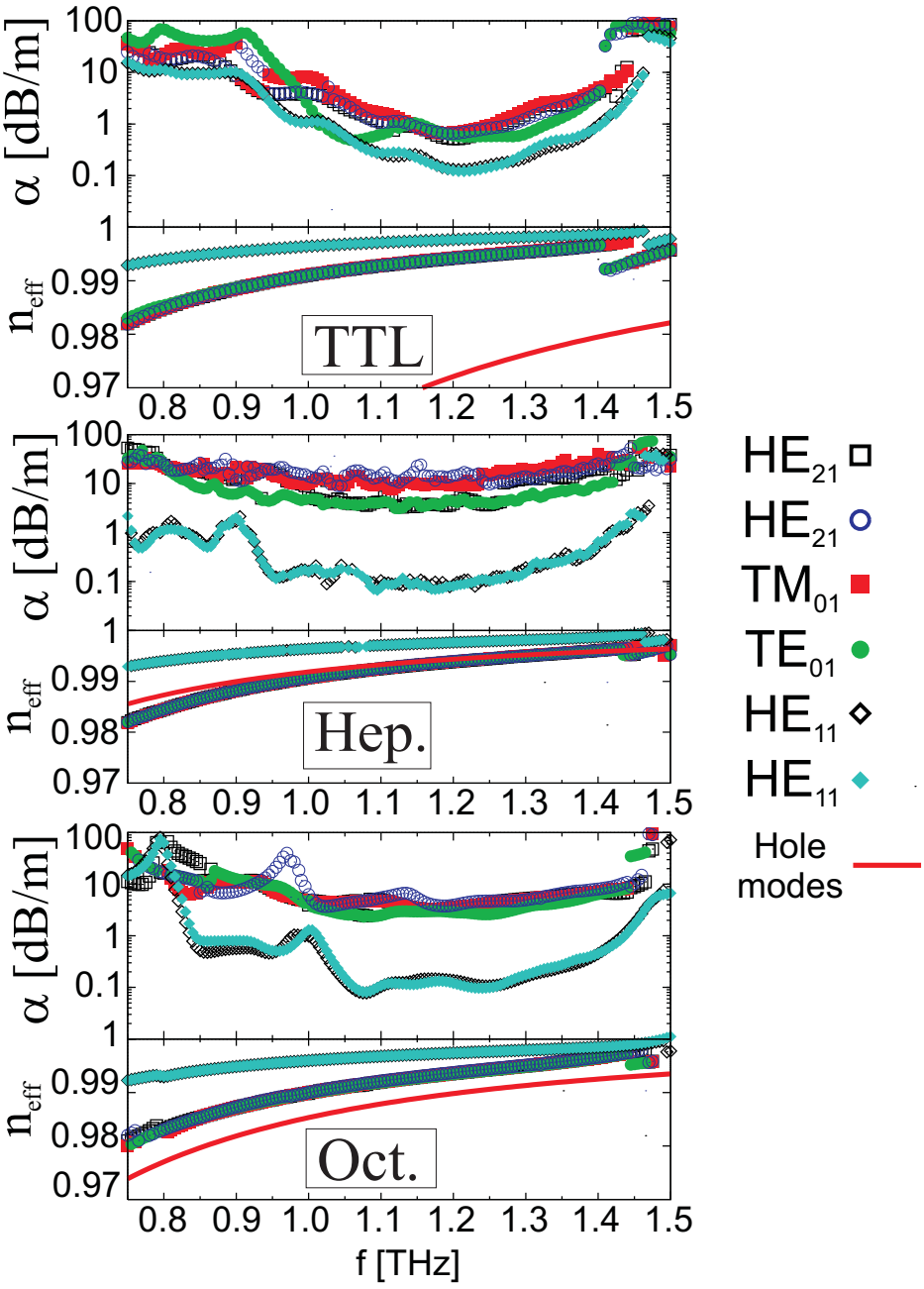

Figure 2.12: Leakege loss and dispersion curves for TTL (top), Heptagonal (middle), and Octagonal (bottom) fibers with a core radius $R_{co} = 1.2$ mm and tube thickness $t = 0.1$ mm. Solid red lines show dispersion curves of the HE_{11} airy cladding modes.

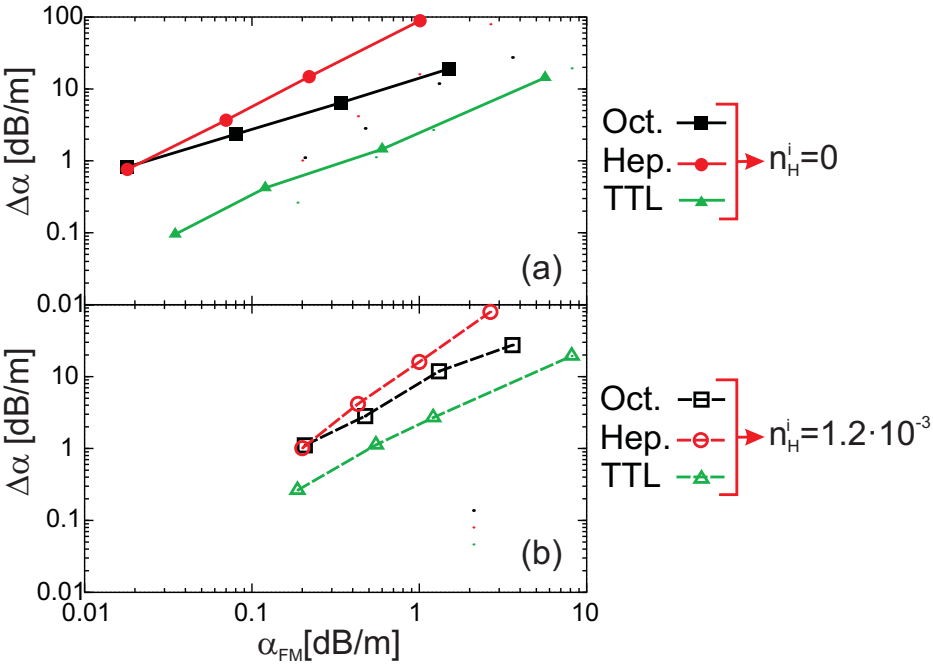

Figure 2.13: $\Delta\alpha$ versus α_{FM} for different values of the core radius, $R_{co} = \{1.6, 1.2, 0.97, 0.73\}$ mm (from left to right), in case of lossless (a) and lossy dielectric (b).

of HOMs significantly increases passing from the TTLF to the $N = 8$ and then, finally, to $N = 7$ CTLF case. In the latter the improvement is about a order of magnitude if compared to the original TTLF-CT. In fact, as shown in Fig. 2.12, in the fiber with 7 tubes, the dispersion curve of the HE_{11}-like hole modes (solid red line) is much closer to those of HOMs than in the other fibers. Furthermore this phase matching condition is maintained over a broad range.

In order to better highlight the improvement allowed by the CTLF structure, in Fig. 2.13(a) the differential loss $\Delta\alpha$ are plotted versus the minimum of the FM loss α_{FM} for the three fibers considered above. All fibers exhibit a quasi-linear relationship in the log-log scale used for the graph and the $N = 7$ CTLF-CT exhibits the steepest curve. However, as the core size is increased, the $N = 7$ and $N = 8$ cross each other when $R_{co} = 1.6$ mm. This can readily been explained through Fig. 2.11. In the current analysis, an increase of r_{ext} is used to increase the core size while keeping the t value constant for the cladding tubes. This cause

the ρ parameters to approach high values ($\rho \to 1$). According to Fig. 2.11, the optimum number N of tubes is then changed from 7 to 8.

Figure 2.13(b) shows the same comparison between the three fibers, but considering a lossy dielectric in the cladding with $n_H^i = 1.2 \cdot 10^{-3}$. The absorption effect is high on the fundamental mode than on HOMs due its lower leakage loss. As a consequence, the curves shown previously in Fig. 2.13(a) are right shifted toward higher values of α_{FM}, whereas the vertical shift is negligible. Notwithstanding this, the same conclusions drawn for the lossless case can be drawn.

Although the threshold over which the fiber can be considered effectively single moded depends on the particular application, to fix the ideas, let assume that a differential loss $\Delta\alpha = 20$ dB/m is required. Fig. 2.13 shows that, by using a TTLF-CT fiber, a core radius of 0.73 mm is required thus giving $\alpha_{FM} = 8$ dB/m. However, the same condition can obtained in a CTLF-CT with 7 tubes with a core radius of 1 mm and $\alpha = 1$ dB/m, which is almost a decade lower than TTLF-CT's one.

Finally, in order to show that effectively single mode operation can be obtained over a broadband, Fig. 2.14 shows propagation loss and dispersion characteristics versus frequency for a CTLF-CT with $N = 7$, $R_{co} = 0.73$ mm, $r_{ext} = 0.59$ mm and $t = 0.1$ mm. As expected HOMs and hole modes dispersion curves are almost completely overlapped over the entire considered frequency range. As a consequence the differential loss is always higher than 70 dB/m, whereas the FM loss is lower 10 dB/m over a band of 0.4 THz with a minimum of 2.8 dB/m at 1.07 THz.

2.4 Effect of multiple turn of tubes around the core

The confinement mechanism that has been proposed in this chapter does not depend on the number of layer of tubes that are used in the cladding. Therefore, in the previous section, it has been shown that, when the absorption loss is reasonably high, the cladding can be conveniently reduced to only one turn of

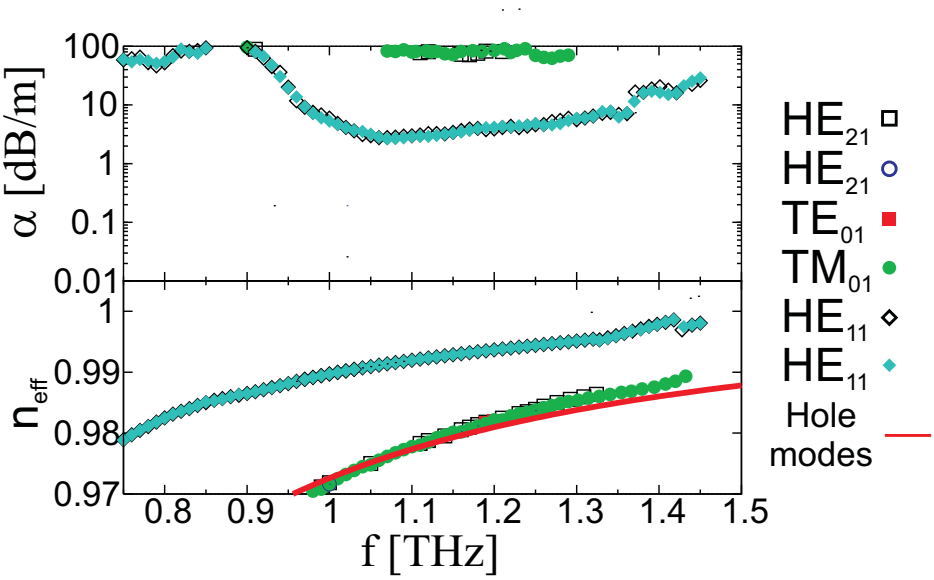

Figure 2.14: Leakege loss and dispersion curves of an heptagonal fiber with a core radius $R_{co} = 0.73$ mm and tube thickness $t = 0.1$ mm. Solid red lines show dispersion curves of the HE_{11}-like hole cladding modes.

tubes. However, CTLFs fibers have recently been proposed also for the infrared spectral region [51] where dielectric materials have, in general, lower absorption if compared to the THz spectral region. Since the purpose of this chapter is to investigate the confinement mechanism of TTLFs and CTLFs in general, in this section the effect of multiple turns of tubes in the cladding is addressed.

It has recently been shown in the literature, that in kagome fibers the confinement loss does not depend on the number of turns of tubes that are used in the cladding [75]. In order to investigate this feature also in the TTLF structure proposed in this chapter, similar fibers with identical core sizes ($R_{co} = 13.6$ μm), $t = 500$ nm, $r_{ext} = 5$ μm and $n = 1.45$ are compared in Fig. 2.15 by changing the turns of cladding tubes from 1 to 3. In all the considered cases an external jacket of infinite extent and with the same refractive index of the cladding tubes is considered. Differently from kagome fibers, the increase in the number of tubes' turns around the hollow core reduces the propagation loss in TTLF-CTs. A two orders of magnitude improvement appears in moving from one to two turns.

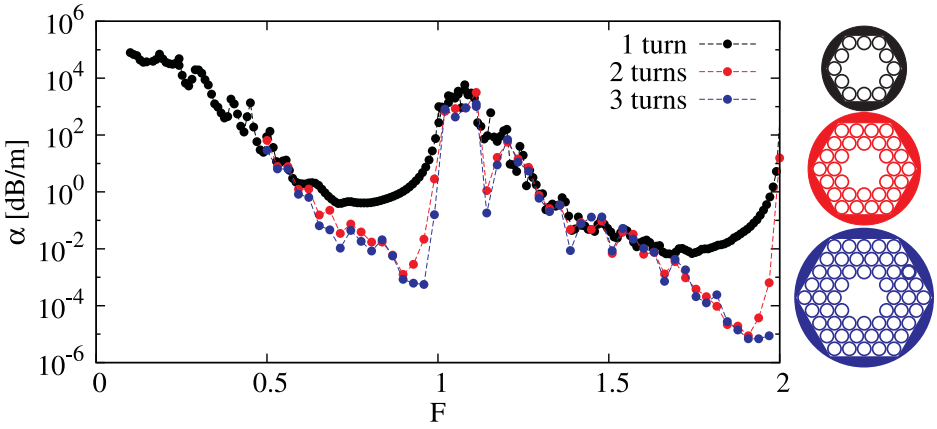

Figure 2.15: Comparison between TLFs with identical core sizes and different turns of tubes around the hollow core.

However, it must be noticed that this improvement is spectrally limited only to the middle-upper part of both the first and second transmission windows, i.e. $F \in [0.6; 1.0]$ and $F \in [1.6; 2.0]$. In the remaining part of the spectrum, where high leakage loss is found due to the coupling between the core mode and low order dielectric modes, additional turns do not enhance the confinement mechanism. If the number of turns is additionally increased (moving to the 3 turns case) only negligible reductions of the propagation loss are obtained. Moreover, they are also spectrally limited to extremely narrow regions.

Chapter 3

Performance analysis in tube lattice fibers with polygonal tubes

In the previous chapter it was shown that both TTLFs and CTLFs offer the interesting possibility to guide electromagnetic radiation inside an hollow core with low propagation losses. Their confinement mechanism is based on the low coupling between core and cladding modes. However, also other ICFs with similar cladding structures have also been recently reported in the literature, based either on a kagome [17, 36, 47, 74] or square lattice cladding [49, 96], for applications that range from the THz to the ultraviolet spectral regions. Similarly to TTLFs, for all of these fibers the transmission bandwidth can be increased by reducing the struts thickness and by increasing the lattice pitch.

Recent experimental results on kagome fibers (KFs) demonstrated that an hypocycloid core shape allows to significantly reduce the propagation loss with respect to the ideal kagome structure [47]. This loss reduction is explained by the fact that an hypocycloid core boundary does not cause distortions in the cladding structure and its length is higher if compared to the ideal kagome lattice. These factors combine to reduce the coupling with cladding modes. On the contrary, numerical

and experimental papers on CTLFs for the far infrared spectral region [51, 97] claim that that the reduction of propagation losses in CTLF with respect to the hollow tube one is due to the negative curvature of the core boundary and to the low density of states of the scattering element composing the cladding.
This chapter starts with the observation that both KFs and TTLF-CT belong to the same family of microstructured hollow core fibers in which the cladding is composed by a triangular lattice of tubes. Geometrical differences between the two structures are due to the different shapes of the tubes used in the cladding. However, despite this similarity in the cladding shape and the fact that both structures have roughly the same core's boundary perimeter and a negative curvature, KFs exhibits much higher propagation loss than the TTLFs. Therefore, the purpose of this chapter is to further investigate the role of the cladding in determining the propagation loss in ICFs. Through a thorough analysis on the shape of cladding elements, it is shown that the performance of these fibers are strongly affected by this parameter. Eventually it is shown that a cladding composed of circular tubes is highly desirable in order to obtain low propagation loss and wide transmission bandwidths, which justifies the performance improvement allowed by circular cladding shapes shown experimentally.

3.1 Outline of the IC waveguiding mechanism and considered geometries

Figure 3.1(a) shows the typical transverse cross section of a kagome fiber in which the core is formed by the removal of the 7 innermost tubes. Belonging to the same family of ICFs as the TTLFs and CTLFs shown in the previous chapter, its waveguiding mechanism can still be described by considering the coupling between the core and the dielectric modes with low spatial dependence [36,46,49]. Owing to its particular cladding structure, the former theoretical model that have been proposed in order to give an analytical description for its dielectric modes, modeled the cladding as an intersection of slab waveguides of infinite width and

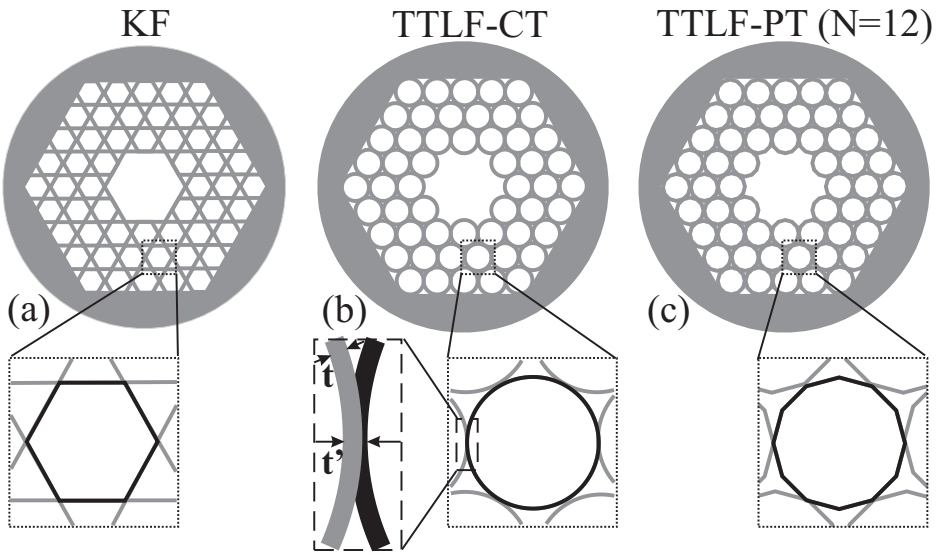

Figure 3.1: Cross sections of a kagome fiber (a), a TTLF-CT (b) and a TTLF-PT (c).

thickness t [36, 49, 76]. According to this model high loss regions are placed at:

$$F = m, \qquad m \in \mathbb{N}. \tag{3.1}$$

where F represents the normalized frequency given by Eq. (2.1).

Even though the same model was successfully applied also to TTLF [85], in the previous chapter it was shown that a more accurate prediction on the effects of cladding's parameters on the fiber's performance can be obtained by considering the spectral properties of the tubes that constitute its cladding. Since the dielectric mode of tube are known analytically [53], this model extend the previous one at almost no extra computational price. In particular, condition given by Eq. (3.1) corresponds to the cutoff of the $HE_{1,m}$ tube's dielectric modes. However, this tube-based model extends the previous slab-based one in terms of higher ability in predicting the effects of cladding's features on the propagation loss spectrum of the guided core modes. Eventually this allowed to correctly estimate the spectral width of high and loss propagation loss regions, along with the necessary conditions to ensure the existence of the transmission windows.

Figure 3.1(b) shows the typical structure of a TTLF-CT. Its cladding shape is

very similar to the KF one shown previously in Fig. 3.1(a). As suggested by relative figures' insets, only the shape of the cladding tubes have been changed moving from the KF to the TTLF-CT. This suggests that actually both fibers belong to the same kind IC fibers in which the cladding is composed by a triangular lattice of polygonal tubes (TTLF-PT) each of which has N sides. For sake of example, a 12 sided TTLF-PT is shown in Fig. 3.1. As a consequence:

- KFs $\rightarrow$ TTLF-PT with $N = 6$,

- TTLF-CT $\rightarrow$ TTLF-PT with $N = \infty$.

Moreover, the overlap between two adjacent cladding tubes is another important parameter for IC fibers [98]. For sake of clarity, the inset of Fig. 3.1(b) shows a detail of the contact point between two tubes in a TTLF-CT: t' is the dielectric thickness at the contact point and then $t \leq t' \leq 2t$. The normalized tubes' overlap is defined as

$$no = \frac{2t - t'}{t}. \tag{3.2}$$

In general, the overlap depends on the fiber fabrication process. TTLFs have been fabricated both by manual assembling of dielectric tubes [52] in the THz spectral region or by a stack and draw technique [51] for the far infrared one. In both cases the overlap between the tube is very low ($no \approx 0 \rightarrow t' \approx 2t$). KFs, on the contrary, are usually made by a stack and draw technique and the overlap values reported on the literature vary from very low ($no \approx 0$) [17] to high values ($no \approx 1$) [36, 47, 48, 99] depending on the manufacturing process.
All the fibers considered in this chapter are composed by tubes with the same thickness $t = 500$ nm and dielectric refractive index $n_H = 1.45$ (constant with the frequency). The hollow core is obtained by removing the seven innermost tubes, whereas only one ring of tubes is used in the cladding. All the numerical analysis have been performed through a modal solver based on the finite element method (FEM) [79].

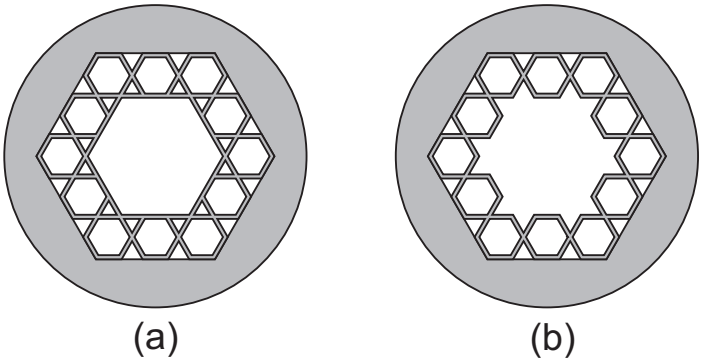

Figure 3.2: Cross sections of kagome fiber (a) and TTLF-PT with $N = 6$ (b).

3.2 Application of the tube-based model to kagome fibers

In this section the validity of the tube-based model is verified also for the KFs. Actually, Fig. 3.2 shows that the original KF's introduced in the previous section differs slightly from a TTLF-PT with $N = 6$ due to some additional dielectric structs that appear on the core boundary. Figure 3.3 compares the effective index and the normalized propagation loss for the fundamental core modes of these two fibers for the first two transmission windows ($F \in [0.5; 2]$). A $no = 1$ was assumed in the simulations in order to obtain a constant dielectric thickness in the cladding. Three different values of ρ were considered, $\rho = [0.6, 0.8, 0.95]$. Being obtained by varying the tubes' external radius (r_{ext}) while keeping a constant dielectric thickness $t = 500$ nm, this ensures that these three fibers have different core radii (R_{co}) whereas the transmission windows are spectrally placed at the same values of absolute frequency (see previous chapter).

It has been shown in the literature that for KFs [46] and hollow core Bragg fibers [100] the CL scales as:

$$CL \propto \left(\frac{c}{fR_{co}}\right)^3. \tag{3.3}$$

Therefore in Fig. 3.3 the normalization of the confinement loss is obtained by multiplying the raw data values with $(fR_{co}/c)^3$ in order to simplify the comparison.

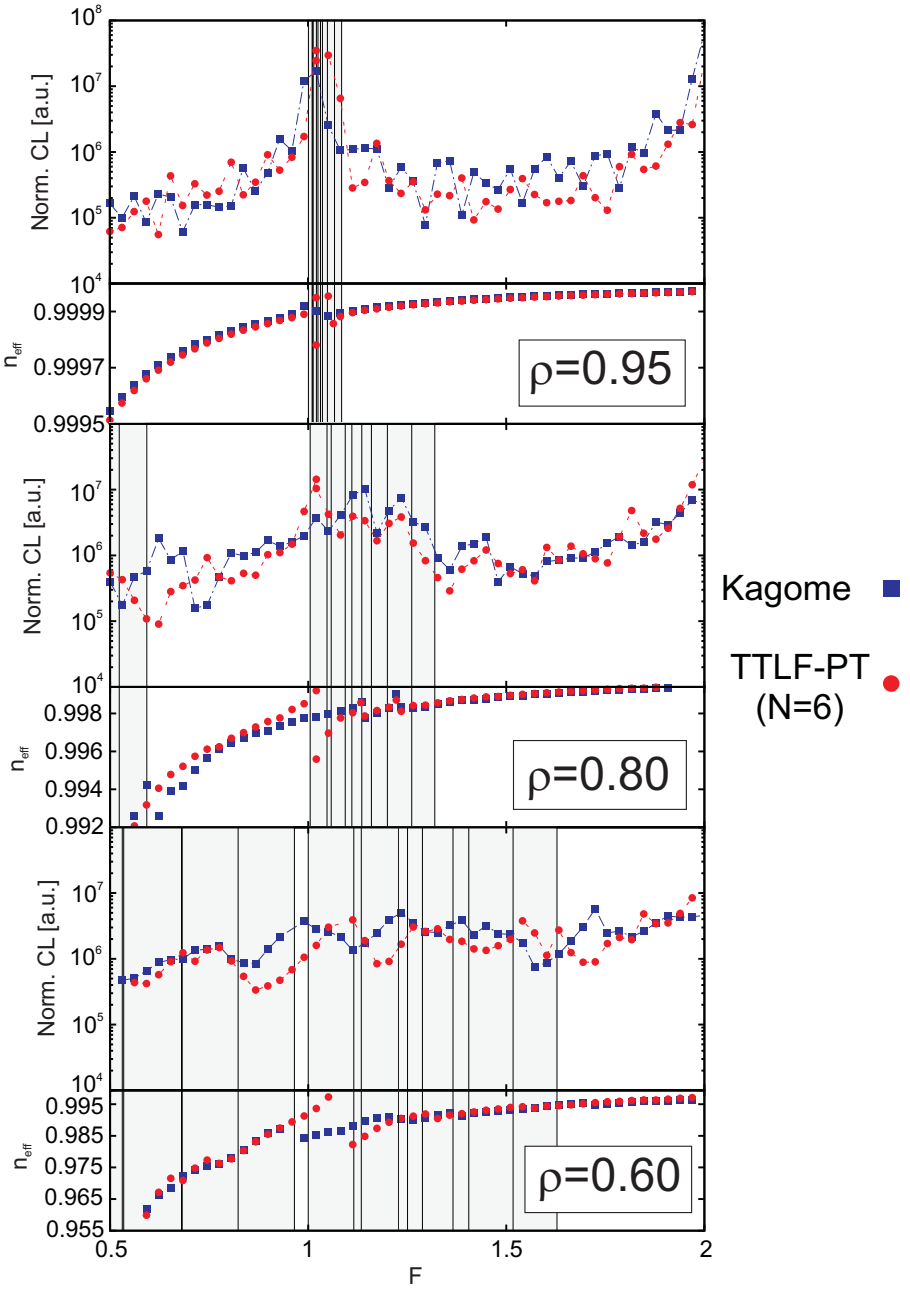

Figure 3.3: Normalized confinement loss and effective index of the fundamental core mode versus the normalized frequency F for the two fiber structures reported in Fig. 3.2 with $t = 500$ nm, $\rho = \{0.95, 0.8, 0.6\}$ (from top to bottom) and $no = 1$. Vertical lines indicate the cutoffs of the low azimuthal order dielectric modes according to the tube-based model.

Although the CL spectra of the KF and the TTLF-PT do not overlap perfectly, it is clear that the average loss spectrum is not significantly affected by the dielectric struts around the core. Dispersion curves' dependence is even weaker and slight differences appear only at the anti-crossing points caused by the coupling with dielectric modes.

Gray regions reported in Fig. 3.3 highlight the cutoff frequencies of the low azimuthal order ($\nu \leq 4$) dielectric modes of a circular tube. According to the tube-based model presented in the previous chapter, they predict the spectral position of anti-crossings between core and dielectric mode, thus determining the spectral position of high loss regions. As expected, as ρ is reduced, the cutoff of the resonant dielectric modes spread out over a wider range, causing the high CL regions to become wider and transmission windows to gradually disappear. As shown in Fig. 3.3 a $\rho = 0.6$ is enough to have no cutoff free spectral region for $F < 1$ and the complete disappearance of the first transmission window. These results are in agreement with those reported in [46], even though the microstructured cladding is slightly different. In conclusion, the application of the tube-based model to kagome fibers allows to understand why large pitches together with extremely thin dielectric structures (which means high ρ values) are generally required in order to have low propagation loss and broadband transmission.

3.3 Triangular tube lattice fibers with polygonal tubes

In order to evaluate the effect of the cladding tubes' shape on the confinement loss of the fundamental guided core mode, TTLF-PTs are considered in this section. By smoothly varying the number N of sides in each tubes from $N = 6$ to $N = \infty$ the strong performance difference between KFs and TTLF-CTs will be explained.

Figure 3.4(a) compares the dispersion curves and the propagation loss for the fundamental core modes of TTLF-PTs whose claddings tubes have $r_{ext} = 5$ μm, $\rho = 0.9$, $no = 1$ and $N = \{6, 12, 24, 36, 48, 96, \infty\}$, respectively. For all of these

fiber an ideally infinite external jacket has also been considered with the same refractive index as the cladding tubes. As expected from the Marcatili's approximation given by Eq. (2.2), a change of N does not affect the dispersion curve of the core modes because core radii are approximatively the same for the various fibers. Despite this, CL strongly changes with N: $N = 6$ represents the worst case in which the CL is prohibitively higher and noisier than the other ones. However, as N is increased, both the CL's noisiness and the average value decrease: $N = \infty$ represents the best case with a propagation loss two and three decades lower than the $N = 6$ one in the first and second transmission windows, respectively.

The improvement given by the increase in the number of sides is incremental and begins at low frequencies. Moving from $N = 6$ to $N = 12$ gives only negligible improvements to the fiber's performance for both transmission windows. Conversely $N = 24$ is already enough to have the TTLF-PT's propagation loss curve to be overlapping with the circular case for $F < 0.85$. Further increases in the number of sides progressively reduce CL also in the second transmission window. Eventually, for $N = 48$ the TTLF-PT's curve almost overlaps with the TTLF-CT over the entire considered frequency range.

In order to investigate the possible effects of the external jacket on the confinement mechanism of the fibers considered above, Fig. 3.4(b) compares the performances of the same fibers in the case in which the dielectric jacket is removed. As expected CL are reduced with respect to Fig. 3.4(a) due to the reduced coupling efficiency between the dielectric modes and the freely radiating bulk modes of the jacket. In general the same conclusions drawn for Fig. 3.4(a) are still valid. However, the main effect of the jacket removal is to allow a faster convergence toward TTLF-CT's performance when N is increased. $N = 48$, indeed, is already enough to allow for a CL spectrum which is almost overlapping with the circular case.

Finally the effects of the tube overlap was also investigated. Figure 3.4(c) compares the performances of the same fibers shown in Fig. 3.4(a) by reducing the normalized overlap from $no = 1$ to $no = 0$. A small increase in the dispersion

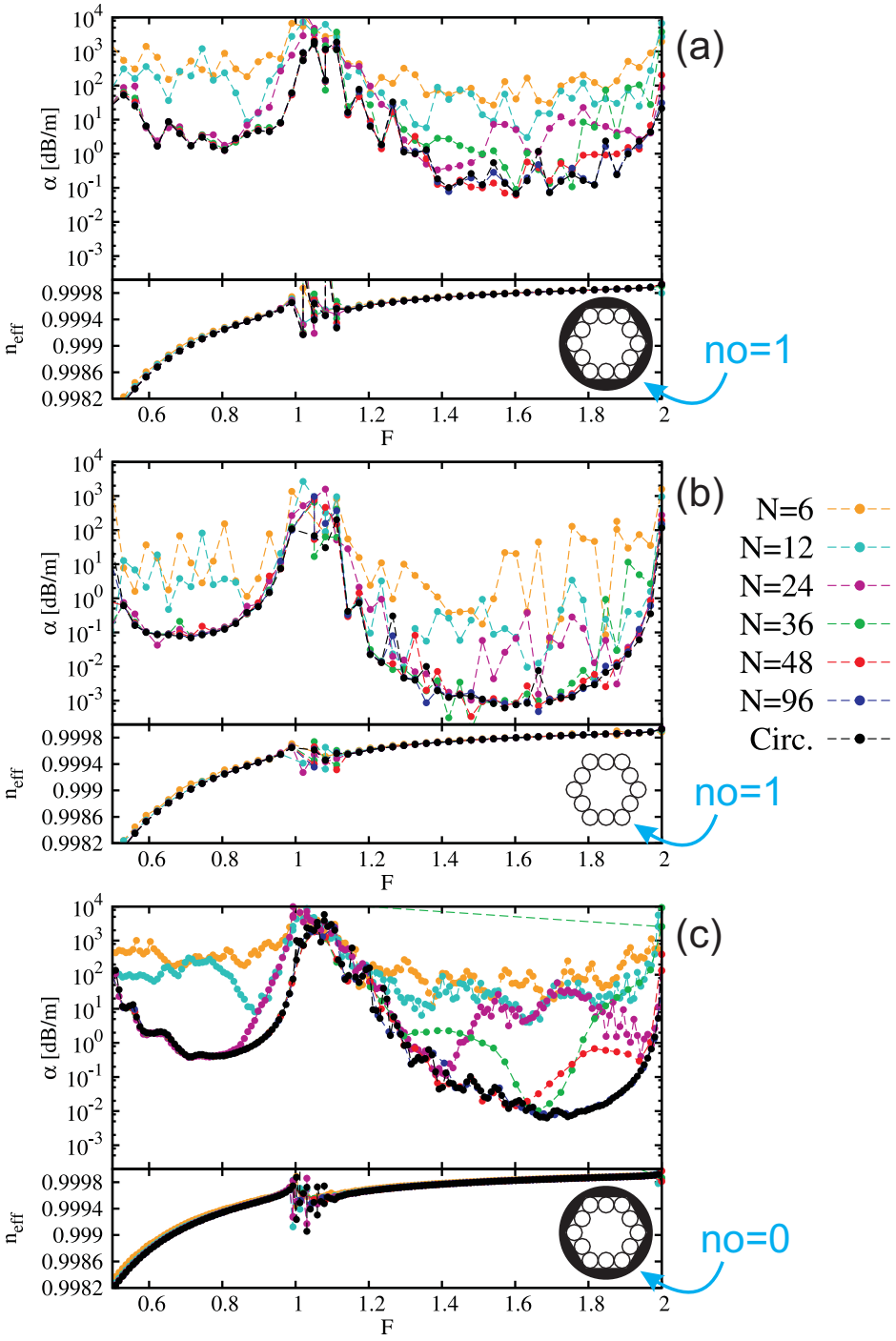

Figure 3.4: Confinement losses and effective indices versus the normalized frequency F for the fundamental core modes of TTLF-PTs with different number N of sides. (a) refers to fibers with an external dielectric jacket and $no = 1$; (b) refers to fibers with no external jacket and $no = 1$; (c) refers to fibers with an external dielectric jacket and $no = 0$.

curves of the core modes is found due to the slight increase of the core size of the fiber after this change. If compared to the fully overlapping case, with $no = 0$ the CL spectra become smoother and lower in magnitude. This is extremely important: differently from what it has been shown in the literature, the variation of the dielectric thickness in the cladding does not necessarily make CL worse. However the convergence toward the best performance becomes slower for $no = 0$. Differently from the $no = 1$ case, even for $N = 48$ noticeable differences with respect to the circular case are found for $F > 1.5$. In this case the perfect overlapping with the circular case is obtained only with $N = 96$.

3.4 Analysis of the performance of an hypocycloid-like core-cladding interface

In the previous section it has been shown the shape of the cladding tubes have a strong impact on the confinement loss performance of the fiber. However, it has recently been shown in the literature that an hypocycloid core-cladding interface allows to strongly reduce the confinement loss in kagome fibers [47]. According to the authors, indeed, the hypocycloid core-cladding interface increases the core boundary perimeter with respect to the kagome fiber, thus reducing the undesired couplings between the core and the dielectric modes. Other works [51], on the contrary, claims that this reduction of the losses is connected to the negative curvature core-cladding boundary.

In order to deeply investigate the role of the core boundary in the confinement loss mechanism of ICFs, hypocycloid-like tube fibers (HLTFs) are here considered. Their typical structure is shown in Fig. 3.5: each HLTFs is obtained from its relative TTLF-PT with N sides by cutting the cladding tubes at their contact points. This results in a hypocycloid-like curve in which the arcs have alternatively $N/2$ or $N/3$ sides. All the HLTFs considered here have $r_{ext} = 5$ μm, $\rho = 0.9$ and $no = 1$.

Figure 3.6 compares the numerical results of various HLTFs having the same core size and different N. Despite all the considered HLTFs have roughly the

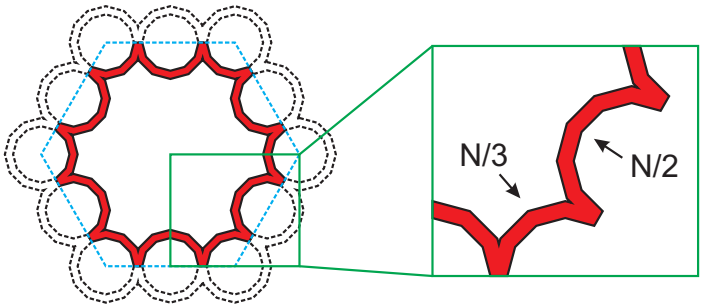

Figure 3.5: Cross section of an hypocycloid-like tube fiber with $N = 12$. The arcs are polygons with alternatively $N/2$ and $N/3$ sides.

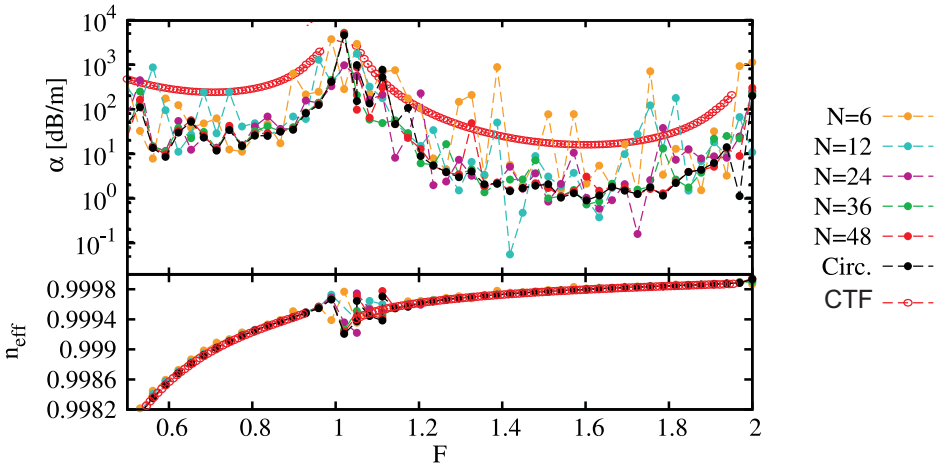

Figure 3.6: Confinement loss (top) and effective index (bottom) of the fundamental mode versus the normalized frequency F for various HLTFs with different number of sides N. CTF's performance is also considered for comparison.

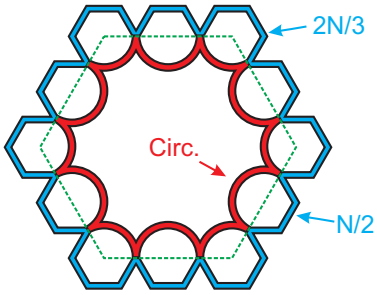

Figure 3.7: Transverse cross section of a hybrid TTLF-PT with a circular hypocycloid core boundary.

same core boundary perimeter and a negative curvature, the confinement loss dependence on N is still very high. As it has been shown in the previous section, the higher the number of the sides, the smoother and lower the propagation loss. Therefore, $N = 6$ is still the worst case with its extremely noisy CL spectrum, whereas with $N = 48$ performance are already reasonably close to the circular case.

For sake of comparison, on Fig. 3.6 also dispersion and confinement loss curves of a CTF with the values of R_{co} and t have also been reported. A direct comparison with the circular HLTF shows that the circular hypocycloid interface allows for a one order of magnitude CL reduction over both the considered transmission windows, thus confirming the experimental results reported in [47].

Great attention has been devoted in the literature also to the effects of the dielectric structs that connect the core boundary to the outer jacket [46,75,76]. In order to investigate the influence of the outer part of the cladding on the performance of ICFs, the structure shown in Fig. 3.7 is finally considered. This structure is obtained by taking the outer part of a TTLF-PT with N sides which has been cut at the contact points of its cladding tubes and then by adding it a circular hypocycloid core boundary. No jacket was considered in order to evaluate only the contribution of the outer cladding part. Figure 3.8 compares dispersion and confinement loss curves when the number N The CL reduction with respect to the simple HLTFs confirms that also external part of the cladding contributes to the reduction of the propagation loss. Once again this gain depends on the

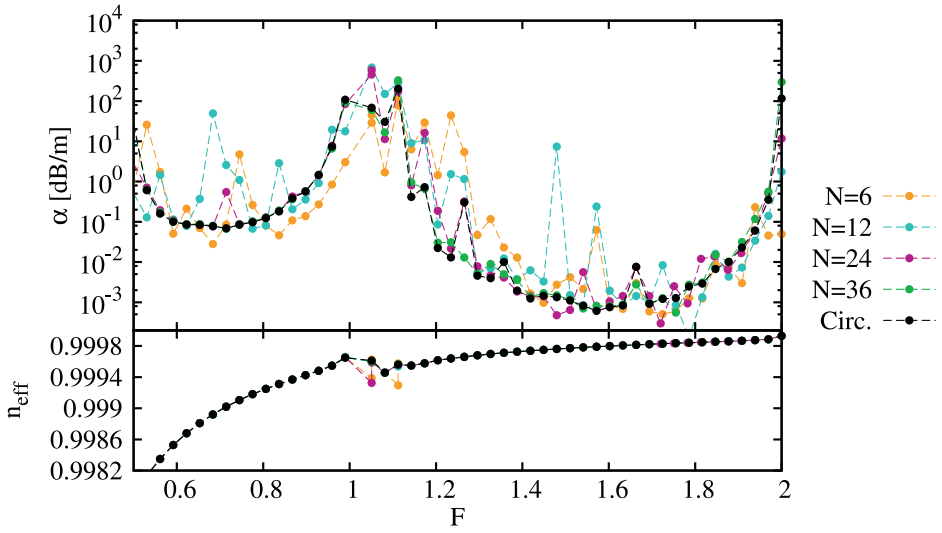

Figure 3.8: Confinement loss (top) and effective index (bottom) of the fundamental mode versus the normalized frequency F for hybrid TTLF-PTs with different number of sides N and an hypocycloid core boundary.

number N of sides, but in this case the convergence rate toward the best performance is much faster: $N = 24$ is, indeed, enough to obtain a CL spectra which is very close to the circular case. This reduced sensitivity on the number of the sides is connected to the reduced overlap of the core mode field with the external part of the cladding with respect to the part that is facing the core.
Comparing the similar TTLF-PTs from Fig. 3.4(b) and Fig. 3.8, the beneficial effect of the hypocycloid interface is clear. Thanks to it, indeed, even with $N = 6$ the CL spectrum is much smoother and closer to the ideal case than in the original TTLF-PT with $N = 6$ shown in Fig. 3.4(b).

3.5 Analysis of the curvature of the hypocycloid interface

In the previous section it has been shown that an hypocycloid core-cladding interface having circular arcs is very interesting since it is able to strongly reduce the CL even in KFs (or any TTLF-PT with low N). This hypocycloid interface

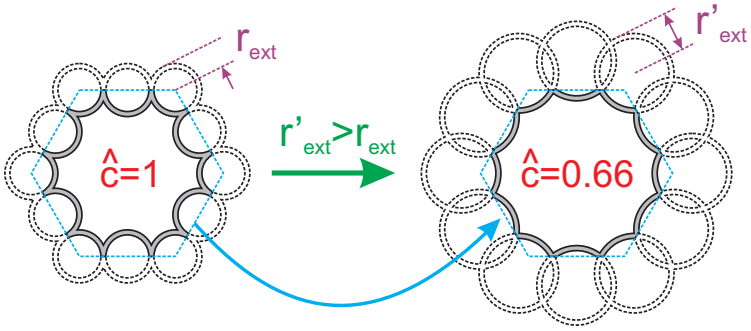

Figure 3.9: Cross sections of HLTFs with different curvatures of the core-cladding arcs; in clockwise: $\hat{c} = 1$, $\hat{c} = 0.5$, and $\hat{c} = 0$.

may be obtained during the final drawing step of the fiber by adjusting the internal pressure inside the core region [47]. However, a wrong pressure may cause different levels of curvature of the arcs, thus differing from the ideal circular shape shown above.

In this section the performances of HLTFs with different arcs curvatures are considered. As shown in Fig. 3.9, these HLTFs are still obtained by cutting a TTLF-CT cladding at the contacts points of its tubes, but in this case the external radius of the tubes, r'_{ext}, is bigger than r_{ext}. The curvature parameter $\hat{c}$ is defined as

$$\hat{c} = \frac{r_{ext}}{r'_{ext}}. \tag{3.4}$$

When the curvature is reduced, the arcs that constitute the HLTF tend to become straight lines. For $\hat{c} = 0$ the hypocycloid shape changes into a polygonal one. $\hat{c} = 1$ is the maximum value, because for values greater than 1, that is $r'_{ext} < r_{ext}$, the tubes do not touch each other any more. In general, owing to the building process through which these HLTFs are obtained, the R_{co} changes depending on the $\hat{c}$ parameter. As a consequence, by using the Marcatili's approximation given by Eq. (2.2), r_{ext} have been adjusted so as to have overlapping dispersion curves for the fundamental core modes.

Figure 3.10 compares HLTFs for different values of curvatures in terms of both dispersion curves and CL. As expected, the former are not affected by the change curvature due to the constant core size that was imposed on the considered

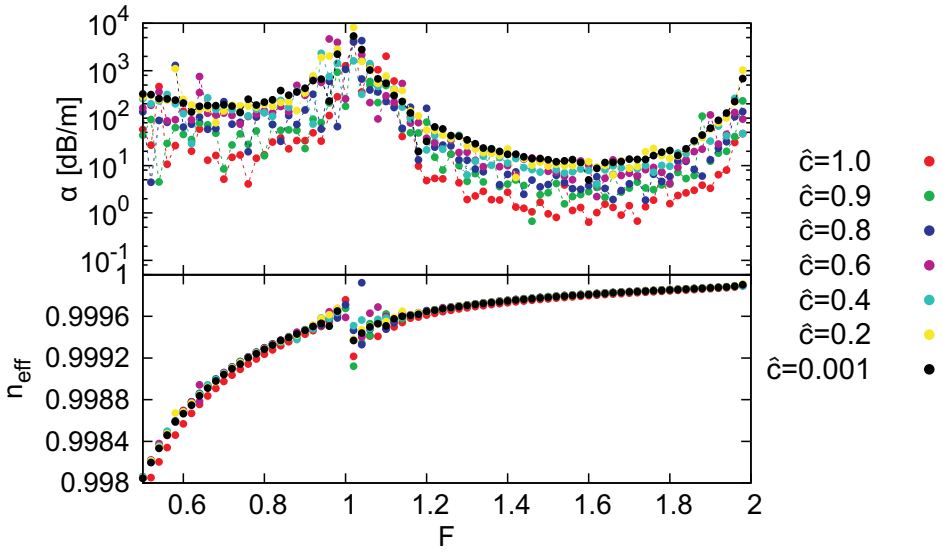

Figure 3.10: Comparison of dispersion curves (bottom) and CL (top) between HLTF with different levels of curvature of the core-cladding arcs.

structures. CL, on the contrary, is highly sensitive the $\hat{c}$ parameter: even if the curvature is slightly reduced, CL rapidly moves toward higher values. This sensitivity is stronger when $\hat{c}$ is close to one, whereas it tends to become weaker approaching zero. With $\hat{c} = 0.6$, for example, CL curve is already very close to the worst case ($\hat{c} = 0$). This confirms that the drawing of a TTLF-PT with an hypocycloid shaped core boundary, such as the one shown in [47], is a very critical task: the core pressure must be carefully controlled in order to exploit all the beneficial advantages offered by the hypocycloid shape.

3.6 Effects of the internal sustain on circular CTLFs

In chapter 2 it was shown that the waveguiding mechanism of TTLFs and CTLFs fibers does not depend on the particular arrangement of the cladding tubes. This allowed for a change of the initial triangular lattice structure (TTLF) to a circular one (CTLF) in order to achieve effectively single mode propagation. This change of the geometry shape is also very interesting from a manufacturing point of view, since the circular arrangement of the cladding tubes gives rise to a self

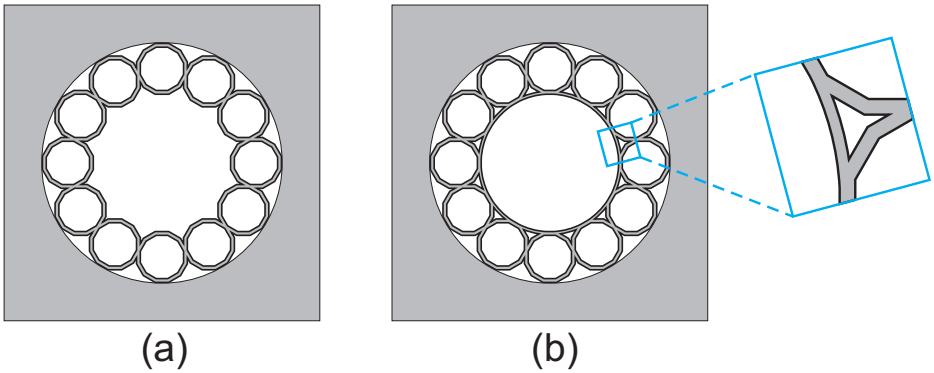

Figure 3.11: Cross section of two identical CTLF-PTs with (b) and without (a) internal sustain.

sustained structure. However, a question may arise asking whether or not an internal sustain can be considered in the CTLF in order to enhance the mechanical stability of the structure. In the first section of this chapter it was shown that a similar internal sustain for the kagome fiber does not produce any noticeable change. The purpose of this section is to answer that question by comparing the two CTLF-PTs structures shown in Figs. 3.11 (a) and (b). In all of these structures $n = 1.45$, $t = 500$ nm, $r_{ext} = 10$ μm and $no = 1$ giving a core size $R_{co} = 27.6$ μm. An infinite external jacket was also considered in the simulations for completeness.

At first, in Fig. 3.12 (a) CTLF-PTs with no internal sustain are compared by changing the number of sides (N) in the cladding's polygons. As shown previously for TTLF-PTs, the N value strongly affect the propagation loss spectrum. In general, the higher the number of the sides the lower and smoother the propagation loss, with the circular case representing the best case.

The effects of the internal sustain are shown in Fig. 3.12 (b). For the internal sustain $t = 500$ nm and $n = 1.45$ were considered in order not to perturb the spectral position of high loss regions (see Eq. (2.1)). Moreover, as shown by the inset of Fig. 3.11 (b), a complete overlap between the internal sustain and the cladding tubes was also assumed. Figure 3.12 (b) confirms that this internal sustain strongly perturb the performance of the initial structure shown in Fig.

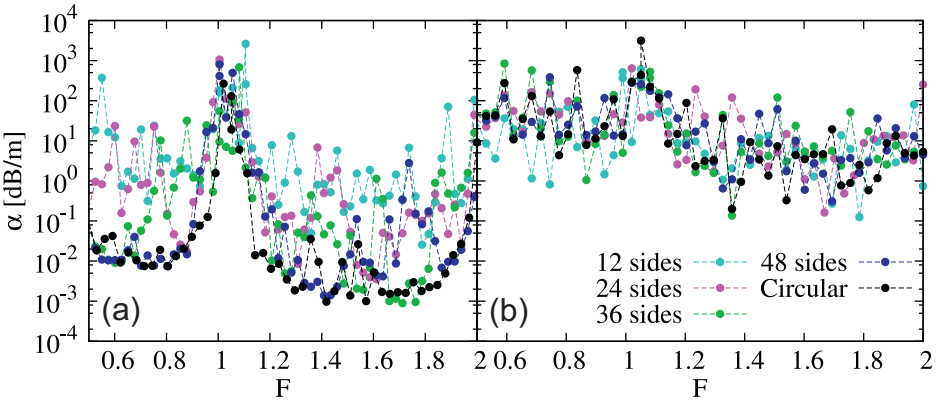

Figure 3.12: (a) Comparison of TTLF-PTs without the internal sustain with different number of cladding polygons' sides. (b) The same fibers considered in the (a) part but with an internal sustain added to the structure.

3.12 (a). In this case, indeed, the increase in the number of polygons' sides does not help in the reduction of the propagation loss, being the CL curves almost overlapping over the whole spectrum independently on the considered number of sides. As a consequence, even for the circular case, the internal sustain causes an increase of the propagation loss of 3 orders of magnitude in both of the considered transmission windows.

This suggests that internal sustains should be avoided in the manufacturing of CTLF-CT in order to reduce the propagation loss. However it should be noticed that, thanks to the circular arrangement of the tubes in the cladding, this structure is self-sustained which means that there is no need for any internal sustain, gluing or further drawing step to keep the cladding tubes in place. This interesting feature will be exploited in chapter 6 to manufacture a low loss and flexible waveguide for the THz spectral range.

In order to understand the reasons for the increased losses caused by the internal sustain, in Fig. 3.13 CTLF-CTs with and without internal sustain are compared to the performance of a stand alone CTF which represents the internal sustain of the fiber. Respective fibers' structures were reported in the same figure using the corresponding color for clarity. Figure 3.13 confirms that the CTLF-CT allows a reduction of the propagation loss with respect to the stand alone CTF.

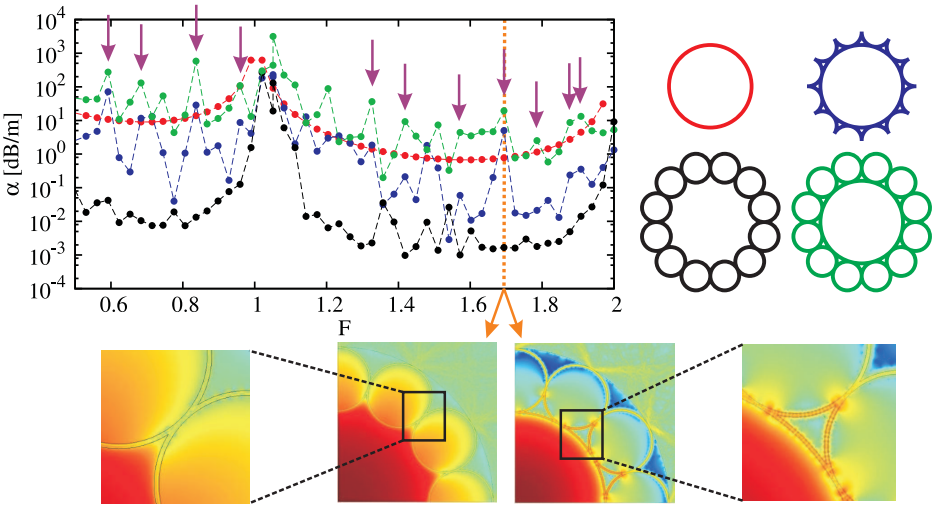

Figure 3.13: Comparison of the propagation loss between the internal sustain considered alone (red), the CTLF-CT (black), the CTLF-CT with internal sustain (green) and the internal sustain with external triangular elements (blue). Vertical violet lines highlight loss peaks similarities between the blue and green curve.

However, when the CTF is used as the internal sustain of the CTLF-CT, the propagation loss is strongly increased as to overlap with the performance of the internal sustain considered alone. The two insets shown in Fig. 3.13 compare the Poynting vector magnitudes (with a logarithmic scale) between CTLF-CTs with and without the internal sustain at $F = 1.7$. Low power intensity is found on the dielectric layer when no internal sustain is taken into account, as expected from the very low coupling between core and dielectric modes in the middle of the transmission windows (see chapter 2). However, when the internal sustain is inserted into the CTLF-CT structure, the power inside the dielectric layer is much increased with respect to the previous case highlighting an extra resonance between the core and dielectric modes. In particular, as shown by the inset of Fig. 3.13, these extra resonances concentrate an high amount of power on the triangular structures found between the internal sustain and the cladding tubes' contact points. Therefore, in Fig. 3.13 the performance of the CTF with these external triangular structures is also reported for comparison. As highlighted by

the violet arrows reported on the same figure, this structure and the CTLF-CT with the internal sustain share many resonance peaks across the considered transmission windows, especially in the low loss spectral regions. This confirms that the increase of the propagation loss in the CTLF-CT when the internal sustain is taken into account is due to the triangular shaped elements that are added to the cladding. Indeed, they bring many new resonances between core and dielectric modes that appear inside the transmission windows, thus compromising the performance of the fiber.

Chapter 4

Fano resonances in tube lattice fibers with polygonal tubes

In the analysis of the confinement mechanism of TTLFs and CTLFs given in chapter 2, it was shown that the properties of the whole fiber can be inferred from those of the tubes that constitute its cladding. This greatly simplified the analysis of the confinement mechanism and allowed for the formulation of a simple theoretical model able to predict the effects of cladding's physical and geometrical features on the performance of the guided core modes. The main advantage of this formulation rely on the fact that the modal analysis of the circular dielectric tube can be performed analytically [53, 54].

In chapter 3, however, it was shown that when the shape these circular tubes is perturbed, the confinement loss of the core modes rapidly worsen. In particular, by considering a polygonal shape for the cladding tubes, it was shown that the noisiness and the magnitude of the confinement loss spectrum can be controlled by changing the number N of sides in the polygons: the higher the number of the sides, the better the performance. Of course this behavior is extremely important from a manufacturing point of view, since it suggests how IC fibers's claddings

should be manufactured in order to minimize the propagation loss and obtain wide transmission bandwidths.

Therefore the purpose of this chapter is to deeply investigate the reasons of extra losses caused by the polygonal tubes in TTLF-PTs. Following the analysis performed in chapter 2, this work begins with the analysis of the stand alone polygonal dielectric tube. It has already been shown in the literature that a polygonal tube shape suffers from extra couplings inside the transmission bands [75, 76]. Such couplings can be detrimental for the fiber performances causing a degradation of the pulse propagating along the fiber [101] and an increase in the magnitude and noisiness of the CL spectrum. In [76], couplings are ascribed to the sharp corners of the polygonal shape which couple together several dielectric modes, allowing them to interact with the core mode. In [75] the better performances of the circular shape is ascribed to the constant dephasing of the bouncing cylindrical waves describing the core modes.

The analysis proposed in this chapter starts from the simple observation that these extra resonances in the polygonal tubes are due to the coupling between core and high azimuthal order dielectric modes. In particular, these couplings give a typical Fano resonance shape [102] in the CL spectrum which has already been found in a wide variety of optical structures [86, 103–106]. A theoretical model is then developed by using coupled mode theory analysis [107, 108] and by considering the polygonal shape as a perturbation of the circular one. Eventually this model allows to predict the relation between the spectral position of these extra Fano resonances and the number of sides in the polygon.

Finally also the tube lattice fibers with polygonal tubes introduced in the previous chapter are investigated. As expected, an high correlation between the spectral features of the stand alone polygonal tube and its relative TTLF-PT is found. This suggests that the theoretical model developed for the stand alone polygonal tube can be extended also to more complex hollow core fibers such as TTLFs. This is extremely important since, on one hand, this allows to define design rules for the manufacturing of complex ICFs and, on the other hand, it explains also the differences in performance between kagome and TTLF-CTs

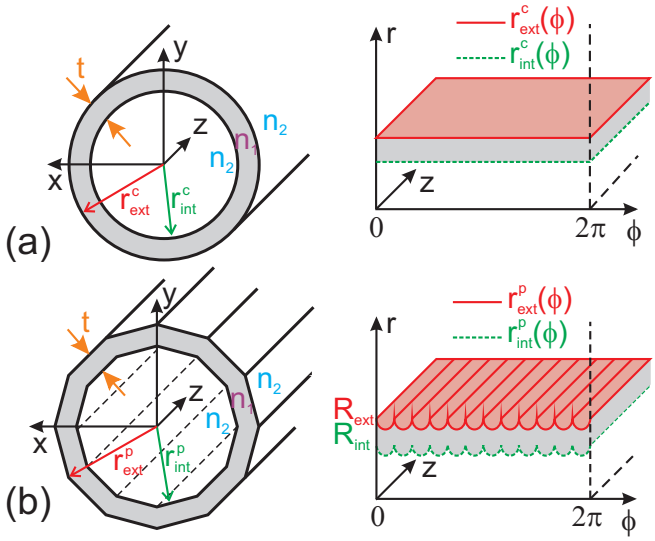

Figure 4.1: (a) Transverse cross section of a circular tube fiber (left) and its corresponding planar structure in cylindrical coordinates (right). (b) Transverse cross section of a polygonal tube fiber (left) and its corresponding planar structure in cylindrical coordinates (right). $r^{c,p}_{int}(\phi)$ and $r^{c,p}_{ext}(\phi)$ represent the distance between the center of the fiber and the internal or external edges of the circular and polygonal tubes, respectively; R_{int} and R_{ext} are the internal and external radii of the polygonal fiber, respectively.

found in chapter 3.

4.1 Outline of the waveguiding mechanism in tube fibers

Figure 4.1(a) show the typical transverse cross section of an hollow dielectric tube as presented in chapter 2. $t = 500$ nm and $r^c_{ext} = 5$ μm represent the dielectric's thickness and the external radius of the tube, whereas $n_H = 1.45$ is the refractive index of the dielectric material. The tube structure is supposed to be filled and surrounded by air whose refractive index is $n_L = 1$.

As shown in chapter 2, the stand alone tube structure supports two kind of modes: the core ones, that confine most part of their electromagnetic power inside the

hollow core [109–111] and the dielectric ones, that, on the other hand, confine most of their power in the dielectric ring [53]. In order to distinguish between them, a ^{co} superscript will be used for the former, whereas a ^{di} superscript will be used for the latter. In general, both core and dielectric modes can be classified as transverse, i.e. TE or TM, or hybrid, i.e. HE or EH. Each polarization is then provided with two subscripts, ν and μ, to account for the number of periods in the azimuthal direction and the number of local maxima and minima in the radial one.

In chapter 2 the confinement mechanism inside the hollow core of the circular tube was effectively described in terms of the coupling between core and dielectric modes. In particular, high CL peaks are found for the frequencies at which both phase matching condition and high overlap integral between the core and a dielectric mode are verified. Since core modes have low azimuthal dependence and an effective index which is always lower than n_L, the above conditions are satisfied only at the cutoff frequencies of dielectric modes with a low azimuthal index.

Dispersion and CL curves for the $HE^{co}_{1,1}$ (fundamental core mode) and the $TE^{co}_{0,1}$ modes are reported in Figs. 4.2 and 4.3 versus the normalized frequency (see Eq. (2.1)). CL increases approaching integer values of the normalized frequency, i.e. $F = \gamma$ with $\gamma \in \mathbb{N}$, which correspond to cut-off frequencies of the dielectric modes $HE^{di}_{1,\gamma}$ and $EH^{di}_{1,\gamma}$. Far from these frequencies CL decreases despite the extremely high density of dielectric modes, and this is due to their high azimuthal dependence which gives a negligible field overlap integral with the core modes.

4.2 Waveguiding characteristics of the polygonal tube fiber

In the polygonal tube fibers, the dielectric boundaries are polygons with N sides. An example with $N = 12$ is shown in Fig. 4.1(b). In these fibers, the distance of the internal and external edges from the center of the fiber, $r^{p}_{int,ext}$, vary with

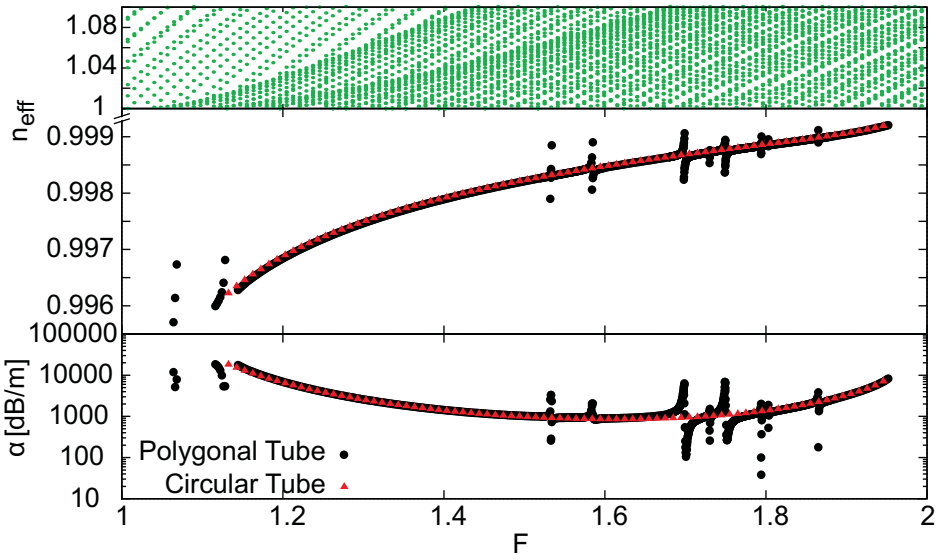

Figure 4.2: Top: Dispersion curves of the dielectric modes of the circular fiber. Middle and bottom: dispersion and CL spectra of the FM core mode of the circular (red triangles) and 24 sided polygonal (black circles) fiber.

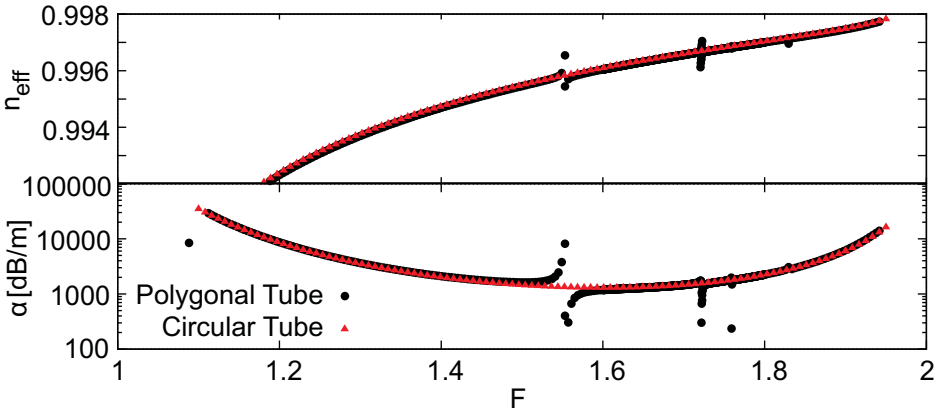

Figure 4.3: Top: dispersion curve of the $TE_{0,1}^{co}$ mode of the circular tube fiber (red triangles) and the polygonal one with $N = 24$ (black circles), respectively. Bottom: confinement loss of the $TE_{0,1}^{co}$ mode in both fibers.

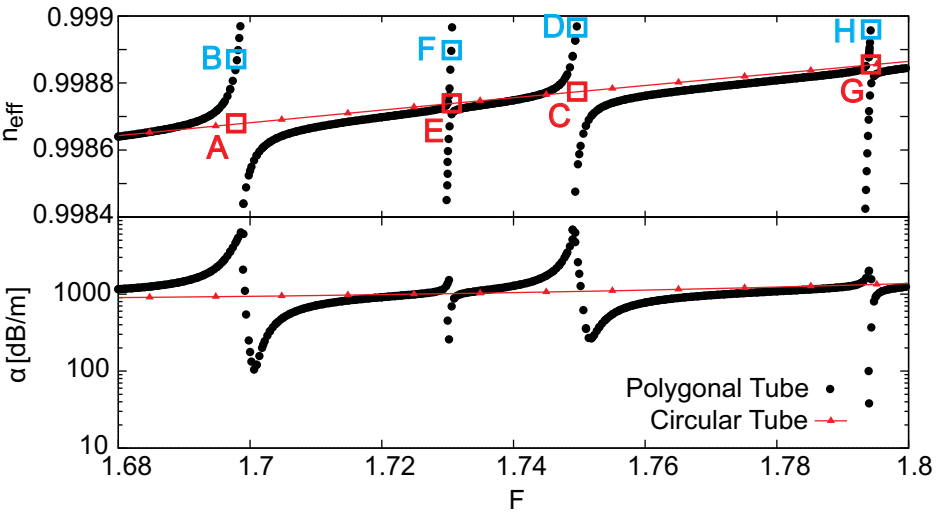

Figure 4.4: Details of the n_{eff} and CL curves reported in figure 4.2 between $F = 1.68$ and $F = 1.8$.

the azimuth angle ϕ according to:

$$\rho^{p}_{int,ext}(\phi) = R_{int,ext}\frac{\cos(\frac{\pi}{N})}{\cos\left[\mathrm{mod}\left(\phi,\ \frac{2\pi}{N}\right) - \frac{\pi}{N}\right]}, \tag{4.1}$$

where $R_{int,ext}$ is the internal or external radius of the polygon and the $\mathrm{mod}(x, y)$ function returns the remainder of the ratio x/y. Hereinafter, the core radius R_{co} of the polygonal fibers are assumed to be the mean value between the radius and the apothem of the internal polygon:

$$R_{co} = \frac{R_{int}}{2}\left[1 + \sin\left(\frac{\pi}{N}\right)\right]. \tag{4.2}$$

Dispersion and the confinement loss curves of the $HE^{co}_{1,1}$ and $TE^{co}_{0,1}$ modes for a polygonal tube fiber with $N = 24$ are reported in Figs. 4.2 and 4.3, respectively. Being the core size almost equal between the circular and polygonal tubes, dispersion curves and confinement loss are very close together. However, the polygonal fibers exhibits some additional sharp variations in both dispersion and CL curves. Details of the curves between $F = 1.68$ and $F = 1.8$ are reported in Figs. 4.4 and 4.5. These extra resonances in the CL curves present the typical asymmetric shape of Fano-type resonance [102] which have already been observed in several other optical structures such as gratings [103, 104], resonators [105], photonic

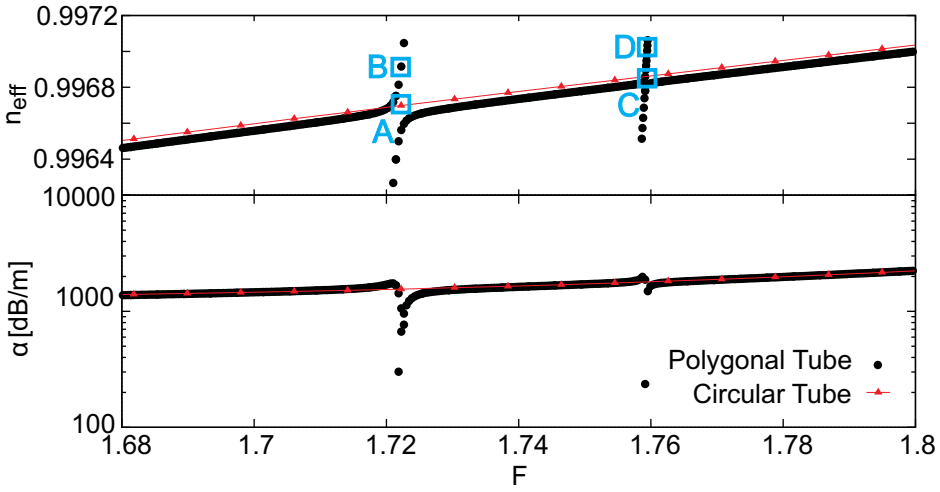

Figure 4.5: Details of the n_{eff} and CL curves reported in figure 4.3 between $F = 1.68$ and $F = 1.8$.

crystals [106] and solid-core photonic crystal fibers [86].

This phenomenon can be intuitively explained by considering the well known simplified model which describes the tube fibers in term of planar slabs [44,112,113]. As highlighted in Figs. 4.1(a) and (b), perfectly circular tubes correspond to perfectly planar slabs since the inner and outer radii are constant with ϕ. In polygonal tube fibers, on the contrary, radii are not constant with ϕ, so they correspond to corrugated slabs with a periodic surface variations along the second transverse direction. The core modes consist in plane waves bouncing back and forth by the dielectric slab which acts as a Fabry-Perot interferometer [44]. Its reflection coefficient is a slowly oscillating term with frequency whose amplitude depends on the difference between refraction coefficients n_H and n_L, whereas the period also depends on the slab thickness t. Low reflection frequencies correspond to cutoffs of the slab's modes, which are found for $F = \gamma$.

In the corrugated slab, similarly to photonic crystal slabs, the spectrum of the reflection coefficient of the corrugated slab is composed by two terms: a smoothly varying background and some sharp oscillations [106]. The former is the same of the planar slab, whereas the latter are due to extra couplings with modes the corrugated slab. The spectral position of these extra resonances depends

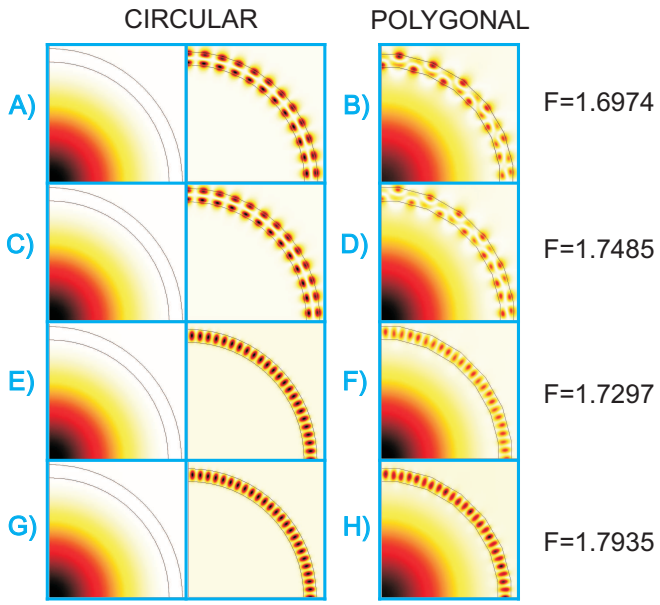

Figure 4.6: Intensity distribution on the transverse plane of the circular (left) and 24 sided polygonal (right) fibers at $F = 1.6974$ (A), (B); $F = 1.7485$ (C), (D); $F = 1.7297$ (E), (F); $F = 1.7935$ (G), (H).

on the dispersion curves of the slab modes, while the shape can be symmetric or asymmetric depending on the position of the background spectrum in which they appear. If they happen at a maxima or minima of the background spectrum they have symmetric Lorentz-line shape, in other cases they have asymmetric Fano-line shape [106].

By considering the high density of dielectric modes shown on the top of Fig. 4.2 and the performance of the core modes shown in Figs. 4.2 and 4.3, it is clear that, actually, only some dielectric modes are able to create extra resonances with the core modes. Field distributions of the modes involved in the resonances

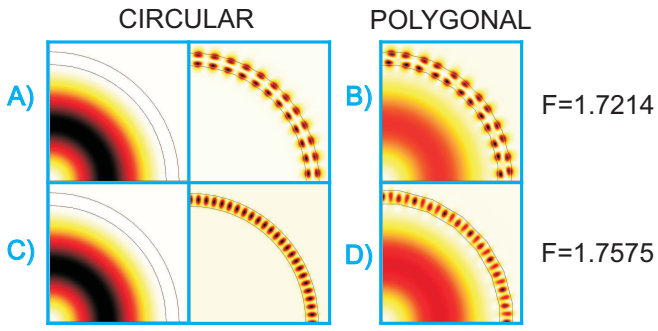

Figure 4.7: Intensity distribution on the transverse plane of the circular (left) and 24 sided polygonal (right) fibers at $F = 1.7214$ (A), (B); $F = 1.7575$ (C), (D).

with $HE^{co}_{1,1}$ of the polygonal fiber with $N = 24$ are reported in Fig. 4.6. In the polygonal fiber, the hybridization shows that these resonances are due to the coupling between the core mode and high azimuthal order dielectric modes with azimuthal number $\xi = \{23, 25, 47, 49\}$ that is $N \pm 1$, and $2N \pm 1$. In the circular fiber these resonances are absent and the modes are uncoupled. Fig. 4.7 performs a similar comparison for the $TE^{co}_{0,1}$ mode, showing that the resonances are due to the dielectric modes with $\xi = \{24, 48\}$ that is N, and $2N$. These results confirms that the azimuthal dependence of the dielectric modes involved in the Fano resonance is strictly connected with the number of sides N of the tube and the azimuthal dependence of the core mode. In order to understand the reason of these relations, an approach based on the coupled mode theory is followed in the next section.

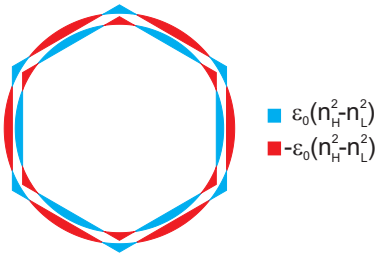

Figure 4.8: Example of the $\Delta\varepsilon(r,\phi)$ in the case of $N = 6$.

4.3 Coupled mode analysis of the polygonal tube

In order to investigate which dielectric modes are able to couple to the core ones and at which frequencies, coupled mode theory is here used [107, 108]. The polygonal tube fiber can be viewed as a circular one, with a perturbed dielectric permittivity profile. The perturbation $\Delta\varepsilon$ is defined as:

$$\Delta\varepsilon(r,\phi) = \varepsilon^p(r,\phi) - \varepsilon^c(r,\phi), \tag{4.3}$$

where

$$\varepsilon_c(r) = \begin{cases} \varepsilon_0 n_H^2, r_{int}^c < r < r_{ext}^c, \\ \varepsilon_0 n_L^2, \text{elsewhere}, \end{cases} \tag{4.4}$$

$$\varepsilon_p(r,\phi) = \begin{cases} \varepsilon_0 n_H^2, r_{int}^p(\phi) < r < r_{ext}^p(\phi), \\ \varepsilon_0 n_L^2, \text{elsewhere}, \end{cases} \tag{4.5}$$

are the dielectric permittivities on the transverse plane of the circular and the polygonal tube fiber respectively. $\Delta\varepsilon$ is a periodic function in ϕ, with a period of $2\pi/N$. Fig. 4.8 shows an example of $\Delta\varepsilon$ when $N = 6$. According to the coupled mode theory [107], such a perturbation causes a coupling between core and high order dielectric modes when the coupling coefficient

$$K_{co,di} = \frac{\tilde{K}_{co,di} - \tilde{K}_{di,di}\bar{c}}{1 - \bar{c}^2}, \tag{4.6}$$

is not null. In Eq. (4.6),

$$\tilde{K}_{a,b} = \frac{\omega}{4} \int_0^\infty \int_0^{2\pi} \Delta\varepsilon \left(\bar{E}_t^a \cdot \bar{E}_t^b - \frac{\varepsilon_c}{\varepsilon_c + \Delta\varepsilon} E_z^a E_z^b \right) r \, d\phi \, dr, \tag{4.7}$$

$$\bar{c} = \frac{1}{4} \int_0^{\infty} \int_0^{2\pi} (\bar{E}_t^{co} \times \bar{H}_t^{di} + \bar{E}_t^{di} \times \bar{H}_t^{co}) r \, d\phi \, dr; \tag{4.8}$$

where subscripts t and z indicate the transverse and longitudinal component of electric and magnetic fields of the circular tube fiber modes, respectively. A numerical integration of Eq. (4.6) is straightforward since both core and cladding modes of a circular tube fiber are known analytically [53, 110, 111]. However a more simple and useful formulation can be obtained through some considerations on the electromagnetic nature of the fields involved.

In IC fibers, the overlap between core and dielectric modes is extremely low [36, 49], thus

$$\bar{c} \simeq 0 \qquad \rightarrow \qquad K_{co,di} \simeq \tilde{K}_{co,di}. \tag{4.9}$$

By expressing electric field components in terms of separate functions and by exploiting the azimuthal periodicity of $\Delta\varepsilon(r, \phi)$, with simple but tedious algebraic manipulations reported in appendix A, it is possible to show that the coupling coefficient given by Eq. (4.7) is non-zero if

$$\xi = mN \pm \mu, \qquad m \in \mathbb{N}^+. \tag{4.10}$$

Therefore, Fano resonances appear at the cut-off frequencies of the dielectric modes whose azimuthal number is given by Eq. (4.10). These results are in agreement with what shown in [114] for elliptical fibers. In that paper, the elliptical shape is seen as a perturbation of the circular one with a perturbation function having two periods in the azimuthal direction. This causes extra couplings between fiber's modes whose azimuthal indices differ by ± 2.

From a practical point of view, a few more comments can be made on Eq. (4.10). In general, the analysis of core modes can be restricted to those with low azimuthal order (the other ones are of little practical interest), i.e. $\nu << mN$ (even when $m = 1$), which gives $\xi > 0$. This means that $TE_{0,\gamma}^{di}$ and $TM_{0,\gamma}^{di}$ modes are never involved in the extra resonances.

Fig. 4.9 shows the normalized cut-off frequencies F_c of the modes $HE_{\xi,\gamma}^{di}$, $EH_{\xi,\gamma}^{di}$ with $\gamma = \{1, 2, 3\}$. The normalized cut-off frequencies increase as ξ increases. As a consequence, by increasing the number of side N of the polygon, the frequen-

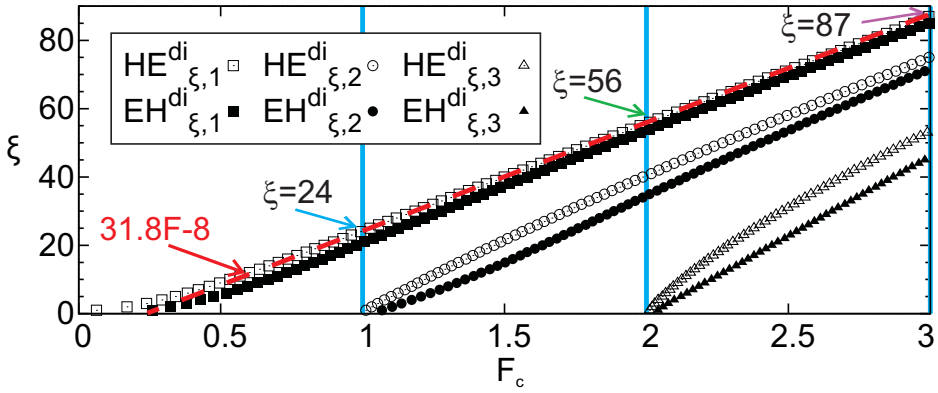

Figure 4.9: Normalized cut-off frequencies of the dielectric modes $HE^{di}_{\xi,\gamma}$, $EH^{di}_{\xi,\gamma}$ with $\gamma = \{1, 2, 3\}$.

cies of the Fano resonances increase. It is thus always possible obtain a spectral region without resonances, provided that N is high enough. To accomplish this task, it should be noticed that for a given ξ, the $HE^{di}_{\xi,1}$ mode has always the lowest normalized cut-off. If ξ^{F_q} is the azimuthal index of the first $HE^{di}_{\xi,1}$ mode with $F_c > F_q$, from Eq. (4.10) it follows that to have no Fano resonances in the range $0 < F < F_q$, it must be

$$N > \xi^{F_q} + \mu. \tag{4.11}$$

Figure 4.9 highlights also that for $F_c > 0.4$, the cutoff frequencies increase linearly with ξ:

$$\xi^{F_q} \simeq \text{nint}\left[aF_q - b\right], \tag{4.12}$$

where $nint[x]$ is the nearest integer to real number x, while $a = 31.8$ and $b = 8$ are parameters that depend on the geometrical and physical properties of the circular tube used as a reference and they were obtained by fitting the numerical cutoffs' curve. By substituting Eq. (4.12) into Eq. (4.11), it yields:

$$N(F_q) > \text{nint}\left[31.8F_q - 8\right] + \mu. \tag{4.13}$$

For example, by considering the fundamental core mode, i.e. $HE^{co}_{1,1}$, N must be greater than 25, 57, and 88 in order to have a Fano resonance free spectral region $F \in [0; F_q]$ with $F_q = \{1, 2, 3\}$, respectively.

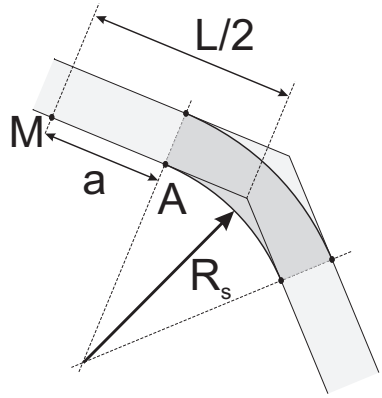

Figure 4.10: Detail of a polygonal fiber with rounded corner.

For the same reasons described above, also the spectral density of the Fano resonances, which is the number of extra resonances lying in a given frequency range, decreases as N increases. Moreover, by increasing N, the perturbation $\Delta\varepsilon$ becomes weaker because the difference between the arc and the polygon side reduces and thus the coupling coefficient tends to zero.

Finally, as shown in appendix A, Eq. (4.10) does not depend on the shape of the perturbation provided that it is periodic with ϕ. This means that also polygonal fibers with rounded corners as shown in Fig. 4.10, and thus with a constant dielectric thickness, are affected by Fano resonances.

4.4 Validation of the polygonal stand alone tube model

In order to validate the model proposed in the previous section, at first a polygonal tube with $N = 24$ has been was taken into account. The transmission characteristics of the first two core modes, $HE^{co}_{1,1}$ and $TE^{co}_{0,1}$, in the range $F \in [0; 3]$ are reported in Figs. 4.11 and 4.12, respectively. On the top of both figures only dispersion curves of the dielectric modes which satisfy Eq. (4.10) with $m = \{1, 2, 3\}$ modes have been reported. Vertical lines highlight the relation the cutoff of the dielectric modes and the Fano resonances in the loss spectrum of the core modes. Eq. (4.10) is perfectly able to predict the spectral positions of all Fano

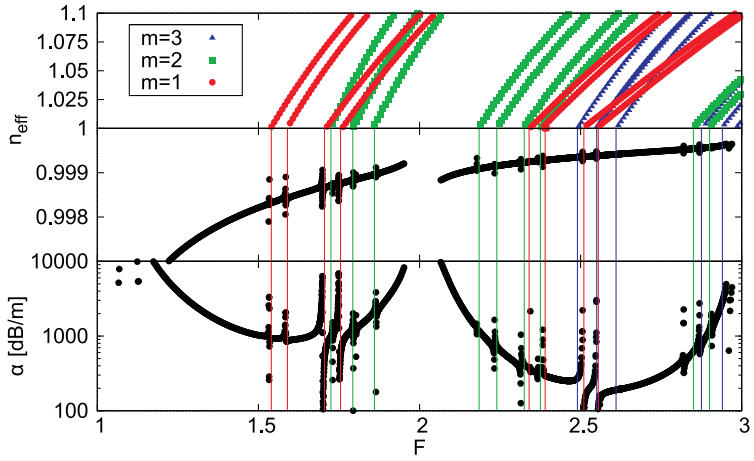

Figure 4.11: Performances of a tube fiber with $N = 24$. Top: dispersion curves for the dielectric modes with azimuthal index $\xi = m24 \pm 1$ and $m = 1$ (red circles), $m = 2$ (green squares) and $m = 3$ (blue triangles). For a given value of m there are both HE and EH modes with different radial index γ. Middle and bottom: n_{eff} and CL spectra of the FM $HE^{co}_{1,1}$. Vertical lines show cutoff frequencies for the cladding modes involved in the coupling.

resonances.

As pointed out in the previous section, when N is reduced, the Fano resonances shift toward lower frequencies and their spectral density increase. This is confirmed by observing the case with $N = 12$ reported in Fig. 4.13. The resonance frequencies are spectrally denser than in the $N = 24$ case, thus resulting in noisier CL curves for the core mode. By reducing N, the perturbation becomes stronger and some resonances due to dielectric modes with $m \geq 3$ appears, even though their dispersion curves and cutoff lines have not been reported on the figure for sake of clarity.

Conversely, when N is increased, Fano resonances shift toward higher frequencies and their spectral density decreases. The case with $N = 57$ is reported in Fig. 4.14. Due to the high number of sides in the polygon, the perturbation function tends to zero, therefore the intensity of the coupling reduces and the resonances' bandwidths become very narrow. However, as expected from Eq. (4.13), no Fano resonances are found for $F \leq 2$.

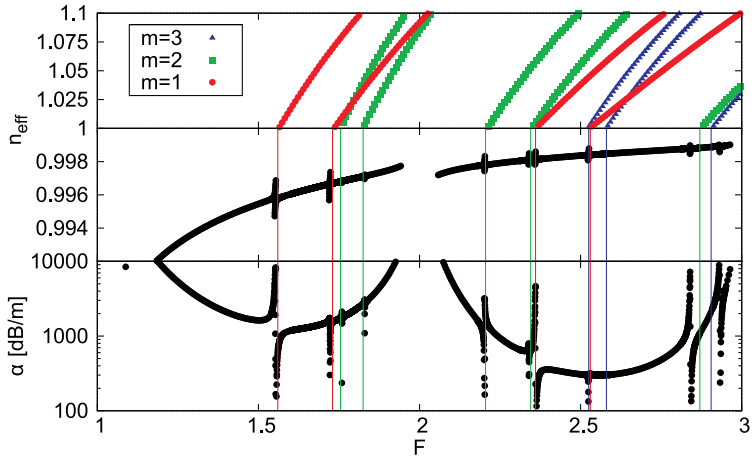

Figure 4.12: Performances of a tube fiber with $N = 24$. Top: dispersion curves for the dielectric modes that has an azimuthal index $\xi = m24$ and $m = 1$ (red circles), $m = 2$ (green squares) and $m = 3$ (blue triangles). For a given value of m there are the HE and EH modes with different radial index γ. Middle and bottom: n_{eff} and CL spectra of the $TE^{co}_{0,1}$ mode. Vertical lines show cutoff frequencies for the cladding modes involved in the coupling.

As it has been shown in chapter 2, the spectral distribution of dielectric modes on the circular tube fiber depends only on the $\rho = r^c_{int}/r^c_{ext}$ geometrical parameter and on the refractive indices n_H and n_L involved on the confinement mechanism. This means that, working with the normalized frequency defined by Eq. (2.1), spectral position of Fano resonances are not changed when tubes with different absolute dimensions but identical R_{co}/t ratio are considered. This is shown by Fig. 4.15 which compares CL performance of three 24 sided TFs with the same R_{co}/t ratio and $t = \{0.5, 1, 2\}$ μm. As expected from the Marcatili's approximation on Eq. (2.2), the three fibers exhibit the same dispersion curve for the core modes since it scales as R_{co}/t. On the contrary, CL reduces as t is increased because it scales as t^3/R^4_c [109].

Finally, it should be noticed that Eq. (4.10) holds for any kind of azimuthal periodic perturbation, thus also polygonal TFs with rounded corners are affected by Fano resonances. A detail of a rounded corner is shown in Fig. 4.10. The smoothing arc has an internal radius R_s, thickness t and it is tangent to the

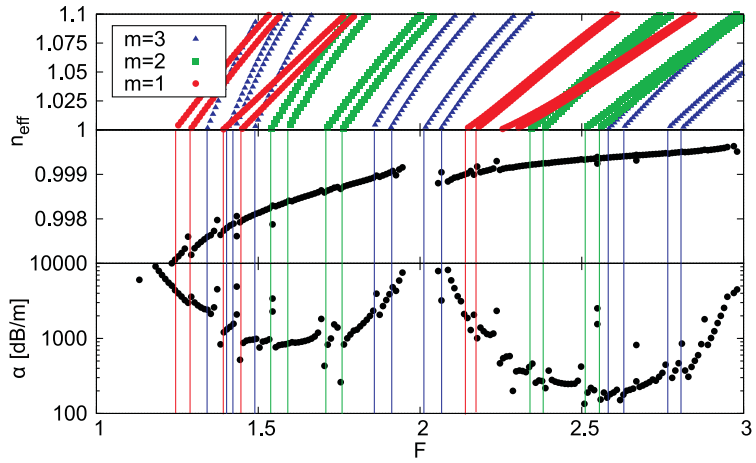

Figure 4.13: Performances of a tube fiber with $N = 12$. Top: dispersion curves for the dielectric modes with azimuthal index $\xi = m12 \pm 1$ and $m = 1$ (red circles), $m = 2$ (green squares) and $m = 3$ (blue triangles). For a given value of m there are the HE and EH modes with different radial index γ. Middle and bottom: n_{eff} and CL spectra of the FM $HE^{co}_{1,1}$. Vertical lines show cutoff frequencies for the cladding modes involved in the coupling.

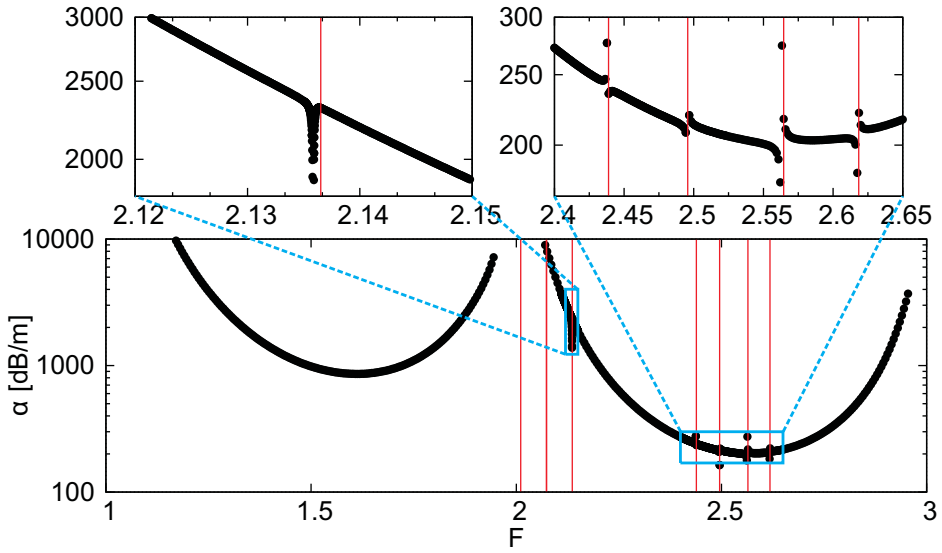

Figure 4.14: Performances of a tube fiber with $N = 57$. CL for the FM $HE^{co}_{1,1}$. Vertical lines represent the cutoff for the dielectric modes with azimuthal index $\xi = m57 \pm 1$ and $m = 1$. The insets show details of the resonances.

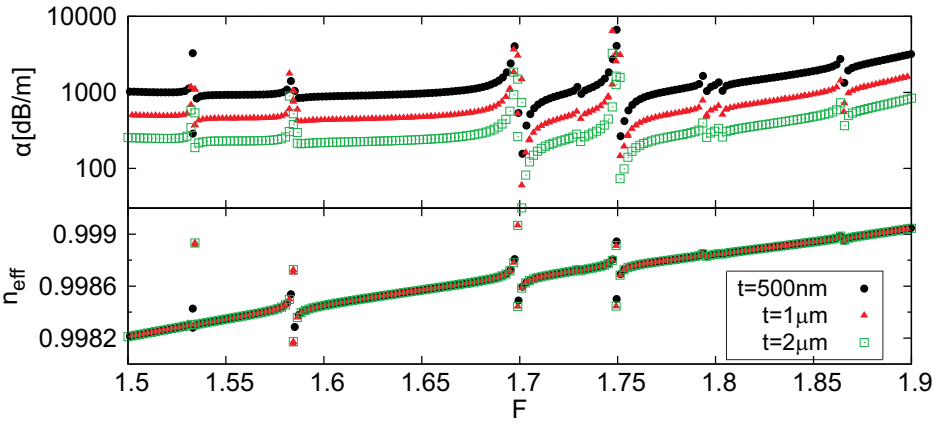

Figure 4.15: Details of n_{eff} and CL spectra of 24 sided tube fibers with identical R_c/t ratios and thickness of 500 nm (black circles), 1 μm (red triangles) and 2 μm (green squares).

polygon's sides whose length is L. In this way the dielectric thickness is always constant along the border of the tube. By changing the distance a from the tangent point A to the midpoint of the side M, it is possible to change the normalized smoothness:

$$s = 1 - \frac{2a}{L}, \tag{4.14}$$

from 0 (inner polygon with sharp corners) to 1 (inner and outer polygons perfectly circular). In Fig. 4.16 a detail of dispersion and CL curves between $F = 1.55$ and $F = 1.85$ for a polygonal tube fiber with N=24 and rounded corners are reported for two different values of s: $s = 0$ and $s = 0.5$. As expected, Fano resonances are still present and their spectral positions do not significantly differ from those of the polygonal fiber with sharp corners. However, for $s \to 1$, the fiber's perturbed shape tends to the ideal circular case, thus the coupling becomes weaker and the resonances narrower.

Owing to the general formulation of the proposed model, it can also been applied to the analysis of Fano resonances which are caused by variations in the tube thickness. For sake of examples, the spectral characteristics of a tube fiber whose

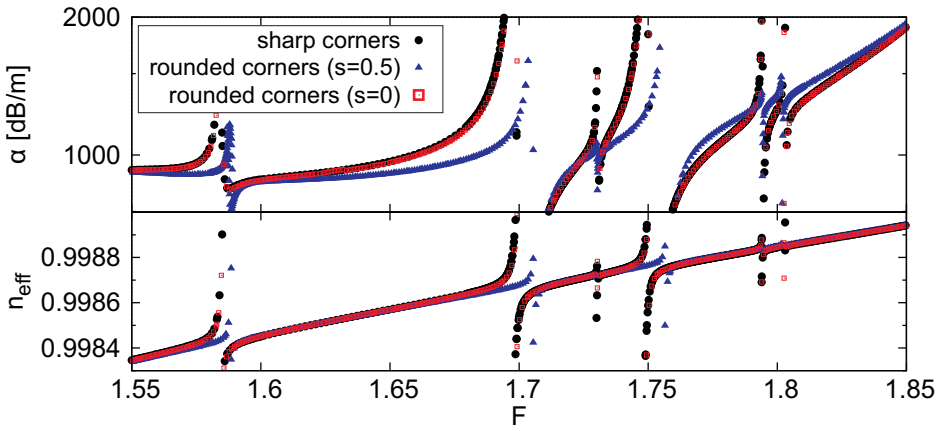

Figure 4.16: Details of n_{eff} and CL spectra of 24 sided tube fibers with sharp corners (black circles) and with smoothed corners with $s = 0$ (red squares) and $s = 0.5$ (blue triangles).

internal and external edges defined as:

$$r^s_{int}(\phi) = r^c_{int}(\phi)\,[1 - \delta\cos(24\phi)] \tag{4.15}$$

$$r^s_{ext}(\phi) = r^c_{ext}(\phi)\,[1 + \delta\cos(24\phi)] \tag{4.16}$$

are shown in Fig. 4.17, with $\delta = 4.25 \cdot 10^{-3}$. Both dispersion and CL curves clearly show the Fano resonances due to the dielectric modes with $m = 1$. Higher order resonances ($m > 1$) are too weak to be seen with the scale used for the figure, except for the resonance with $m = 2$ at $F = 1.7225$. This is due to the fact that with this kind of perturbation, the functions $I_{z_{i,j}}(\phi)$ reported on appendix A are very close (even though not perfectly equal) to sinusoidal functions.

4.5 Solid core polygonal tube fibers

The analytical model developed in the previous sections for the prediction of the spectral position of extra Fano resonances in polygonal tubes is absolutely general and it is not limited to hollow core (HC) tubes. In order to show its general validity, solid core (SC) IC fibers are here considered. Their generic structures are still represented by Figs. 4.1(a) and (b), but in this case the dielectric tube is filled and surrounded by a dielectric material whose refractive

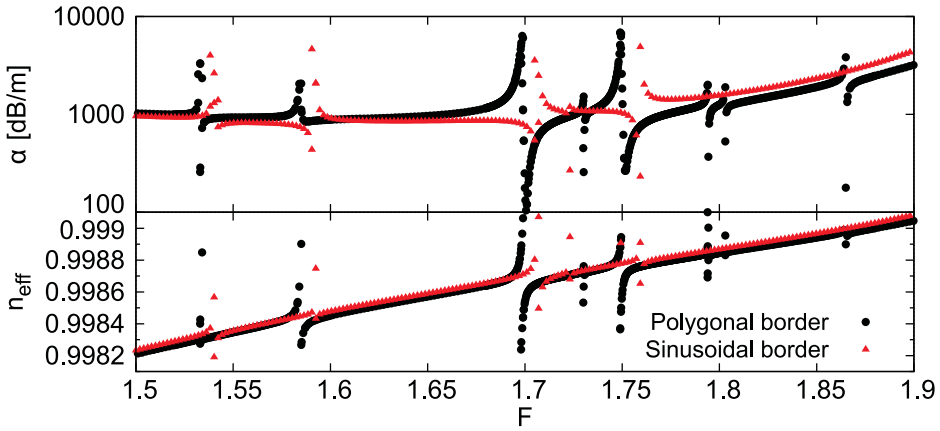

Figure 4.17: Details of n_{eff} and CL spectra of a 24 sided polygonal TF (black dots) and a TF with a sinusoidal borders (red triangles).

index n_L is higher than air, i.e. $1 < n_L < n_H$.

Figure 4.18(a) compares confinement loss of a SC-CTF and a SC-PTF with $N = 12$ sides and with $n_H = 1.47288$, $n_L = 1.457$, $r^c_{ext} = 5.25$ μm and $t = 472.5$ nm. As expected, the SC-PTF has some additional asymmetric shaped peaks due to the extra-resonances between the fundamental mode are the hybrid modes $HE_{\xi,\gamma}$ and $EH_{\xi,\gamma}$ with azimuthal index ξ given by Eq. (4.10), which can be rewritten as:

$$|\xi - mN| = 1, \qquad m \in \mathbb{N}. \tag{4.17}$$

Figure 4.18(b) shows the cutoff normalized frequencies of the ring modes $HE^{ri}_{\xi,\gamma}$ and $EH^{ri}_{\xi,\gamma}$ with $\gamma = \{1, 2\}$ computed for the SC-CTF under analysis.

It should be noticed that, for a solid core tube fiber $(n_H - n_L)/n_H << 1$, which means that the perturbation function $\Delta\varepsilon$ given by Eq. (4.3) is much reduced in amplitude with respect to the hollow core case. As a consequence the coupling strength between core and high order dielectric modes is also reduced. Moreover, for $\xi \geq 2$, hybrid modes to degenerate into linearly polarized modes:

$$LP^{di}_{\xi,\gamma} \longleftrightarrow HE^{di}_{\xi+1,\gamma}, EH^{di}_{\xi-1,\gamma}. \tag{4.18}$$

Due to the weakness of the coupling, only $LP^{di}_{mN,\gamma}$ modes give rise to non-negligible Fano resonances, because they are composed of hybrid modes both

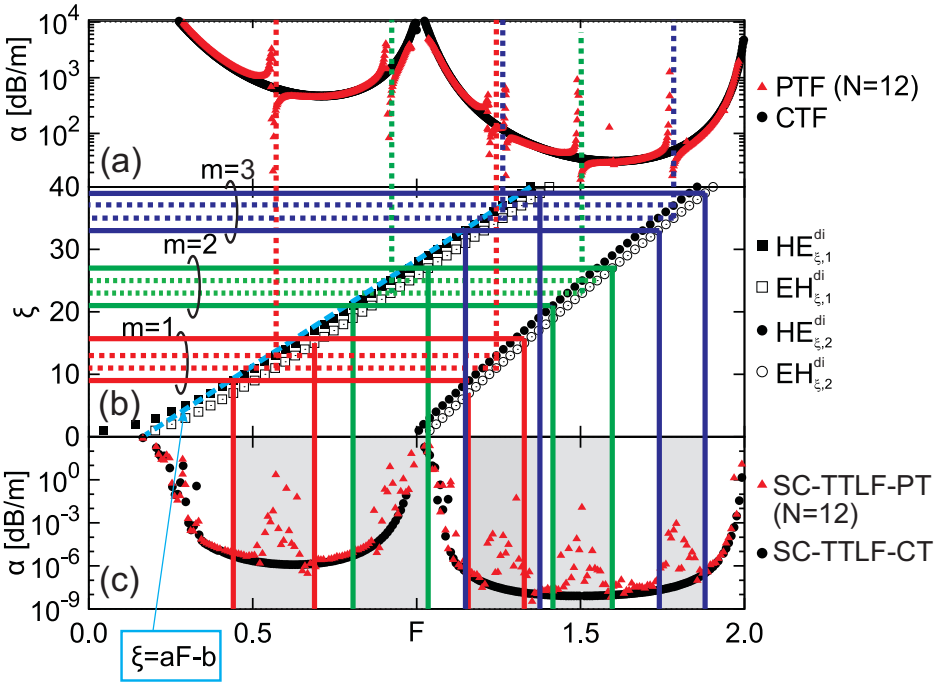

Figure 4.18: (a) Comparison of the confinement loss spectra of a circular (black dots) and a 12-sided polygonal (red triangles) tube fibers. (b) Cutoff frequencies for the dielectric modes of the circular tube fiber. Dotted vertical lines highlight the tubes modes which cause Fano resonances in tube fiber according to Eq. (4.17). Solid vertical lines highlight the cladding modes which defines the boundaries of the Fano resonances regions according to Eq. (4.24) with $\bar{\mu} = 3$. Red, green, and blue colors are used for $m = 1$ and $m = 2$, respectively. (c) Comparison of the confinement loss performance between a SC-TTLF-CT (black dots) and SC-TTLF-PT with $N = 12$ (red triangles).

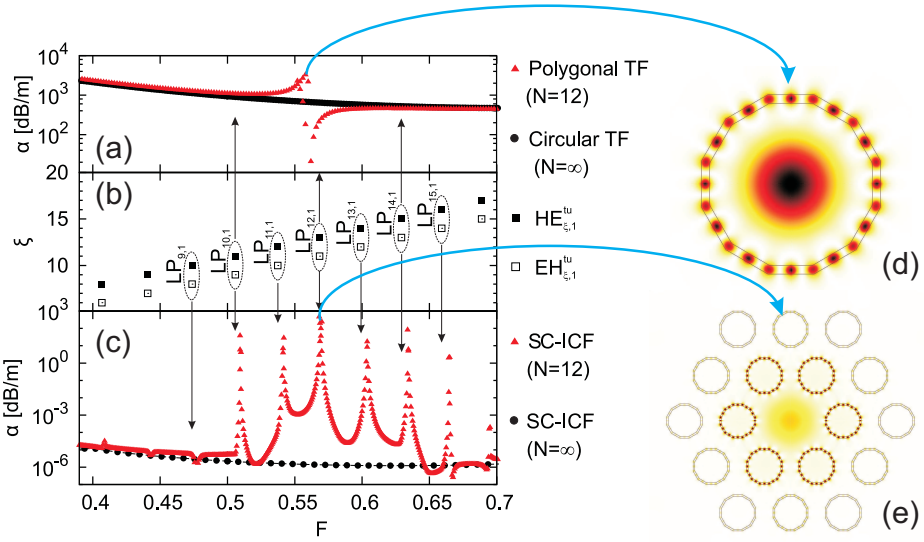

Figure 4.19: (a,b,c) Zoom of Fig. 4.18(a),(b) and (c) for $F \in [0.39; 0.75]$. In (b) the degeneration of the $HE^{di}_{\xi+1,\gamma}$ and $EH^{di}_{\xi-1,\gamma}$ modes composing the $LP^{di}_{\xi,\gamma}$ modes is highlighted. The z-component of the Poynting's vector of the guided mode at $F = 0.569373$ of the PTF (d) and PTLF (e) both with $N = 12$.

satisfying Eq. (4.17). In $LP^{ri}_{mN-1,\gamma}$ and $LP^{di}_{mN+1,\gamma}$ modes, only one of the two hybrid modes satisfies Eq. (4.17), thus the resonances are much lower and they are not visible with the scale used in Fig. 4.18. A detail of the resonance with the $LP^{di}_{12,1}$ mode is reported in Fig. 4.19(a) while Fig. 4.19(d) clearly shows the hybridization between the core mode $HE^{co}_{1,1}$ and the ring $LP^{di}_{12,1}$ mode at $F = 0.569373$. Therefore, vertical dotted lines reported on Fig. 4.18(a) correspond to the cutoff frequencies of the $HE^{ri}_{mN+1,\gamma}$ and $EH^{ri}_{mN-1,\gamma}$ modes ($LP_{mN,\gamma}$) satisfying Eq. (4.17) with $m = 1$ (red lines), $m = 2$ (green lines), and $m = 3$ (blue lines).

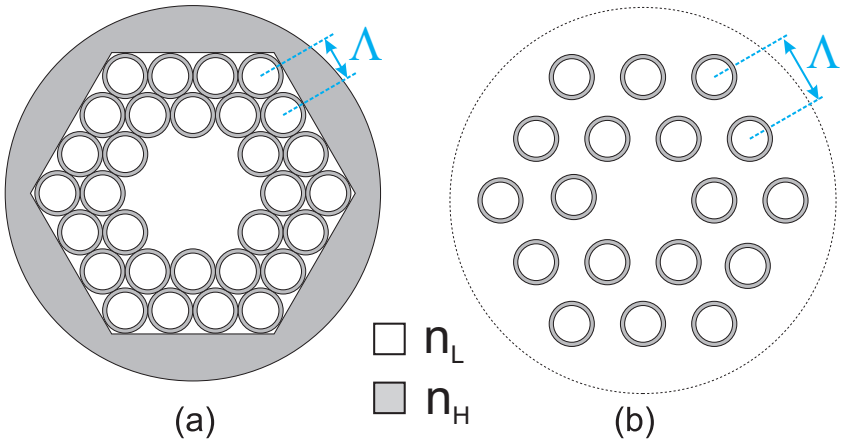

Figure 4.20: (a,b) Cross sections of an HC-TTLF and a SC-TTLF respectively, with circular tubes in the cladding. White and gray regions represent low refractive index (n_L) background material and high index (n_H) one respectively.

4.6 Effects of the polygonal tubes in solid and hollow core TTLFs

In chapter 2 it was shown that the spectral properties of TTLF-CTs can be derived by from those of the circular tubes that constitute their cladding. In chapter 3, it was numerically shown that when the circular shape of these cladding tubes is changed to a polygonal one, the core mode experiences extra losses thus compromising the performance of the fiber. Interestingly these extra losses are connected on the number N of sides in the cladding polygons: the higher N the smoother and lower the CL spectrum of the core mode. In order to provide a theoretical explanation of this effect, the results obtained above for the stand alone polygonal tubes are here used to investigate extra losses in ICFs whose cladding is based on a triangular lattice of tubes. Once again, the model developed here does not rely on a particular choice for the refractive indices n_H and n_L (provided that $1 \leq n_L < n_H$), thus both solid (SC) and hollow core (SC) TTLFs are considered, keeping the analysis as general as possible.

SC-TTLFs [86,87] and HC-TTLF [52] structures are very similar and their typical cross sections are shown in Figs. 4.20(a) and (b), respectively. In both cases

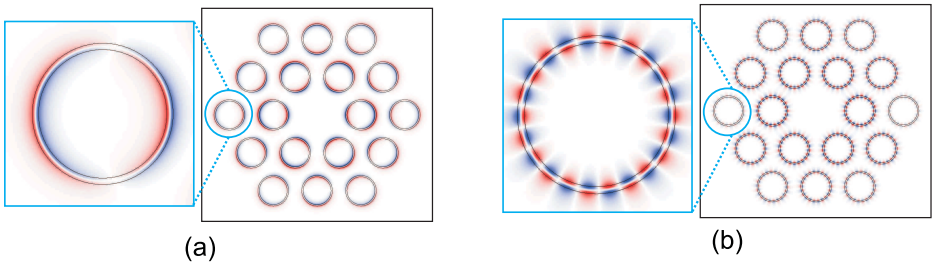

Figure 4.21: E_ϕ field component for the cladding ring modes $HE^{ri}_{1,2}$ (a) and $LP^{ri}_{11,2}$ (b) respectively.

claddings are composed of a regular arrangement of circular tubes with external radius r^c_{ext}, thickness t and refractive index n_H, separated by a pitch Λ and immersed in a uniform dielectric background with lower refractive index n_L. In the HC-TTLFs, the background material is air ($n_L = 1$), and the tubes must be in contact with each other, thus r^c_{ext} and Λ are bounded each other. In the SC-TTLFs, on the contrary, the background material has a refraction index $n_L > 1$. In this case mechanical stability of the fiber is not a problem, thus Λ can have any desired value. Typically, for HC-TTLFs, also an external jacket that surrounds the cladding tubes is added in order to enhance the mechanical stability of the entire structure. In this chapter its refractive index will be assumed equal to n_H for simplicity.

As shown in chapter 2 and in [86], the confinement mechanism of these fibers can be completely described in terms of the coupling between core ($n_{eff} < n_L$) and dielectric modes ($n_L \leq n_{eff} < n_H$). The latter can be described in terms of a combination of the dielectric modes of the single tubes composing the cladding as highlighted in Figs. 4.21(a) and (b). Therefore, by using the same naming convention adopted for the stand alone tube, dielectric modes of TTLFs can be classified in $HE^{di}_{\xi,\gamma}$, $EH^{di}_{\xi,\gamma}$, $TE^{di}_{0,\gamma}$ and $TM^{di}_{0,\gamma}$. As for the SC-TF, in the SC-TTLF usually $|n_H - n_L|/n_H << 1$ and ring modes can be described in terms of the linearly polarized $LP^{ri}_{\xi,\gamma}$ modes, whereas this approximation is no longer valid in HC-TTLF because the step index is much higher.

In order to show the effects of polygonal tubes in TTLFs, the solid core case

is here considered, since the bigger Λ allows a clearer identification of the resonances with the cladding ring modes. Figure 4.18(c) shows a comparison between the confinement loss of a SC-TTLF with circular (SC-TTLF-CT) and polygonal tubes (SC-TTLF-PT) with $N = 12$. Physical and geometrical features of the cladding's tubes are still those of the previous section ($n_H = 1.47288$, $n_L = 1.457$, $r^c_{ext} = 5.25$ μm, $t = 472.5$ nm) for a clearer analysis, while $\Lambda = 15$ μm [87].

As expected, in the SC-TTLF-CT the confinement loss smoothly varies with frequency depending on the coupling between the core and the dielectric modes. Such coupling depends on two factors: the difference between the effective indices of core and ring modes, and the field integral overlap between them. The effect of the former is maximized at the crossing point between the dispersion curves of the two involved modes (phase-matching condition). Since ICFs work in the large core regime, $n_{eff} \lesssim n_L$, thus the crossing frequencies can be well approximated by the cutoff frequencies of the dielectric modes. The modes overlap depends on spatial variation of the dielectric modes along the tubes circumferences: the higher the periodicity, the lower the coupling. Figures 4.21(a) and (b) show the azimuthal field components of the electric field (E_ϕ) of two dielectric modes with low and high spatial dependence, respectively. The former is the $LP^{di}_{0,1} \leftrightarrow HE^{di}_{1,1}$ mode which gives rise to high coupling with core mode at its cutoff frequency $F = 1$. The latter is the $LP^{di}_{11,2}$ mode which is composed of $EH^{di}_{10,2}$ and $HE^{ri}_{12,2}$ modes and, conversely to the previous one, its coupling with the core mode is weak due its high spatial dependence along the tubes boundary. For this reason, the confinement loss variation at its cutoff frequency $F = 1.54$ is negligible.

As expected from the analysis of chapter 3, Fig. 4.18(c) shows that when the circular shape of cladding tubes is changed to a polygonal one, extra losses appear. However, from a direct comparison between the SC-PTF in Fig. 4.18(a) and the SC-TTLF-PT of Fig. 4.18(c) it is clear that there is a correlation between the performance worsening the in stand alone tube and in the ICF, even though the effect on the ICF is spectrally wider. Figure 4.19(c) reports a detail of the loss in the spectral region $F \in [0.39, 0.75]$, showing that the widening is due to the resonance of the fundamental mode with a multiplicity of modes and

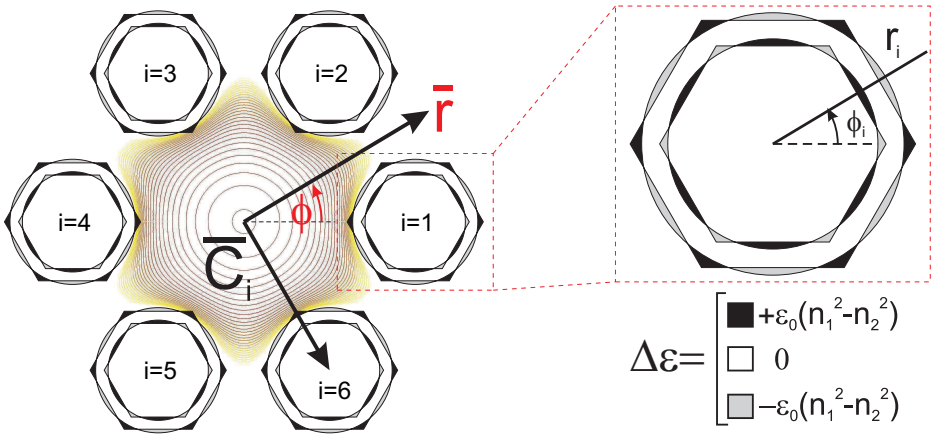

Figure 4.22: (a) Example of perturbation function for a TTLF-PT with $N = 6$. The z-component of the Poynting vector for the fundamental mode is also shown on log scale. The inset shows the perturbation function for a generic cladding tube, with the local reference system centered at its center.

not only with the $LP^{di}_{12,1}$ one. The same behavior holds for all the additional resonances, although they are not reported here for sake of brevity. However, as for the stand alone polygonal tube case, this highlights that the azimuthal index ξ of the resonant ring modes that couple to the core one is still strictly connected with N. The reason for the growth in the number of modes involved in the resonances is investigated in the next section and it is related to a much more complex core-cladding interface in ICFs with respect to the stand alone tubes.

4.7 Analytical model for TTLFs with polygonal tubes

As for the stand alone polygonal tubes, coupled mode theory [107, 108] is here used to investigate which dielectric modes are able to couple to the core one. For this purpose the TTLF-PT can be seen as the perturbed version of a TTLF-CT. Figure 4.22 shows an example with $N = 6$.

As shown previously for the stand alone tube, in ICFs the overlap between

core and dielectric modes is quite low thus their coupling can still be computed through Eq. (4.7), where for the TTLFs case ε^c is the dielectric permittivity of the TTLF-CT, and $\Delta\varepsilon$ is the perturbation function shown in Fig. 4.22(a).
In order to find which dielectric modes are able to give a not null coupling coefficient with the core mode, as shown in Fig. 4.22(a) the N_t tubes composing the cladding are indexed by i and their centers are specified by vector $\bar{C}_i$. Therefore, by introducing a local cylindrical coordinate system (r_i, ϕ_i) is at the center of each cladding's tube, the perturbation function can be expressed as:

$$\Delta\varepsilon(\bar{r}) = \sum_{i=1}^{N_t} \Delta\tilde{\varepsilon}(\bar{r} - \bar{C}_i). \tag{4.19}$$

where the explicit expression of $\Delta\tilde{\varepsilon}$ is given by Eq. (4.5). This means that the perturbation function in the case of TTLF-PT can be analytically described as composition of multiple spatially shifted replicas of stand alone case. As a consequence, in the proximity of each cladding tube, $\Delta\varepsilon(\bar{r})$ is still periodic along the azimuthal direction ϕ_i of the local coordinate system with a period $2\pi/N$.
Due to the vectorial nature of the Eq. (4.7), its development gives rise to three similar integrals, one for each field component. By substituting Eq. (4.19) in each one of these integrals, it yields:

$$\tilde{K}^x_{co,ri} = (-1)^{\delta_{x,z}} \frac{\pi f}{2} \sum_{i=1}^{N_t} \iint_{A_i} \Delta\tilde{\varepsilon} \left(\frac{\tilde{\varepsilon^c}}{\tilde{\varepsilon}^c + \Delta\tilde{\varepsilon}\delta_{x,z}} E^{co}_x E^{ri}_x \right) r_i \, d\phi_i \, dr_i \tag{4.20}$$

where $x = \{r, \phi, z\}$, $\delta_{x,z}$ is the Kronecker index, $\tilde{\varepsilon^c}$ is the permittivity of a CTF centered in the origin, and A_i is the surface where $\Delta\tilde{\varepsilon}(\bar{r} - \bar{C}_i) \neq 0$. Since dielectric modes can be described as a composition of the modes of a stand alone tube, their field components can be expressed as:

$$E^{ri}_x(r_i, \phi_i) = R^{ri}_{x_1}(r_i)\cos(\xi\phi_i) + R^{ri}_{x_2}(r_i)\sin(\xi\phi_i), \tag{4.21}$$

which are periodic functions with period $2\pi/\xi$ along ϕ_i.
As shown in appendix A, for the stand alone tube a similar analytical description is valid also for the core modes. However, as shown in Fig. 4.23, this is not the case for TTLFs. Despite that, since $\Delta\tilde{\varepsilon}(\bar{r} - \bar{C}_i) \neq 0$ only near the cladding tubes'

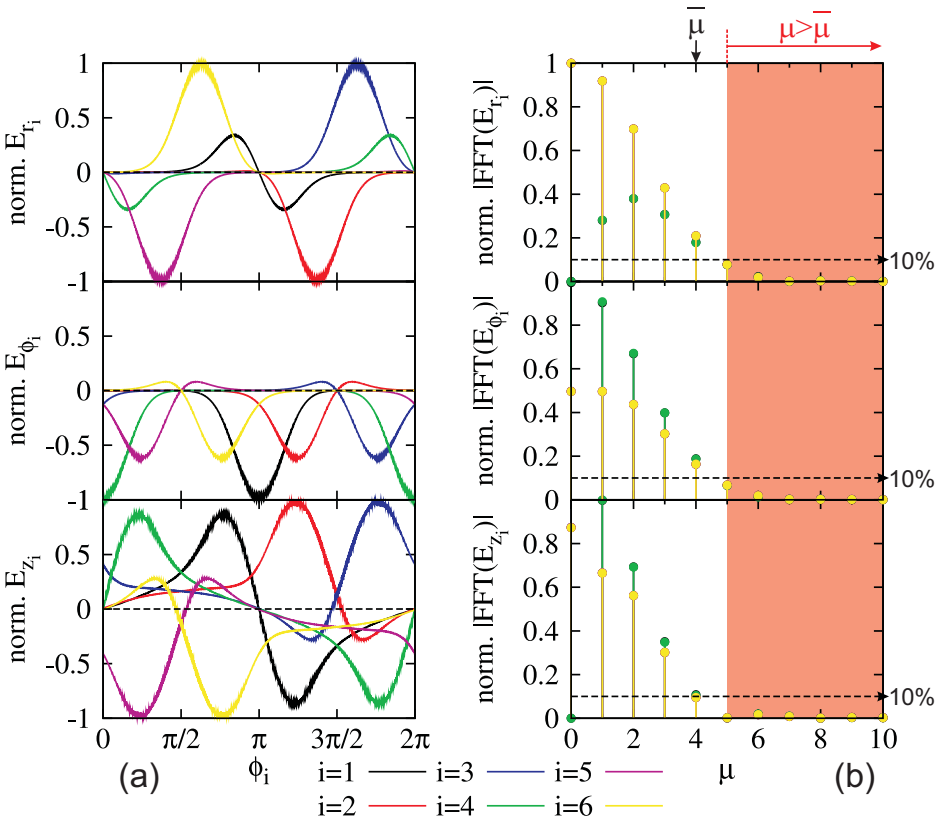

Figure 4.23: (a) Normalized electric field components of the fundamental mode along the six innermost tubes of the SC-TTLF-CT (different colors refer to different tubes). (b) Normalized fourier transform magnitude of the fields components shown in (a). Red shaded regions highlights indices for which $\mu > 4$, whereas the horizontal dashed black lines highlight a magnitude intensity 10% of the maximum value.

interfaces, E_x^{co} can be locally described by means of a Fourier-Bessel series [115]:

$$E_x^{co}(r_i, \phi_i) = \sum_{\mu=0}^{\bar{\mu}} A_{x\mu} R_{x_1}^{co,\mu}(r_i) \cos(\mu\phi_i) + B_{x\mu} R_{x_2}^{co,\mu}(r_i) \sin(\mu\phi_i), \tag{4.22}$$

where $\bar{\mu}$ is the integer at which the Fourier-Bessel series can be truncated without loss accuracy. As reported in Fig. 4.23(a), $\bar{E}^{co}$ components are slowly varying along ϕ_i with $i = \{1, .., N_t\}$. As a consequence, Fig. 4.23(b) highlights that the magnitude of their spectral components rapidly decrease when μ increases. By introducing a threshold at 10% of the maximum value, for example, all the terms with $\mu > \bar{\mu} = 4$ have a magnitude that falls below the threshold. Therefore, the series (4.22) can be reasonably truncated only to the lowest terms for which $\mu \leq \bar{\mu}$.

By introducing Eq. (4.22) into Eq. (4.20), for each tube in the cladding there are $\bar{\mu} + 1$ integrals equal to those of a PTF:

- according to Eq. (4.10), for a polygonal tube fiber with N sides, a core mode with an azimuthal index $\tilde{\mu}$ couples with cladding modes with azimuthal index such that

$$|mN - \xi| = \tilde{\mu}; \tag{4.23}$$

- in the TTLF, all the harmonics of Eq. (4.22) must be considered for the core mode, thus the condition on the dielectric modes becomes:

$$|mN - \xi| \leq \bar{\mu}. \tag{4.24}$$

This model is then applied in Fig. 4.18(c) to the SC-TTLF-PT considered before. Shaded gray regions highlights the cutoff frequencies of the $HE_{\xi,\gamma}^{di}$ and $EH_{\xi,\gamma}^{di}$ modes satisfying Eq. (4.24) with $\bar{\mu} = 3$ and $m = \{1, 2, 3\}$ (red, green and blue lines, respectively). In particular, since for each ξ value the HE mode has a lower cutoff frequency than the corresponding EH one, the vertical solid lines that delimit these resonant regions are given by:

$$HE_{mN-\bar{\mu},\gamma}^{di} \leftarrow \text{resonances region} \rightarrow EH_{mN+\bar{\mu},\gamma}^{di}. \tag{4.25}$$

An excellent agreement is found between these shaded regions and the extra losses caused by the polygonal shaped tubes in the SC-TTLF-PT.

In short, in the stand alone tube the core modes are described on the perturbation domain by only one sinusoidal function along the azimuthal direction. On the contrary, in the TTLFs, the core modes do not exhibit a periodic trend on the perturbation. However they can still be described in terms of a series of periodic functions, each of which gives a non zero term to integral (4.6). This justify the increment of the number of the resonances shown in Fig. 4.19(a).

As for the stand alone tube, it is important to point out that the model here developed does not rely on the particular perturbation, provided that it is a periodic function along the tube boundaries. As a consequence it can be also applied in case of non-polygonal deformation. Moreover, it does not rely on specific values of refraction indexes so it is valid for both SC-TLFs and HC-TLFs.

4.7.1 Conditions to have a resonance free spectral regions

As for the analysis of stand alone polygonal tubes, the resonance having the lowest frequency F_q is the most important since it determines the spectral region $F \in [0; F_q]$ without Fano resonances where the confinement loss is very close to that of an ideal TTLF-CT. According to Eq. (4.25), the first resonance is due to the $HE^{di}_{N-\bar{\mu},1}$ mode.

Cutoff frequencies of the modes of the stand alone tube are reported in Fig. 4.18(b). Figure 4.18(b) highlights that for $\xi >> 1$ the linear relation given by Eq. (4.12) between the azimuthal dependence ξ and the cutoff frequencies of dielectric modes is still valid. Therefore by combining Eq. (4.12) and (4.24) it yields:

$$F^q = \frac{N + b - \bar{\mu}}{a}, \tag{4.26}$$

thus the number of the sides N which guarantee the absence of Fano resonances in the spectral region $[0 : F_q]$ is:

$$N = \lceil aF^q - b + \bar{\mu} \rceil, \tag{4.27}$$

where $\lceil x \rceil$ denotes the nearest integer value that is bigger than x.

4.8 Numerical validation

4.8.1 Hollow core TTLF-PTs

At first the theoretical model is applied to HC-TTLFs, whose structure is shown in Fig. 4.20(a). In this case $r_{ext}^{c} = 5$ μm, $t = 500$ nm, $n_H = 1.45$ and $n_L = 1$ and a single layer of tubes surrounds the hollow core which is obtained by removing the seven innermost ones. As shown in section 4.3, tubes with these physical properties give $a = 31.8$ and $b = 8$ in Eq. (4.12). Moreover, the polygons in the cladding are oriented in such a way to contact each other only on vertices, as happens in the KFs [47, 75].

In Fig. 4.24(a) a HC-TTLF-PT with $N = 6$ is considered. It corresponds to a Kagome fiber with pitch $\Lambda = 9.5$ μm and strut thickness $t = 500$ nm. Colored rectangles on the top of the graphs represent the cutoff regions of the rings modes that satisfy Eq. (4.24) with $\bar{\mu} = 3$. Different colors correspond to different values of the m parameter. Confinement loss is compared to that of a HC-TTLF-CT. CLs coincide only in the high loss spectral regions corresponding to resonances with low azimuthal dependence dielectric modes. In the low loss regions, the Fano resonances due to hexagonal shape of the tubes composing the cladding cause a significant worsening of the confinement loss with respect to the circular case. Since $F^q = 0.24$ and the bands of $m = \{1, 2, 3\}$ are partially overlapped and the Fano resonances cover the whole spectrum.

Figure 4.24(b) shows the case of an HC-TTLF-PT with $N = 12$. Moving from $N = 6$ to $N = 12$ shifts the extra resonance bands toward higher frequencies. However $F^q = 0.53$ is still too low and the bands are still partially overlapped, so there is no significant improvement with respect to the previous case. By further increasing the sides up to $N = 24$ (Fig. 4.24(c)) an improvement of the confinement loss is obtained in both the first and the second transmission windows. Indeed, being $F^q = 0.91$, in the first transmission window there is a wide frequency range where confinement loss coincides with that of HC-TTLF-CT. Moreover, the bands with $m = 1$ and with $m = 2$ are no longer overlapped in the second transmission window creating a frequency range where confinement

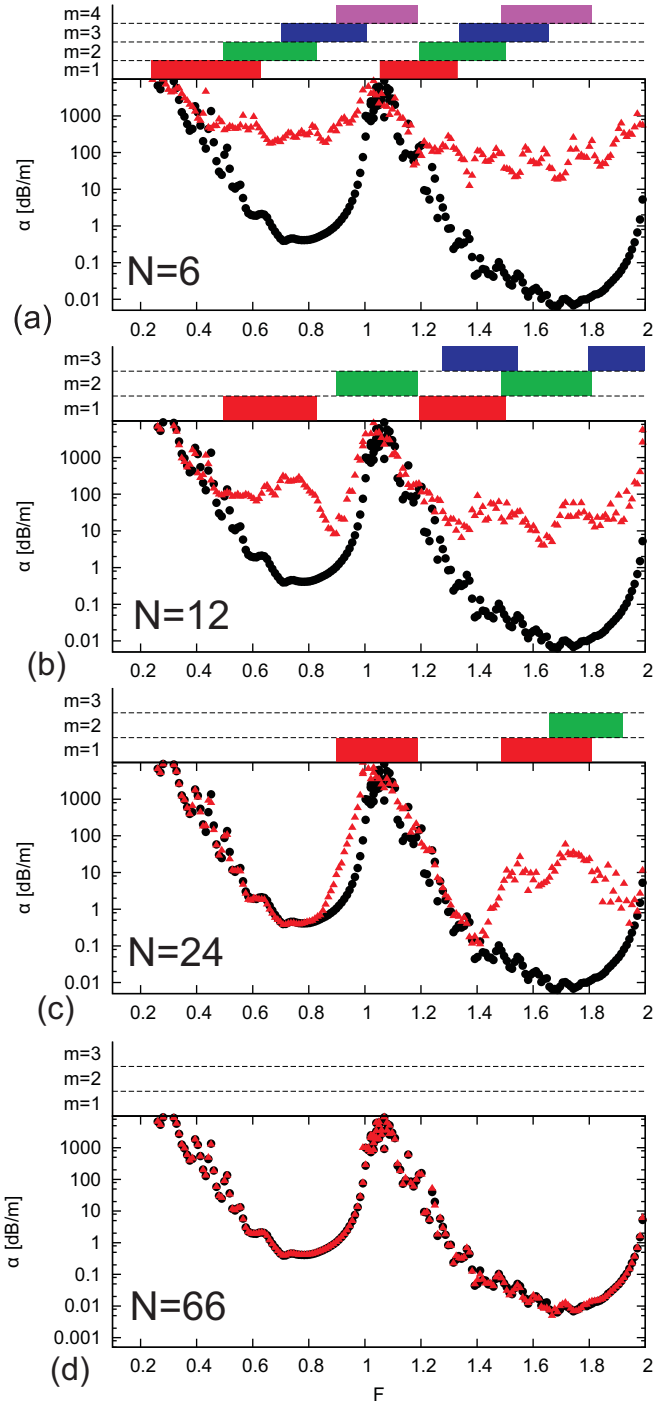

Figure 4.24: Comparison of the confinement loss performances between a HC-TLF with circular cladding tubes (black dots) and an N-sided polygonal HC-TLF (red triangles), with $N = 6$ (a), $N = 12$ (b), $N = 24$ (c), $N = 66$ (d). Rectangles on the top of the graphs represent the cutoff regions for the rings modes that satisfy Eq. (4.24) with $\bar{\mu} = 3$. Different colors are used for different values of the m parameter. In (a) only $m \leq 4$ has been considered for clearness.

loss coincides with the circular case. However, for higher frequencies, there are still a lot of resonant modes that worsen the performance of the fiber.

In order to widen the Fano resonance free region, polygons with a higher number of sides must be considered. By choosing $F^q = 2$ in Eq. (4.27) , it yields $N \geq 62$. Actually $N = 66$ is required in order to satisfy geometrical constraints about the contact points of the cladding polygons. Figure 4.24(d) shows the confinement loss performance for such fiber. As expected, the confinement loss performance of the 66-sided HC-TTLF-PT overlaps with HC-TTLF-CT's one in the first two transmission windows.

The results shown in this section are in perfect agreement with the experimental ones shown in [47] and the numerical ones given in chapter 3: in general, ICFs whose cladding is based on circular tubes give much better performances with respect to the polygonal ones because their spectrum is completely free of extra Fano resonances.

4.8.2 Solid core TTLF-PTs

In order to further confirm the general validity of the proposed model, the CL performance of a real SC-TTLF is here investigated. For the ideal case a SC-TTLF-CT is as a reference being $n_H = 1.47288$, $n_L = 1.457$, $t = 540$ nm and $r^c_{ext} = 5.4$ μm [87]. However, as shown in the scanning electron micrograph reported in [87], due to the manufacturing process, cladding tubes are actually hexagonal tubes with rounded corners instead of circular ones. In section 4.4 it was shown that rounded corners do not affect the spectral position of the Fano resonances, but reduce their bandwidth.

In order to consider a realistic model for the real SC-TTLF-PT shown in [87], a smoothing parameter $s = 0.75$ (as defined by Eq. (4.14)), was considered in the numerical simulations for the cladding's hexagons. Figure 4.25(a) compares the confinement loss performance of the SC-TTLF-PT with rounded hexagons with those of a SC-TTLF-CT. Yellow regions represent the spectral regions with high transmission loss obtained experimentally in [87]. For the SC-TTLF-CT, the resonance intensities with $LP^{ri}_{\xi,1}$ quickly decrease as ξ increases and the fiber

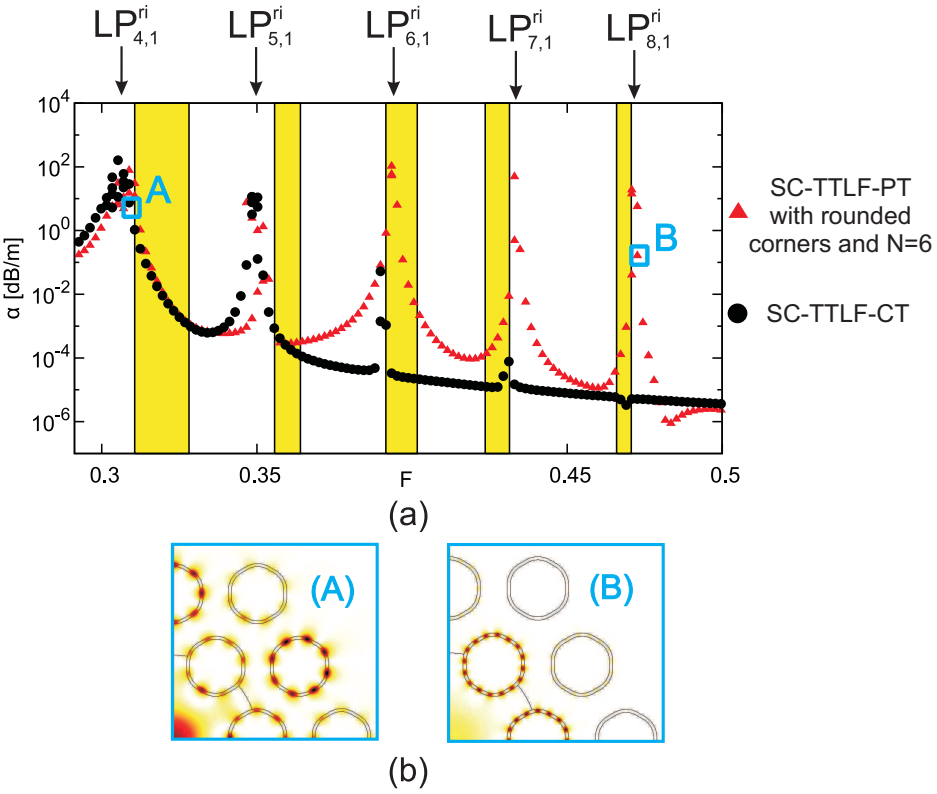

Figure 4.25: (a) Comparison of the confinement loss between a SC-TTLF with circular (black dots) or rounded hexagonal (red triangles) tubes in the cladding. Resonant rings modes are highlighted on the top of the figure. Yellow regions represent the high confinement loss regions reported in [87]. (b) Hybridization between core mode and ring modes $LP^{ri}_{4,1}$ (A) and $LP^{ri}_{8,1}$ (B) computed at $F = 0.305$ and $F = 0.47$, respectively.

does not exhibit high loss peaks for $F > 0.40$. On the contrary, the SC-TTLF-PT exhibits all high loss peaks experimentally observed, proving that they are due to the hexagonal shape of the cladding elements. This is further confirmed by Fig. 4.25(b) which shows the numerical intensities of the guided core mode found at $F = 0.305$ and $F = 0.47$. They agree very well with near field images reported in [87].

Discrepancies between numerical and experimental results are due to the fact that it was not possible to perfectly reproduce all the features of the real fiber inside the numerical solver. For example, in the simulations the tubes' thickness was considered constant, whereas in the fabricated fiber the cross section of each tube is actually a ring of closely-spaced rods spaced by around 0.6 μm. However the image resolution used in the paper does not allow to determine exactly their shape and size. A better agreement between numerical and experimental results can be obtained only by a higher resolution scanning micrograph image of the fiber's cross section.

Chapter 5

Perturbations and scaling effects in CTLF-TFs

In the previous chapters it was shown that hollow core fibers whose cladding is based on a lattice of circular tubes are very promising for low loss broadband waveguiding in the THz spectral range. The purpose of this chapter is to further investigate the spectral properties of these fibers by considering perturbations of the ideal structure, such as:

- elliptical core shape,
- thickness variations in cladding tubes,
- geometric scaling,
- bending loss.

Elliptical shape of the core can be both undesired, due for example to manufacturing imperfections, or desired, in order to have polarization maintaining fibers. At first, performance of CTLF-CTs whose cladding tubes placed on an ellipse instead of a circle are investigated. The effects of this perturbation are evaluated by considering birefringence (B), polarization dependent loss (PDL) and differential group delay (DGD) for various core ellipticities. It is shown that all these parameters change with frequency, reaching the minimum value at the center of

the transmission windows. In particular the birefringence goes always to zero at the center of each TW irrespective of the ellipticity. Numerical results show that CTLF-CTs are very insensitive to core deformation, which means that they are not suitable to obtain polarization maintaining fibers.

In chapter 2 it was shown that the thickness of the cladding tubes is essential in defining the spectral position of high loss regions and, thus, the transmission bandwidth. Then in chapters 3 and 4 it was shown how the shape of these cladding tubes affects the performance of the guided core mode. Therefore, the second goal of this chapter is to investigate the effects of a variation in the cladding tubes' thickness on the performance of the fiber. This is a very interesting aspect from the manufacturing point of view since these cladding tubes can be obtained from different drawing steps before their assemblage into the TTLF or CTLF claddings. Results show that, in general, a variation of the dielectric thickness in the cladding is highly undesirable, since the spectral width of high loss regions is expanded, thus reducing the transmission bandwidth.

The confinement mechanism shown in chapter 2 for TTLF and CTLF is absolutely general and is valid for any desired frequency range provided that a scaling of the whole fiber's structure is performed accordingly. The analysis of the propagation loss with respect to the core size and the working frequency has already been performed for other kind of hollow core waveguides such as:

- hollow core in an infinite dielectric medium [54],
- stand alone tube fiber [109],
- hollow core Bragg fibers [100],
- kagome fibers [46].

Therefore, a further goal of this chapter is to extend this scaling analysis of the propagation loss also to the CTLF-CTs introduced in the previous chapters.

Finally also the bending loss properties of CTLF-CTs are investigated. Since most of the THz applications applications require flexible waveguides to allow dynamic setup configurations, it is extremely important to define general design rules for the minimization of undesired bending effects due to the bending.

Through a thorough numerical analysis it is shown that, due to the bending, the confinement mechanism is affected in two different ways:

- reduction of the transmission bandwidth,
- confinement loss peaks due to extra couplings between the core and the hole modes.

A complete theoretical model is finally proposed in order to quantify the effects for both of these phenomena.

5.1 Core ellipticity in CTLFs

The cross sections of both the ideal and the perturbed CTLF-CTs are shown in Figs. 5.1(a) and (b), respectively. In the ideal case the cladding is composed by a circular arrangement of eight hollow dielectric tubes with thickness $t = 145$ μm and internal radius $r_{int} = 1.3$ mm, corresponding to a core radius $R_{co} = 2.1$ mm. In the elliptical case (ETLF-CT), the same cladding tubes have the same parameters, but here they are displaced in such a way that their centers are on an ellipse instead of a circle. As a consequence, core radius changes along the azimuthal direction, moving from its minimum value R_m, along the horizontal direction, to its maximum R_M, along the vertical one. The ratio between the two radii defines the ellipticity of the core

$$\tau = \frac{R_M}{R_m}. \tag{5.1}$$

Figure 5.1(c) shows the normalized values of R_M/R_{co} and R_m/R_{co} versus the ellipticity.

In both cases the cladding tubes are embedded into an external jacket in order to enhance the mechanical stability of the structure. Since the goal of the current chapter is to focus on the variations of the confinement mechanism in case of ellipticity, the external jacket is supposed to be of infinite extent for simplicity. Moreover both the cladding tubes and the jacket are assumed to be composed of Teflon whose refractive index at 1 THz has been experimentally measured as $n_H = 1.44 - j1.2 \cdot 10^{-3}$ [15,95] and, throughout this section, is assumed frequency

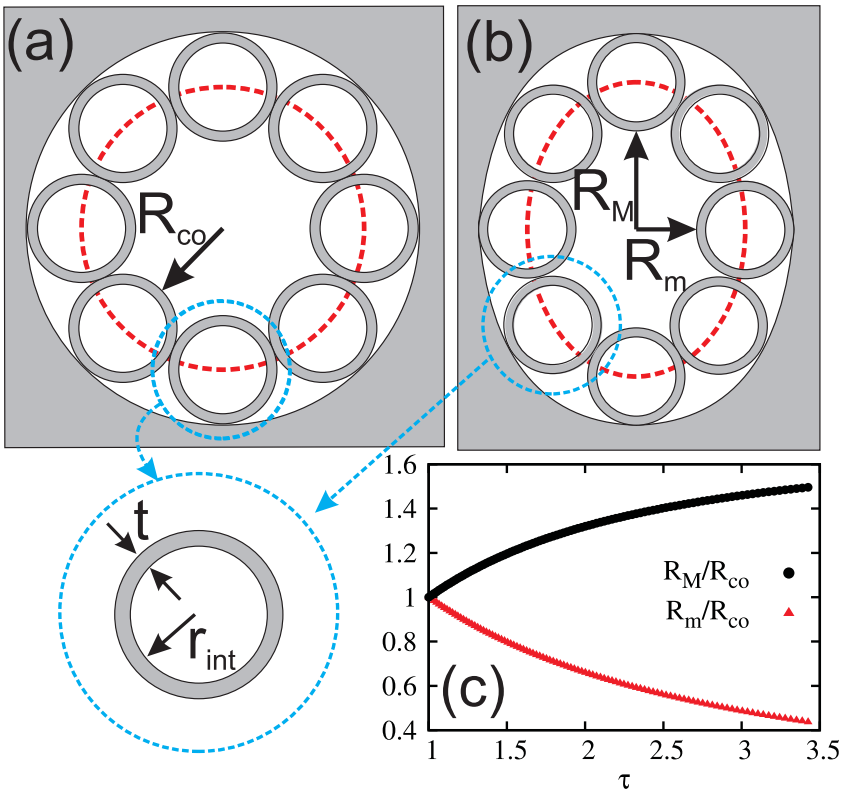

Figure 5.1: Cross sections of a circular (a) and a elliptical (b) tube lattice fiber. The tube parameters are: $r_{int} = 1.3$ mm, $t = 145$ μm and $n = 1.44$. (c) R_M/R_{co} and R_m/R_{co} versus the ellipticity τ.

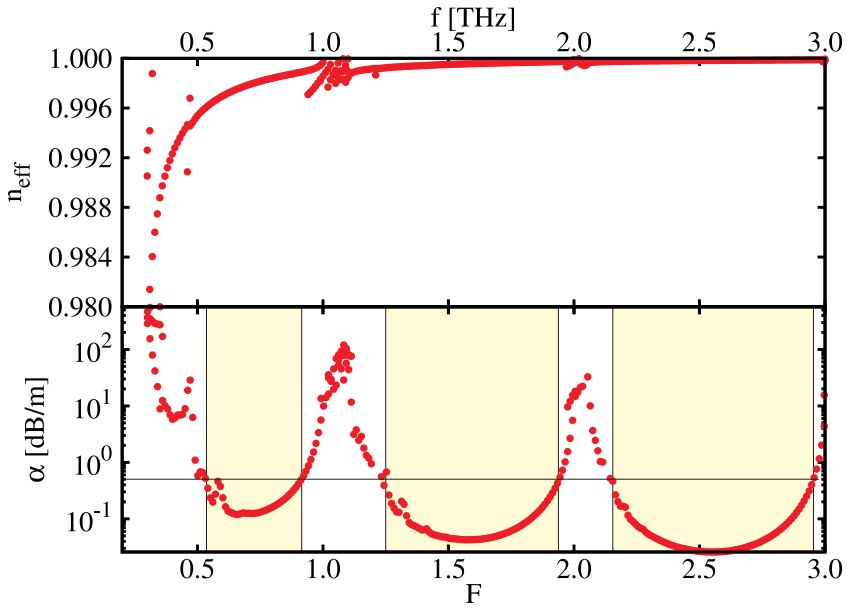

Figure 5.2: Dispersion curve (top) and CL (bottom) of the fundamental mode HE_{11} of the circular TLF.

independent for simplicity.

In chapter 2, it was shown that for these ICFs the electromagnetic radiation is confined inside the hollow core through the inhibited coupling mechanism. Dispersion and CL of the fundamental mode HE_{11} for the CTLF-CT are shown in Fig. 5.2 versus the absolute frequency f and the normalized frequency. CL spectrum is strongly frequency dependent. Transmission windows (low CL regions) are separated in frequency by high CL peaks caused by the coupling between the core mode and some low azimuthal order cladding modes which occur for integer values of the normalized frequency F. Hereinafter, light yellow regions in the figures will show the frequency ranges where confinement loss is lower than 0.5 dB/m.

As shown in chapter 2, the confinement mechanism shown for the CTLF-CT holds also for the ETLF-CT since it does not depend on the particular arrangement for the cladding tubes. However, in ETLF-CTs the ellipticity of the core breaks the degeneracy between the two orthogonal polarizations of the core mode, thus causing birefringence and different confinement loss values. Hereinafter subscripts or

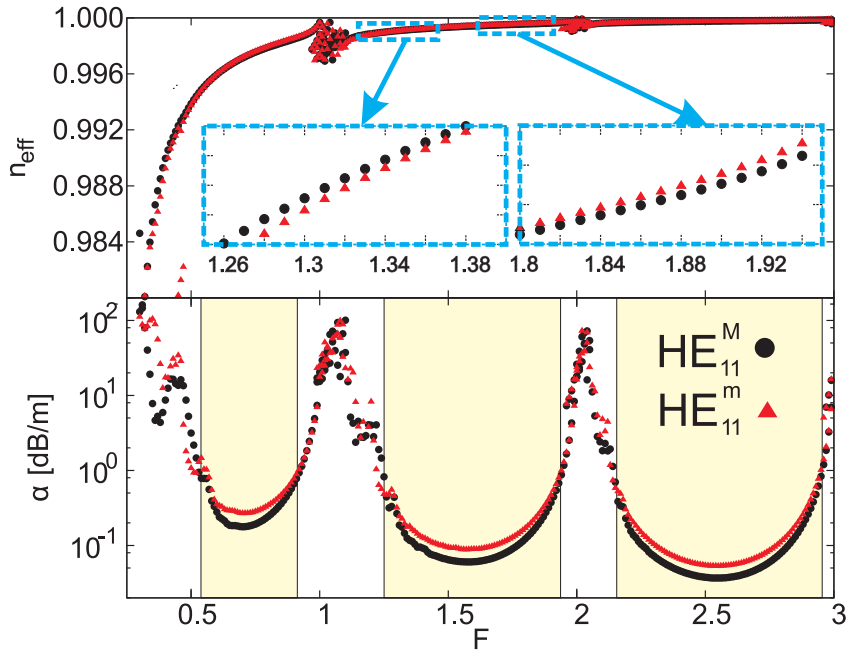

Figure 5.3: Dispersion curves (top) and CL (bottom) of the two polarizations HE_{11}^M and HE_{11}^m of the fundamental mode of an elliptical TLF with $\tau = 1.95$.

superscripts m and M will be used to address the parameters referring to these two polarizations of the fundamental core mode, HE_{11}^m and HE_{11}^M, whose electric field is polarized along the minor and the major axis, respectively.

The effective indices n_{eff}^m and n_{eff}^M and the attenuation constants α_m and α_M are shown in Fig. 5.3 for an elliptical fiber with $\tau = 1.95$. As expected, the spectra of α_m and α_M split up with $\alpha_m > \alpha_M$ and both of them higher than the in the CTLF-CT. Also the dispersion curves split up, but in a more complicated way. As shown in the inset of Fig. 5.3, in the first half of the TWs, $n_{eff}^M > n_{eff}^m$, whereas on the other half the order reverses. This means that in each TW there always is a frequency where the dispersion curves cross each other. To the author's knowledge this property has never been observed in other birefringent fibers even with electromagnetic field confinement based on other mechanisms such as photonic band gap [116] or total internal reflection [117].

Figure 5.4 shows the profiles of the z component of the Poynting vector along the x and y axis at the center of the first three TWs, i. e. $F = \{0.6, 1.6, 2.6\}$.

Negligible differences are found between the profiles of the HE_{11}^{M} and HE_{11}^{m} modes, thus justifying the small differences in dispersion and propagation loss shown on Fig. 5.3.

5.1.1 Birefringence

The birefringence $B = n_{eff}^{m} - n_{eff}^{M}$ for different ellipticity in the range $\tau \in [1; 1.95]$ is shown in Fig. 5.5. By moving from the beginning to the end of all TWs, birefringence changes in sign. Maximum absolute values are located close to the edges of the TWs whereas the minima ones are found close to the center of the TWs, where birefringence always goes to zero irrespective of τ. The highest absolute magnitudes are found in the first TW, and they rapidly decrease moving to the higher TWs. In fact, as the normalized frequency increases, the ratio R_{co}/λ increases too, making elliptical perturbation effects more and more negligible. However, even with small R_{co}/λ ratios and high τ, the birefringence is always lower than $7 \cdot 10^{-5}$. Figure 5.6 shows the beat length $L_b = \lambda/B$. In each TW there is a spectral range where L_b is longer than some tens of meters, which means that the dephasing of the two polarization at the fiber's output is negligible if propagation length of meters are considered, as usually is in the THz applications.

5.1.2 Differential Group Delay

Thanks to their broadband characteristic, CTLF-CTs are particularly interesting for pulsed applications such as time domain spectroscopy [118]. Due to the different dispersion values, the pulses traveling on the two polarizations have different group velocity v_g and thus arrive at the receiver with different delays. If the input polarization is not under control, this can cause an unwanted signal distortion. Fig. 5.7 compares the differential group delay ($DGD = 1/v_g^m - 1/v_g^M$) for various ETLF-CTs with different values of ellipticity. DGD measures the difference in traveling time per unit length between the two polarizations. Similarly to the birefringence, also DGD has a strong frequency dependence: maximum values are found close to the edges of the TWs, whereas minimum

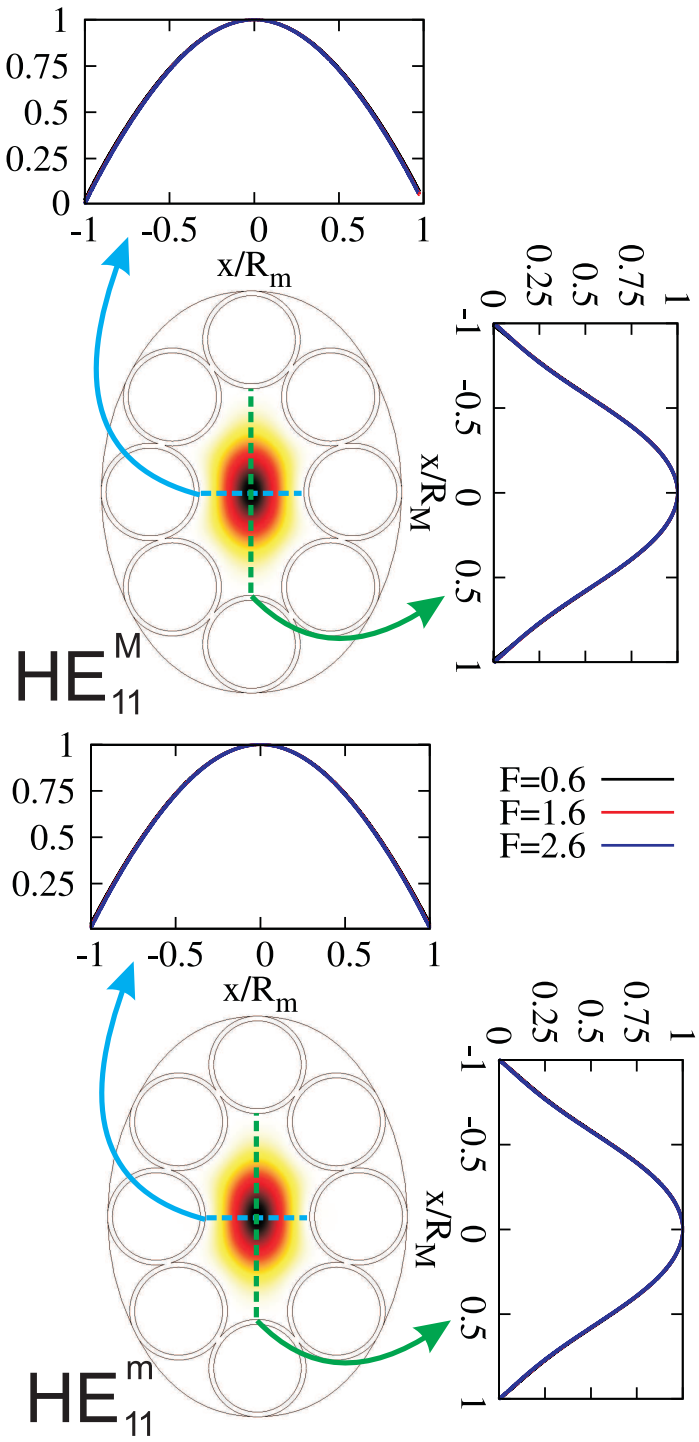

Figure 5.4: Profiles of the z component of the Poynting vector along the x and y axis for three normalized frequencies $F = \{0.6, 1.6, 2.6\}$. Left and right pictures refer to HE_{11}^{M} and HE_{11}^{m} respectively.

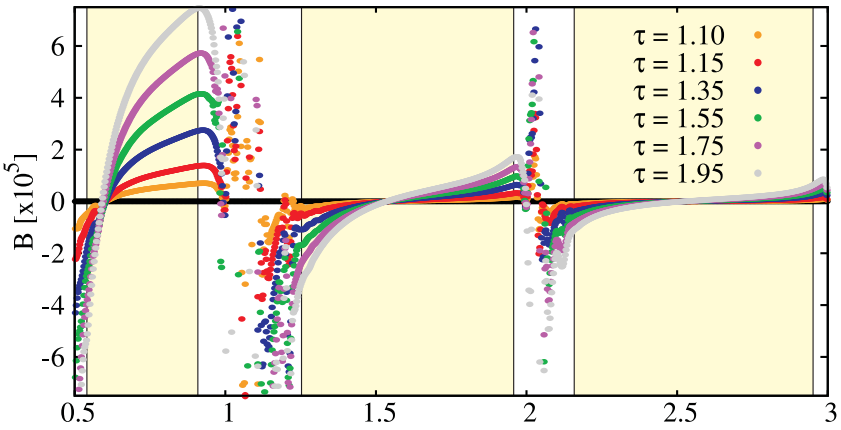

Figure 5.5: Birefringence for various ETLF-CTs.

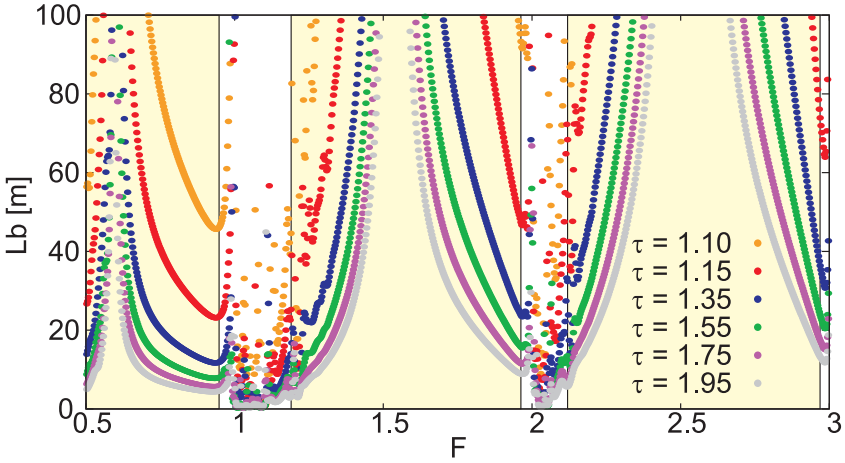

Figure 5.6: Beat length for various elliptical ETLF-CTs.

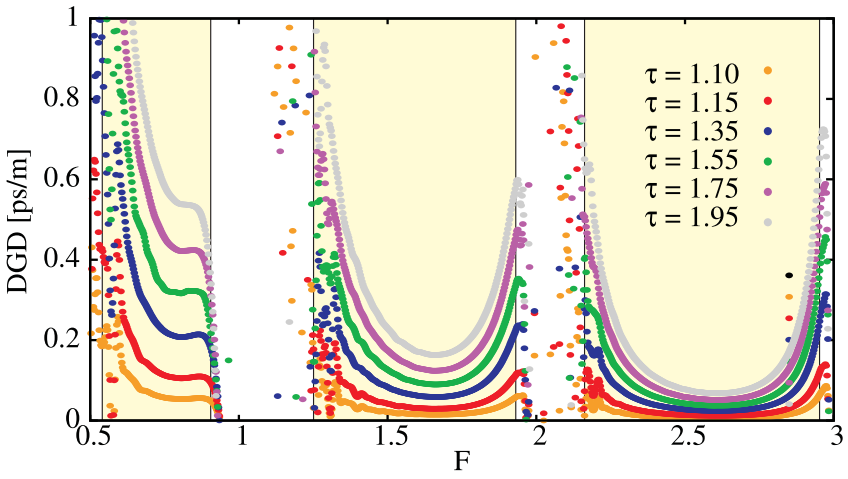

Figure 5.7: DGD for various ETLF-CTs.

ones are found at the center. Even in this case, moving from low to high TWs, DGD reduces rapidly. Hence the first TW gives the maximum DGD, while in the successive ones there are wide spectral ranges where DGD remains below 100 fs/m if $\tau \leq 1.35$. This shows that CTLF-CTs are very robust against undesired echoes that may be caused by unwanted ellipticity due to fabrication process.

5.1.3 Polarization Dependent Loss

Figure 5.8 compares the polarization dependent loss $PDL = \alpha_{dB}^{m} - \alpha_{dB}^{M}$ for various ETLF-CTs with different values of ellipticity. PDL is an important parameter for this kind of fibers, especially when ellipticity is an undesired feature. It can be used to estimate the additional loss of one polarization with respect to the other one. Once again, minima and maxima values are found at the center and at the borders of the TWs, respectively. For $\tau \leq 1.95$, PDL is lower than 0.1 dB/m, which means that even with propagation length of meters, the power difference between the two polarizations is lower than 1 dB.

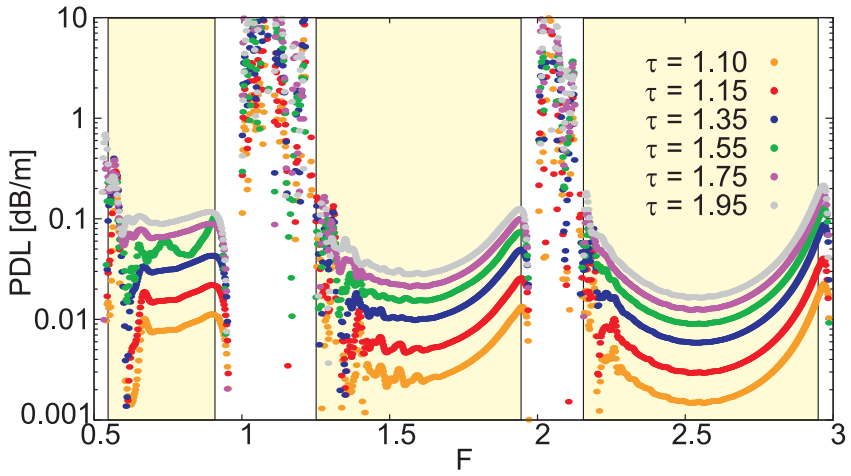

Figure 5.8: PDL for various ETLF-CTs.

5.2 TLFs with thickness perturbations

In chapter 2 it was shown that the thickness t of the cladding tubes is essential in defining the spectral position of high loss regions and, thus, the transmission bandwidth. The analysis presented in this section starts from the original CTLF-CT structure labeled A in Fig. 5.9(a). In this structure $t = 131$ μm, $r_{ext} = 873$ μm, $R_{co} = 1.405$ mm and $n = 1.52$ which is a typical value for Zeonex at 1 THz [16]. The first perturbed structure considered is labeled B in Fig. 5.9(a): the two cladding tubes that are centered on the x axis have a thickness $t' \neq t$, whereas the other ones are unperturbed. According to Eq. (2.1), this different thickness of cladding tubes sets extra high loss regions at:

$$f' = \frac{cm}{2t'\sqrt{n^2-1}}, \qquad m \in \mathbb{N}. \tag{5.2}$$

By normalizing the resonant frequencies given by Eq.(5.2) with the original t value, it is possible to express the resonant normalized frequencies as:

$$F' = m\frac{t}{t'}, \qquad m \in \mathbb{N}, \tag{5.3}$$

which suggests the way according to which the vertical lines of Fig. 5.9(b) have been computed.

As shown in Fig. 5.9(b), as soon as t' is reduced with respect to its original value

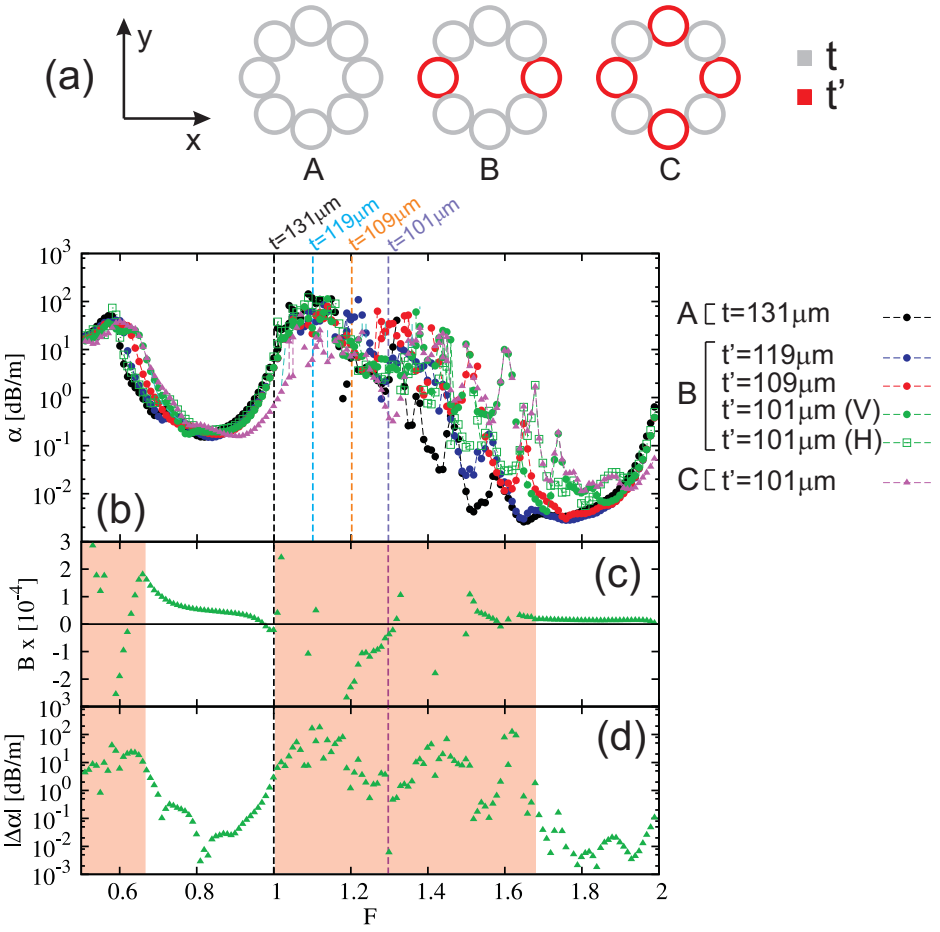

Figure 5.9: (a) Original (leftmost) and perturbed (center and rightmost) versions of the CTLF-CTs analyzed in which some of the cladding tubes have a different thickness t'. (b) Performance of the fibers shown in (a) with different values of the perturbed thickness t'. Vertical lines represent the additional high loss regions caused by the tubes with $t' \neq t$ calculated according to Eq. 5.3. (V) represents the FM in which the electric field on the transverse plane is directed on the y axis, whereas (H) is its orthogonal counterpart. (c,d) Birefringence ($B = n_{eff}^H - n_{eff}^V$) and differential loss ($\Delta\alpha = \alpha^H - \alpha^V$) for the two the two polarization of the FM in the B structure with $t' = 101$ μm. Red shaded regions highlight high CL frequencies due to resonances with the dielectric modes.

t, both of the first two considered transmission windows reduce their bandwidth. In particular, as suggested by the vertical lines reported on the graph, this is due to an increase in the spectral width of high loss regions.

For the case $t' = 101$ μm, both of the polarizations of the FM were also investigated in order to find any difference in performance connected to the different relative orientation of the electromagnetic field lines and the boundaries. However, as shown in Figs. 5.9(c) and (d), only negligible differences for both birefringence and differential loss were found for the first two transmission windows. It should be noticed that, differently from the ETLFs, in these kind of perturbed CTLFs birefringence does not change in sign inside the transmission window. However, its magnitude is still very small ($|B| < 10^{-4}$ for both transmission windows), which means that they can not be exploited to obtain polarization maintaining fibers due to the very limited difference in performance between the two polarizations of the FM.

As a final step, the structure labeled C in Fig. 5.9(a) was also considered for a single value of $t' = 101$ μm for sake of clearness. As shown from the performance in Fig. 5.9(b), when four perturbed tubes are introduced into the ideal structure the high loss peaks at $F = 1$ and $F = 2$ are slightly shifted toward high frequencies. However, especially in the second transmission window, this gain is negligible with respect to the increased extension of high loss regions, which cause an overall reduction of the transmission bandwidth.

5.3 CL scaling relations with R_{co} and f

The analysis of the waveguiding mechanism that has been proposed in the previous chapters is absolutely general and does not rely on a particular frequency range. This suggests that both the TTLFs and the CTLFs that have been proposed in this thesis can be extended also to other applications. Kagome fibers, for example, have already been proposed for the infrared spectral region for the delivery of high power pulses [119] and pulse compression [120], for the ultra violet spectral region [74] and also for the THz one [17].

The analysis of the change in propagation loss for the HE_{11} core mode corresponding to a variation in the core size or working frequency is a classic problem in the literature and it has already been addressed for various hollow core waveguides:

- for a simple air hole immersed in an infinite dielectric medium [54]

$$CL \propto \frac{1}{R_{co}^3 f^2}; \tag{5.4}$$

- for an hollow core Bragg fiber whose cladding is made by B layers of concentric dielectric tubes [109]:

$$CL \propto \frac{1}{R_{co}^{2B+2} f^{2B+1}}, \tag{5.5}$$

  which for $B = 1$ represents the stand alone dielectric tube fiber considered in the previous chapters, thus giving

$$CL \propto \frac{1}{R_{co}^4 f^3}; \tag{5.6}$$

Recently, numerical analysis have been performed also for kagome fibers, even though different results were reported:

- [46]:

$$CL \propto \left(\frac{1}{R_{co} f}\right)^3. \tag{5.7}$$

- [75]:

$$CL \propto \frac{1}{R_{co}^3 f^2}. \tag{5.8}$$

Following these results, it is reasonable to assume that also in CTLFs the confinement might be expressed as:

$$CL \propto \frac{1}{R_{co}^p f^q}, \qquad p, q \in \mathbb{N}^+ \tag{5.9}$$

where both p and q are generic coefficients that must be determined. Without loss of generality, it is possible to assume that $p \geq q$, thus rewriting Eq. (5.9) as:

$$CL \propto \left(\frac{1}{R_{co} f}\right)^q \left(\frac{1}{R_{co}}\right)^{p-q}. \tag{5.10}$$

In the two following sections, different transformations will be considered in order to numerically determine both p and q coefficients for CTLFs.

5.3.1 Scaling effects on the confinement loss

A possible solution to determine the difference $p - q$ in Eq. (5.10) is to consider the scaling transformation schematically represented in Fig. 5.10. The initial CTLF-CT structure is shown on the left side of Fig. 5.10(a). For this fiber $t = 131$ μm, $R_{co} = 1.405$ mm, $n = 1.52$ (typical value for Zeonex at 1 THz [16]) and an external dielectric jacket are considered. The analysis is performed by scaling both the entire fiber's structure and the working frequency through a generic parameter $M \in \mathbb{R}^+$ as:

$$\begin{aligned} \lambda' = \lambda \cdot M, \quad \rightarrow \quad f' = f/M \\ R'_{co} = R_{co} \cdot M, \\ t' = t \cdot M, \\ r'_{ext} = r_{ext} \cdot M, \end{aligned} \tag{5.11}$$

while keeping the total number of mesh elements constant among various steps in order to preserve the same accuracy in the simulations.

The analysis of the confinement mechanism given in the previous chapters showed that the spectral properties of the guided core are completely determined by the coupling between the core and dielectric modes of the CTLF-CT. When the normalized frequency given by Eq. (2.1) is taken into account, the latter are not affected by the scaling proposed in Eq. (5.11) provided that the $\rho = r_{int}/r_{ext} = 1 - t/r_{ext}$ value is kept constant (which is always true since $t'/r'_{ext} = t/r_{ext}$). Also core modes are not affected by the changed given by Eq. (5.11) since the Marcatili's approximation (see Eq. (2.2)) remains unchanged when $R_{co}f$ is kept constant (which is also true since $R'_{co}f' = R_{co}f$).

Since the transformation (5.11) keeps $(R_{co}f)$ constant, according to Eq. (5.10), also $CL \cdot R_{co}^{p-q}$ is constant, i.e.

$$CL'(R'_{co})^{p-q} = CL(R_{co})^{p-q} \rightarrow \log\left(\frac{CL'}{CL}\right) = (q-p)\log\left(\frac{R'_{co}}{R_{co}}\right). \tag{5.12}$$

Figure 5.10(b) shows the analysis of the normalized confinement loss (CL'/CL) for the fundamental core mode of the CTLF-CT versus the scaling parameter $M = R'_{co}/R_{co}$ for two different normalized frequencies $F = \{0.8; 1.8\}$. Interpola-

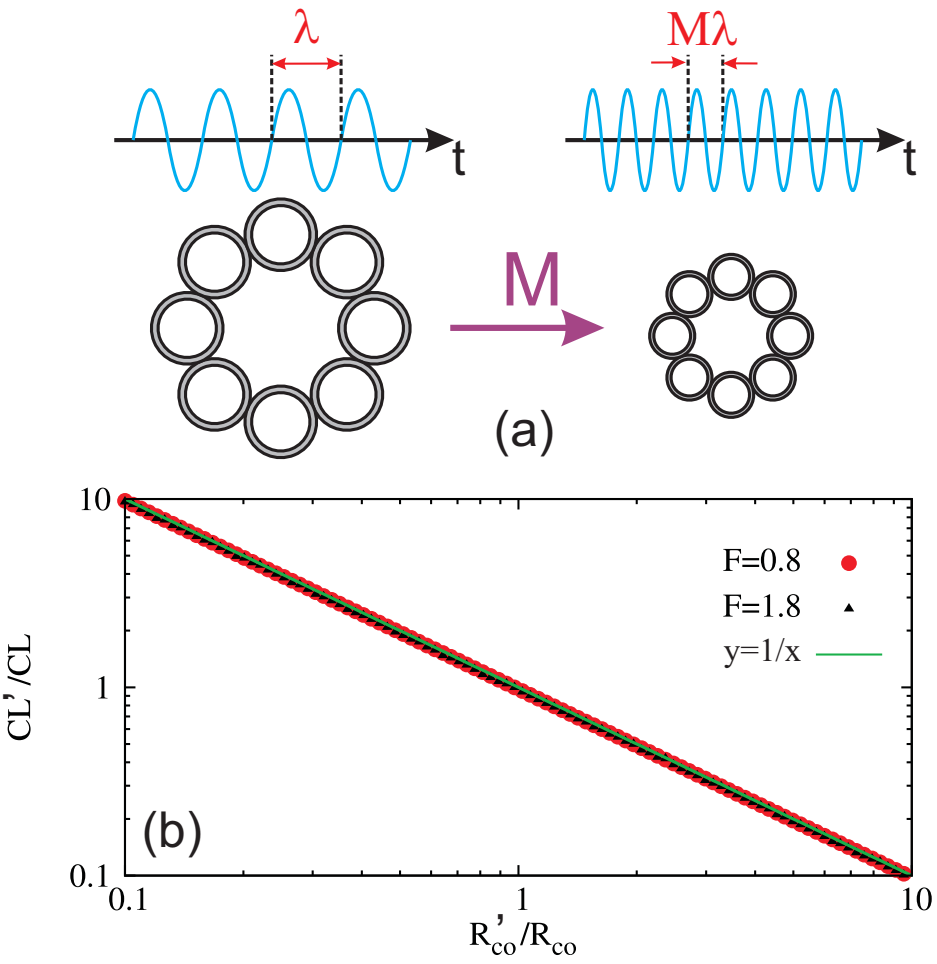

Figure 5.10: (a) Schematic representation of the considered transformation. (b) Confinement loss plotted versus the scaling factor M for two normalized frequencies $F = \{0.8; 1.8\}$. The blue and green solid lines are used to approximate numerical data and to highlight that $CL \propto 1/M$.

tion lines have also been reported in order to highlight that:

$$\log\left(\frac{CL'}{CL}\right) = -1\log\left(\frac{R'_{co}}{R_{co}}\right), \tag{5.13}$$

which means

$$q - p = -1 \qquad \rightarrow \qquad p = q + 1. \tag{5.14}$$

Therefore, according to Eq. (5.9), the confinement loss in CTLF-CT scale as:

$$CL \propto \left(\frac{1}{R_{co}f}\right)^{q}\left(\frac{1}{R_{co}}\right). \tag{5.15}$$

in which only q is not yet determined. A physical interpretation of this relation is given in appendix C.

5.3.2 CL variations with different core radii

A possible solution to find the generic q coefficient in Eq. (5.15), is to consider the tranformation shown in Fig. 5.11(a). The physical and geometrical properties of the cladding tubes are still the same as before, but in this case the number of the tubes N in the cladding is changed, thus giving a core radius which depends on N as:

$$R_{co}(N) = r_{ext}\left[\frac{1}{\sin\left(\frac{\pi}{N}\right)} - 1\right]. \tag{5.16}$$

Since all the properties of the single tubes in the cladding are kept constant, this solution allows to consider variations in the core size without affecting the spectral distributions of dielectric modes as shown in chapter 2. As a consequence the absolute frequency values considered in simulations are the same for all the fibers.

Figure 5.11(b) shows the CL performance of the proposed CTLF-CT when $N \in [6; 12]$. As expected the spectral positions of high loss regions are not affected by a change in the number of sides, highlighting that the confinement mechanism is not perturbed in the various cases. Moreover, for each CTLF-CT the propagation loss reduces by moving from lower to higher transmission windows, whereas the minimum values reached in the middle of each transmission region reduces when N is increased due to the increased core size.

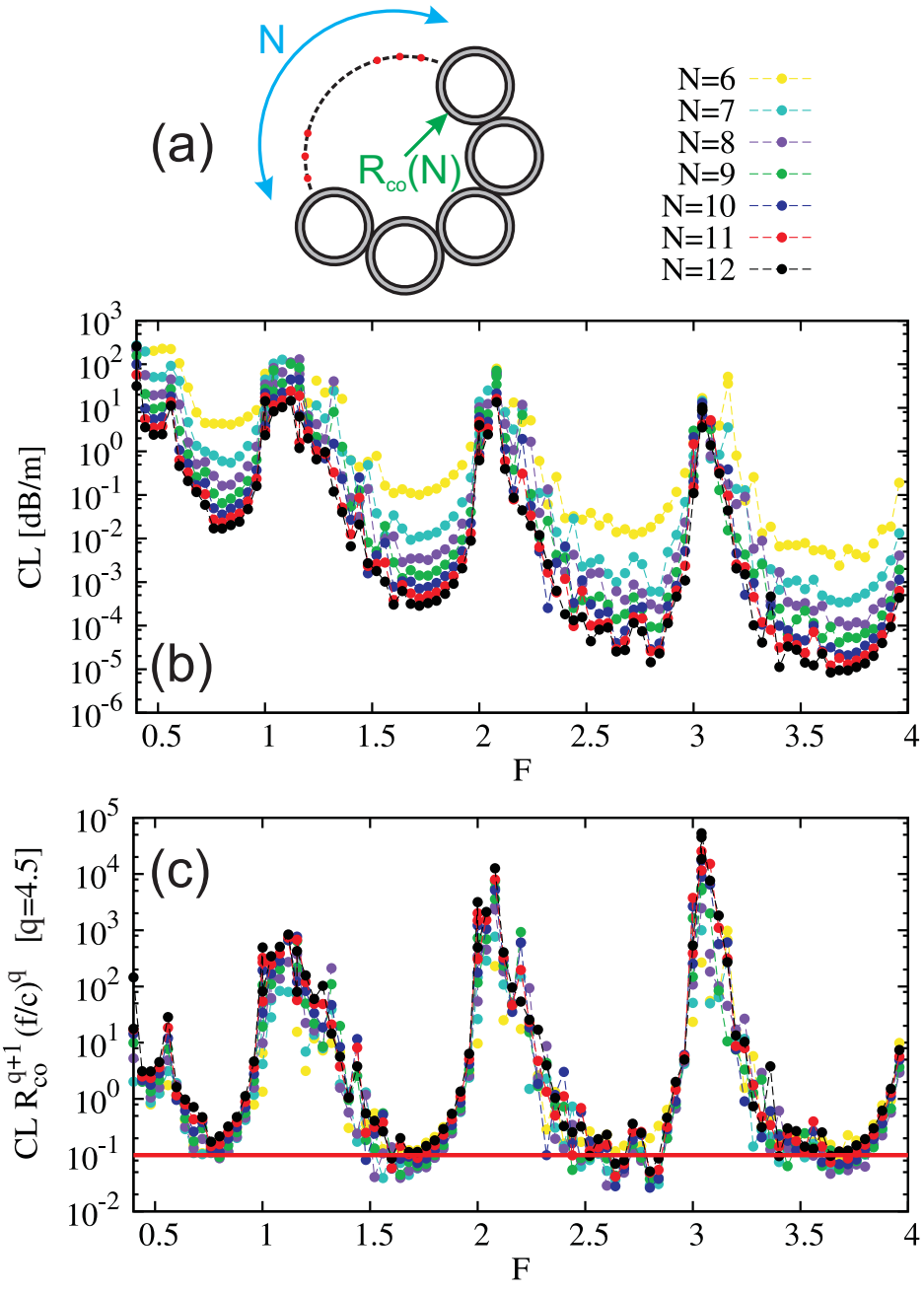

Figure 5.11: (a) Generic CTLF-CT structure with an arbitrary number N of tubes in the cladding. (b) CL of the structures shown in (a) for the first four transmission windows. The same curves are shown also in (c) after the multiplication with the normalizing factor $R_{co}^{5.5} \cdot f^{4.5}$.

According to Eq. (5.15):

$$CL_{N=6}[R_{co}(N=6)]^{q+1}f^q \approx \ldots \approx CL_{N=12}[R_{co}(N=12)]^{q+1}f^q, \qquad (5.17)$$

which means that, though a proper normalization, the CL curves with different N values should be almost overlapping over the whole spectrum. In order to numerically estimate the correct value for the q coefficient in Eq. (5.15), the confinement loss curves shown in Fig. 5.11(b) were re-plotted several times with the normalization given in Eq. (5.17) and by using different q values. The best agreement with Eq. (5.17) was found for $q = 4.5$ and the final result is shown in Fig. 5.11(c). As expected the CL curves of all the considered CTLFs are almost overlapping over the all the first four transmission windows. This confirms that the CL reduction among different fibers due to the different number of tubes used in the cladding, is correctly compensated by the normalizing factor. Moreover, an horizontal red line was also added to Fig. 5.11(c) to highlight that, after normalization, the also the CL reduction with increasing frequency is also compensated.

Together with the result of the previous section (Eq. (5.15)), this suggests that for CTLF-CTs:

$$CL \propto \left(\frac{1}{R_{co}f}\right)^{4.5} \frac{1}{R_{co}}. \qquad (5.18)$$

5.4 Analysis of the bending loss in CTLF-CTs

For the analysis of the bending loss in CTLF-CTs the structure shown in Fig. 5.12 is considered. It is a CTLF-CT with 8 cladding tubes with $t = 252$ μm and $r_{int} = 743$ μm. The dielectric material is supposed to be polymethylmethacrylate (PMMA) which, as measured experimentally in the following chapter, has a complex refractive index $n_H = \Re(n_H^{PMMA}) - j\Im(n_H^{PMMA})$ in the THz range. In order to evaluate the effects of the dielectric absorption on the bending properties of the waveguide two different cases are considered:

- real PMMA tubes, in which $\Im(n_H) = \Im(n_H^{PMMA})$,
- ideal PMMA tubes, in which $\Im(n_H) = 0$.

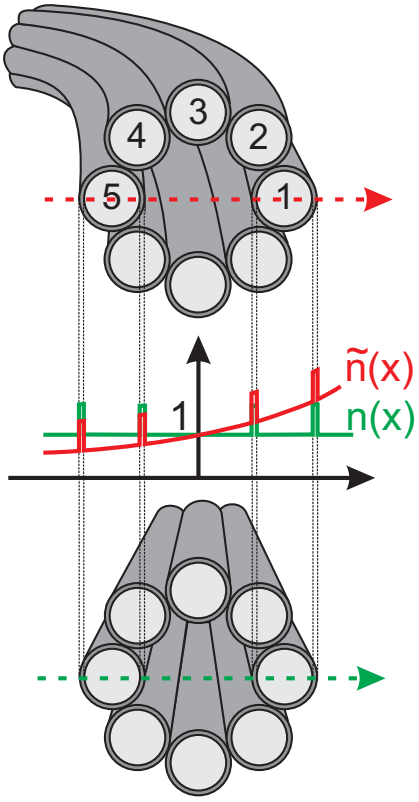

Figure 5.12: Effect of the conformal mapping on the refractive index of the fiber in the transverse direction.

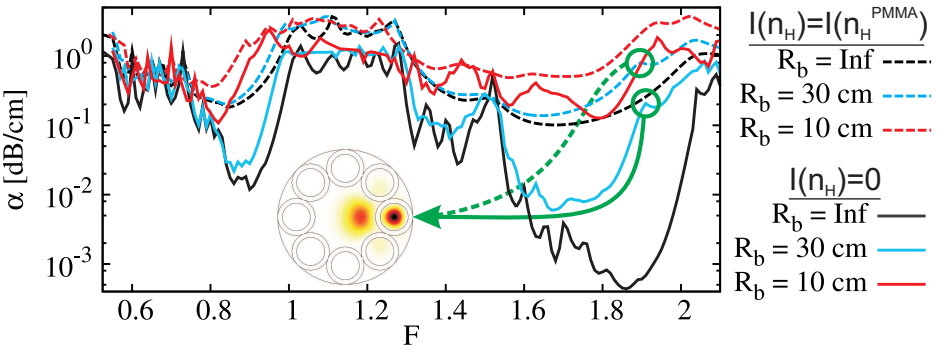

Figure 5.13: Comparison of propagation loss in case of bending for CTLF-CT with either ideal (solid lines) or absorbing (dashed lines) PMMA tubes.

The numerical analysis of the bending loss performed is based on the conformal mapping technique [121], where a bent fiber with refractive index $n(x, y)$ is analyzed in terms of a straight fiber with a refractive index:

$$\tilde{n}(x, y) = n(x, y)e^{\xi/R_b}. \tag{5.19}$$

In this expression, $\xi = \{x, y\}$ is the bending direction while R_b is the bending radius. A schematic of this effect is shown in Fig. 5.12 for bending in the xz plane, but the same can be readily applied also for a bending in the yz plane.
In order to better understand the loss mechanisms in bent CTLF-CTs and to separate the effects of the leakage and of the material absorption, the propagation loss spectra with $R_b = \{10, 30, \infty\}$ cm and either PMMA or lossless tubes were computed for the first two transmission windows and the results are shown in Fig. 5.13. As expected, the lossless case is more sensitive to bending because the loss of the straight fiber is much lower than in the absorbing case. In both cases, however, the bending causes both an increase of the losses in the middle of the transmission windows and a reduction of the transmission bandwidth. The latter is due to a down shift of the high frequency edges close to $F = 1$ and $F = 2$, whereas the lower edges are almost unperturbed. Since this shift exists in both cases, it is due to confinement mechanisms and not to material absorption. In addition to the bandwidth reduction, extra peaks are also observed inside the transmission windows as highlighted and shown in the inset of Fig. 5.13. They

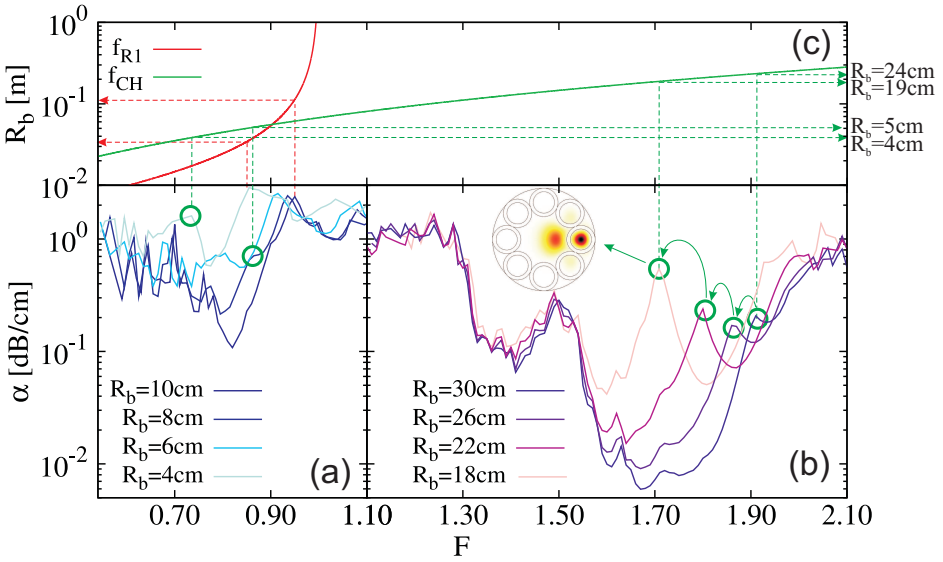

Figure 5.14: (a) Propagation loss of the core mode in the first transmission window for $R_b = \{4, 6, 8, 10\}$ cm (from light to dark blue). (b) Propagation loss of the core mode in the second transmission window for $R_b = \{18, 22, 26, 30\}$ cm (from light to dark violet). The resonance between core and hole mode is highlighted in the inset. (c) Evaluation of Eq. (5.20) for the first resonance edge (red) and of Eq. (5.24) for the resonances between core and hole modes (green) in the two transmission windows.

are due to extra resonances between the core mode and hole modes as already observed in other inhibited coupling fibers [97, 122, 123]. Their spectral position strongly depends on the bending radius. This is clearly shown in Fig. 5.14(b) where the calculated propagation loss spectrum in the second transmission window is shown for decreasing values of R_b (from 30 cm to 18 cm). When R_b falls below 30 cm, this new resonance shifts toward lower frequencies, thus compromising that transmission window. In general, bending effects are higher in the second transmission with respect to the first one, and their intensity and spectral position is strongly connected with bending radius.

These results show that bending loss in CTLF-CTs even with highly absorbing materials does not only depend on the material absorption, but also on the waveguiding mechanism. Although some results on the behavior of bent ICFs

already exist for the infrared spectral region [97, 122–124], due to their experimental or strictly numerical nature they are unable to provide a deep insight into underlying physical mechanism that affects the fibers in the case of bending. For this reasons, in the next sections a thorough numerical and theoretical analysis based on the conformal mapping technique is presented.

5.4.1 High frequency edge shift

As shown in Fig. 5.12 the bending causes an increment of the refractive index of the outer tubes (relative to the bend), and therefore a change of the dispersion characteristics of both dielectric and hole modes. The shift of the high frequency transmission window edges is due to the shift of the cutoff frequencies of the dielectric modes. By substituting Eq. (5.19) in Eq. (2.1) it is possible to estimate the new position of the edges due to the bending:

$$F'_m = m\sqrt{\frac{n_H^2 - n_L^2}{(n_H e^{\hat{x}/R_b})^2 - n_L^2}}, \qquad m \in \mathbb{N}^+ \tag{5.20}$$

where $\hat{x}$ represents the coordinate of the outermost part of the tube on the right side of the structure in Fig. 5.12

$$\hat{x} = R_{co} + 2(r_{int} + t). \tag{5.21}$$

When the fiber is bent, $R_b < \infty$, thus

$$e^{\hat{x}/R_b} > 1 \qquad \rightarrow \qquad F'_m < m, \tag{5.22}$$

which highlights the down shift of the high loss frequency peaks. The bending radius required to shift the high frequency edge of the first transmission window to a particular frequency as calculated by Eq. (5.20) is shown in Fig. 5.14(c) (red curve).

Figures 5.14(a) and (c) allow a comparison of the numerical results with those predicted by Eq. (5.20) for the high frequency edge of the first transmission window. Excellent agreement is found. For large bending radii, the shift is negligible, as indicated by the increasing, steep gradient above $F = 0.9$. By reducing R_b the edge shifts quicker, limiting the transmission window bandwidths.

5.4.2 Extra loss due to hole modes resonances

The extra loss due to the resonances between the core mode and hole modes appear when the modes are phase matched. As shown in chapter 2, in a straight fiber this cannot happen because of the different size between the fiber core and the cladding holes. However, Fig. 5.12 shows that due to the conformal mapping on the bent fiber, the refractive indices inside the cladding holes change according to their relative position along the bending direction and the bending radius. In particular, the effective indices of the modes of the outer tubes increase approaching the effective index of the core mode until the phase matching condition is reached, causing the extra losses.

In appendix B it is shown that in case of an hollow core waveguide with a generic refraction index n_L for the core, the Marcatili's approximation given by Eq. (2.2) changes to:

$$n_{eff} = n_L - \frac{1}{2}\left(\frac{u_{\nu\mu}c}{2\pi f R\sqrt{n_L}}\right)^2. \tag{5.23}$$

By assuming a uniform refractive index inside each hole for simplicity, and by substituting the values $\tilde{n}_L(x_{ci}, y_{ci})$ in Eq. (5.23), it is possible to analytically describe the effective index of the holes modes of the i-th tube centered at (x_i, y_i) for the bent fiber. In Fig. 5.15(a) the analytical curves of the effective indices of the core and hole modes at $F = 1.806$ are shown as a function of the bending radius. They are compared with the numerical curves obtained by applying the conformal mapping technique to a single hole with internal radius r_{int}, refractive index $n_L = 1$, centered at (x_{ci}, y_{ci}) and immersed in an infinite dielectric medium with refractive index $\Re(n_H) = \Re(n_H^{PMMA})$ and $\Im(n_H) = 0$. A good agreement is found showing the validity of the proposed analytical model. Small discrepancies appear only for the hole mode placed on the y axis (hole 3 in Fig. 5.12) because for tight bends, the hole mode field profile shifts toward the outer part of the bending plane whereas the analytical model neglects this distortion. The same observations can be made for the effective index of the core mode. The difference between analytical and numerical results appears for larger bending radii for the core mode compared to hole 3 mode because having $R_{co} > r_{int}$ the field profile bending distortion is more pronounced for the core mode than the hole mode,

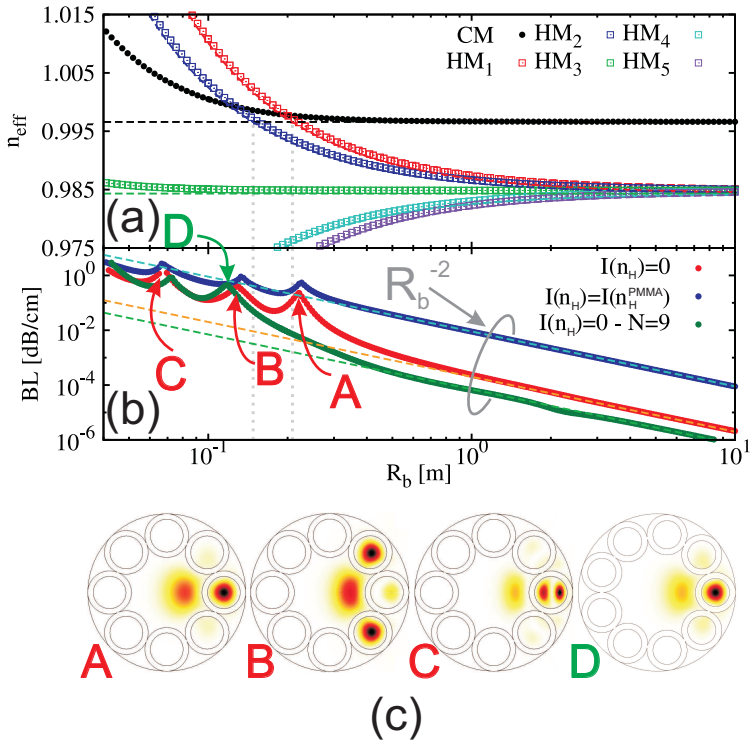

Figure 5.15: (a) Numerical (dots) and analytical (dashed lines) effective indices for the hole modes and the core mode of the CTLF. (b) Bending loss for CTLFs with 8 (red dots) and 9 (green dots) transparent cladding tubes and for a 8 PMMA tubes CTLF (blue) at $F = 1.806$. Dashed lines represent the asymptotic R_b^{-2} trend. (c) Poynting vector intensities for the core mode at the high loss peaks reported in (b).

as shown in Figs. 5.15(c). The crossing points between the core mode and hole mode curves in Fig. 5.15(a) represent the phase matching conditions, that is the resonances between core and holes modes. By equating Eq. (5.23) for both the core and the mode of a hole positioned at $x = x_c$ it is possible to have an analytical estimation of the bending radii at which these resonances appear:

$$R_b(F) = \frac{x_c}{\ln\left[\frac{M(F,R_{co})}{2} + \sqrt{\left(\frac{M(F,R_{co})}{2}\right)^2 - M(F,r_{int}) + 1}\right]}, \tag{5.24}$$

$$M(F,R) = 1 - \frac{1}{2}\left(\frac{u_{nm}t\sqrt{n_H^2 - n_L^2}}{\pi F R}\right)^2. \tag{5.25}$$

The resonance with the outermost hole mode defines the tolerance of the CTLF-CT to additional high loss peaks. The green curve in Fig. 5.14(c) shows the evaluation of Eq. (5.24) with $x_c = x_{c1}$ over the first two transmission windows, whereby the bending radius required to shift the resonance between the core and the mode of hole 1 to a particular frequency is plotted as a function of frequency. No resonances are found in the first two transmission windows for $R_b > 30$ cm meaning that the considered CTLF is relatively robust against extra resonances for such bending radii. However, when R_b falls below this, the resonance appears in the second transmission window and shifts toward lower frequencies, eventually reaching the first transmission window at $R_b \approx 5$ cm.

Bending loss, defined as

$$BL(R_b) = \alpha(R_b) - \alpha(\infty), \tag{5.26}$$

were also numerically computed at $F = 1.806$ and they are shown in Fig. 5.15(b) versus the bending radius. For large bending radii BL increases as $1/R_b^2$ as it has already been reported in the literature for other hollow core waveguides [54,100,125]. For small value of R_b, many additional loss peaks appear due to the resonances with hole modes. The intensity profile of the core mode at these peaks is shown in Fig. 5.15(c). The R_b values of the extra losses are well predicted by Eq. (5.24). Figure 5.15(b) shows also the bending loss for the core mode of a CTLF-CT with PMMA cladding tubes. For large R_b values the bending loss still scales as R_b^{-2} as was found for the lossless case. The higher magnitude of bending

loss with respect to the ideal case can be ascribed to the additional loss caused by PMMA absorption in the bent fiber. Extra losses due to the resonances between the core and hole modes are still present and their position is not changed with respect to the ideal tubes. However, their relative magnitude with respect to the background bending loss is reduced because the loss is already higher due to material absorption.

In order to further confirm the proposed model, Fig. 5.15(b) shows also the bending loss for a CTLF-CT of an alternative design with nine tubes in the cladding. In this case, R_{co} and t remain the same as before, and r_{int} is reduced to 596 μm, with a schematic shown in the lower right panel of Fig. 5.15(c). According to Eq. (5.23), this change causes a reduction of the effective index for the hole modes in the straight fiber, whereas the core mode is unaffected. As a consequence a smaller bending radius is necessary to reach the phase matching condition between core and hole modes. Numerical results shown in Fig. 5.15(b) confirm that the first resonance shifts toward lower values of bending radius, and allows the bending radius to be further reduced by 10 cm before such resonances appear. This provides an avenue for increasing the amount of bending possible before such resonances affect the transmission.

Chapter 6

Manufacturing and characterization of a CTLF

In the previous chapters a thorough theoretical and numerical analysis of hollow core waveguides whose cladding is based on a lattice of tubes was provided. Owing to the inhibited coupling confinement mechanism and to the hollow core, they offer an interesting solution for low loss and broadband waveguiding in the terahertz spectral range.

A kagome fiber for the THz range has recently been reported in the literature made from polymethylmethacrylate (PMMA) tubes [17], showing that ICFs can be obtained from cheap polymers with a simple stack and draw process. However, in chapters 3 and 4, it was shown that microstructured fibers with circular tubes in the cladding (CTLF-CTs or TTLF-CTs) allow a strong improvement of the performance with respect to the kagome fibers in terms of both propagation loss and transmission bandwidth.

In general, from a manufacturing point of view, CTLFs are easier to assemble with respect to TTLF thanks to their self-sustained structure. The circular displacement of cladding tubes, indeed, makes it possible to keep the tubes in place without any further drawing or gluing steps. As shown in chapter 3 these additional steps may cause undesired structure perturbations and performance

worsening.

Therefore, in this chapter a CTLF-CT for the THz spectral range is finally proposed. Cladding tubes were drawn from commercially available PMMA tubes and the structure was assembled manually in such a way as to keep the waveguide flexible. Final CTLF samples were characterized in both straight and bent configurations. In the straight configuration both dispersion and propagation loss of the fundamental core mode for the first two transmission windows were obtained. Thanks to the hollow core, the propagation loss of the fundamental core mode was strongly reduced with respect to the bulk PMMA material loss in both transmission windows. A 31 times reduction at 0.375 THz (first transmission window) and 272 times reduction at 0.828 THz (second transmission window) were obtained. Finally, thanks to the high flexibility of the manufactured fiber, CTLF's samples were characterized also for bending loss down to bend radii (R_b) of 10 cm. On one hand this experimental characterization confirmed the theoretical and numerical results shown in section 5.4. On the other hand, thanks to the low sensitivity of CTLFs to bending induced losses, it suggests the use of these waveguide in dynamic THz setups.

6.1 Manufacturing technique

Fig. 6.1(a) shows the transverse cross section of the manufactured CTLF. The cladding is composed of a collection of eight hollow dielectric tubes placed in a circle. They have refractive index n_H, internal radius r_{int} and thickness t. The core of radius R_{co} is located in the central part of this structure and is formed by air ($n_L = 1$). The CTLF presented in this paper was manufactured from PMMA tubes with 16 mm and 12 mm external and internal diameter respectively. This tube was drawn to an external diameter of 9.6 mm using a polymer fiber drawing tower. Part of it was used for the external jacket, while the remainder was drawn again in order to obtain the cladding tubes with an average thickness of $t = 252$ μm and an external diameter of about 1.99 mm ($r_{int} = 743$ μm). The final core radius was $R_{co} = 1.62$ mm. The cladding tubes were cut into pieces 10 cm and

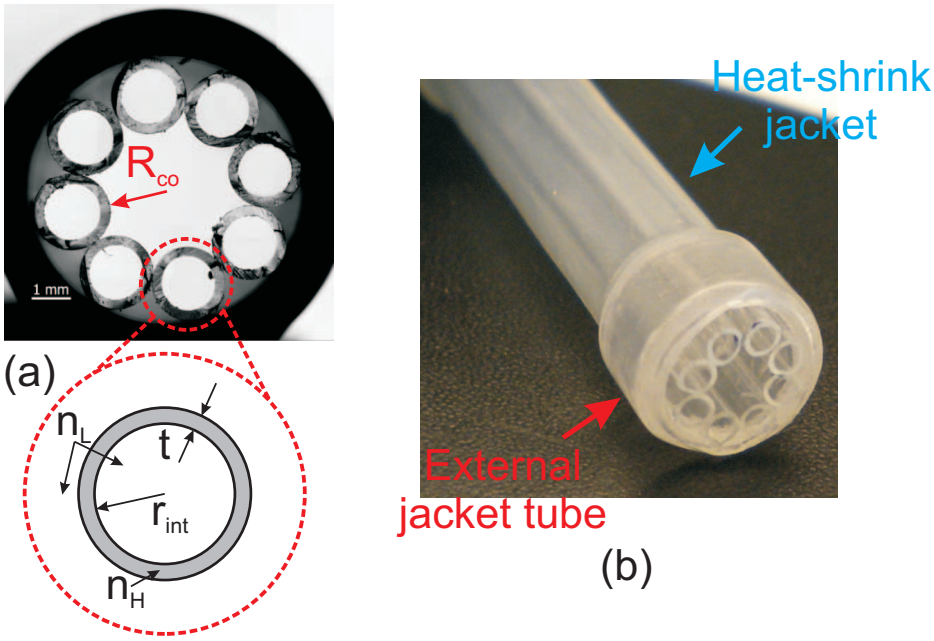

Figure 6.1: (a) Microscope image of the transverse cross section of the manufactured fiber along with its physical dimensions and dielectric properties. (b) Side picture of the fiber.

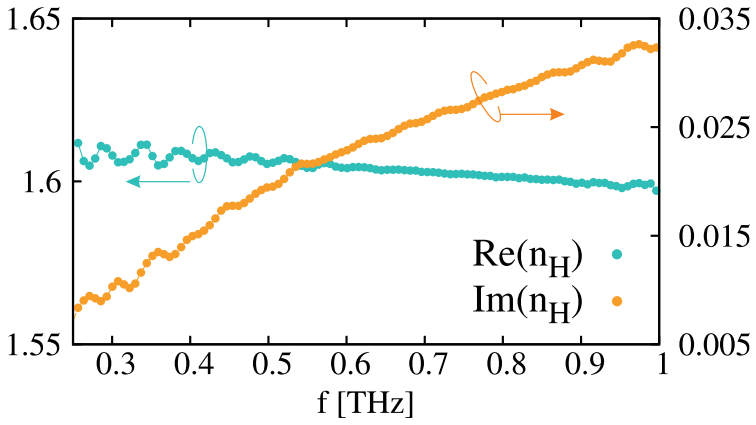

Figure 6.2: Frequency dependence of $\Re(n_H)$ and $\Im(n_H)$ measured experimentally for a PMMA disk.

20 cm long.

In order to realize a flexible THz fiber, the external jacket tube was cut into small pieces 5 mm in length. These are necessary to keep the cladding tubes in place, but at the same time they have to be separated from each other in order to make the fiber flexible. Therefore the cladding tubes were manually stacked inside these jacket rings, and the rings were spaced 10 cm apart forming a self supporting structure. No glue or fusing was necessary to keep the components in place. An external heat-shrink jacket was added over the entire structure to enhance its mechanical stability during the bending. Figure 6.1(b) gives a side picture of the fiber in order to show the final cladding shape.

In order to give a reliable comparison between the experimental results and the simulations a 2 mm thick PMMA disk was characterized via THz time domain spectroscopy. Figure 6.2 shows the measured real, $\Re(n_H^{PMMA})$, and imaginary, $\Im(n_H^{PMMA})$, of the PMMA refractive index in the range $[0.25; 1]$ THz. As expected $\Re(n_H^{PMMA})$ was almost constant in the frequency range of interest, while $\Im(n_H^{PMMA})$ changes with frequency [15].

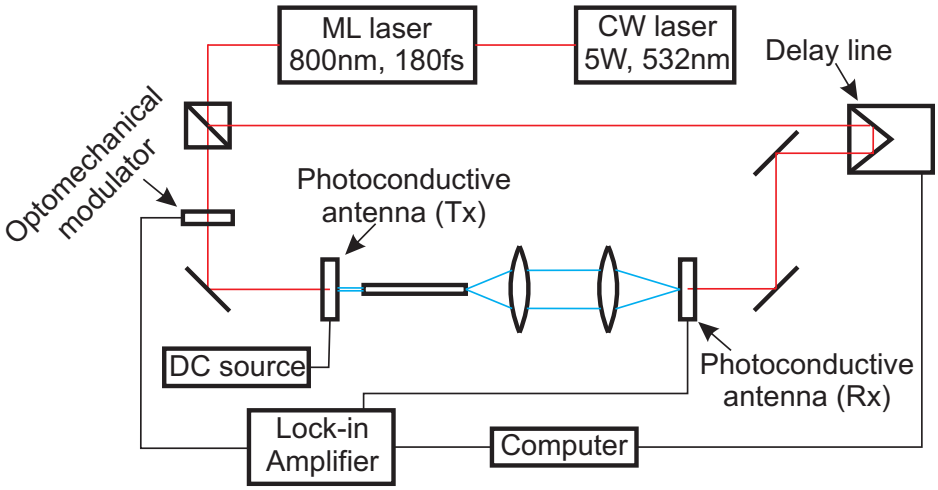

Figure 6.3: THz-TDS setup that have been used to characterize the straight fiber.

6.2 Absorption and confinement loss in CTLFs

The characterization of the fibre in a straight configuration was done using the THz time domain spectroscopy (THz-TDS) setup shown in Fig. 6.3. THz-TDS is widely used for the analysis of THz waveguides as it gives both phase and magnitude information for the detected radiation. Measurements on fibers of different length can be easily performed by moving only the first lens after the fiber's output, such that the output remains in its focal plane. In general, through the fourier transform of each temporal scan, the pulses propagating either in free space or inside the waveguides can be expresses as

$$E_0(t) \quad \longleftrightarrow \quad \tilde{E}_0(f) = E_0(f)e^{-j\phi_x}, \tag{6.1}$$

$$E_S(t) \quad \longleftrightarrow \quad \tilde{E}_S(f) = E_S(f)e^{-j\phi_S}, \qquad S = \{S', S''\}, \tag{6.2}$$

where S' refers to the 10 cm long sample, whereas S'' to the 20 cm one. Dispersion curves were computed by comparing the phase of a pulse propagating through free space to that propagating through the fiber:

$$n^S_{eff(RAW)}(f) = 1 + \frac{c}{2\pi f}\left(\frac{\phi_0 - \phi_S}{L_S}\right), \qquad S = \{S', S''\}. \tag{6.3}$$

Actually, due to the extremely low received power in the high loss spectral regions, ϕ_S might be affected by an error [16]:

$$\phi_e(f) = M(f)2\pi, \tag{6.4}$$

where $M(f)$ is a piecewise constant function which

- is constant inside each transmission window,
- vary among the various transmission windows.

However, by taking the numerical dispersion values $n_{eff}^{FEM}(f)$ given by the FEM software as a reference, it is possible to estimate the integer correction values as:

$$M(f) = \text{round}\left[\frac{fL_S}{c}\left(n_{eff(RAW)}^{S}(f) - n_{eff}^{FEM}(f)\right)\right]. \tag{6.5}$$

where round(x) approximates the real number x with its closest integer. Once Eq. (6.5) has been computed for at least one frequency in each transmission window, Eq. (6.3) can be corrected as:

$$n_{eff}^{S}(f) = 1 + \frac{c}{2\pi f}\left(\frac{\phi_0 - \phi_S + M(f)2\pi}{L_S}\right), \qquad S = \{S', S''\}. \tag{6.6}$$

In a similar way, propagation loss was computed by comparing the spectral magnitude of two fibers of different length, thus avoiding problems associated with estimating the coupling efficiency for the fibers

$$\alpha(f) = \frac{1}{L_{S''} - L_{S'}} \ln\left(\frac{E_{S'}(f)}{E_{S''}(f)}\right) \qquad \left[\frac{1}{m}\right]. \tag{6.7}$$

Great attention was paid to the positioning of the lenses and the waveguides and multiple scans were performed in order to maximize the received power over the entire spectrum and minimize any misalignment. Moreover, integration times as long as 3 s were used for the scans in order to minimize noise in the received signal.

For comparison, all the experimentally measured properties of the fibres and PMMA reported in the previous section were used to generate a model of the manufactured CTLF in a finite element software package (Comsol Multiphysics). For simplicity the jacket was approximated with a hollow pipe surrounding the

cladding tubes, with thickness $3t$ and refractive index equal to that of PMMA. Figure 6.4(a) compares the simulation and experimental results for the effective mode index (n_{eff}) and loss in the frequency range $f \in [0.25; 1]$ THz and an overall excellent agreement is found for both. Two transmission windows were observed, the fundamental (lowest frequency) one extending from 0.29 THz to 0.47 THz, and the second one extending from 0.61 THz to 0.95 THz. High loss peaks separate the different transmission windows. As shown in chapter 2, these peaks are due to the coupling between the core mode (labelled A in Fig. 6.4(b)) and the lower order dielectric modes which are confined to the high index (solid) part of the cladding tubes (labelled C in Fig. 6.4(b)). This coupling occurs when the two are resonant, as seen in Fig. 6.4(a), which occurs for frequencies satisfying [36, 48, 49, 76, 86, 123]:

$$f_{Rm} = \frac{mc}{2t\sqrt{\bar{n}_H^2 - n_L^2}}, \qquad m \in \mathbb{N}^+, \tag{6.8}$$

where c is the speed of light in vacuum and $\bar{n}_H = 1.6$ is the mean value of n_H. As shown in chapter 2, high order dielectric modes, such as D in Fig. 6.4(b), do not result in such loss peaks.

The propagation loss of the guided mode is strongly reduced with respect to the bulk materia absorption loss thanks to the hollow core [48]. Comparing the experimentally measured loss of the CTLF and the material absorption of the PMMA, a reduction of 31 times ($\alpha = 0.3$ dB/cm) at 0.375 THz and 272 times (0.16 dB/cm) at $f = 0.828$ THz were obtained, with these frequencies corresponding to the approximate centres of the two transmission windows as seen in Fig. 6.4(a). This confirms that the guided mode is confined in the hollow core of the fiber and also that hollow-core waveguides such as CTLFs are potentially low loss waveguides for the terahertz range. Materials with lower absorption such as Zeonex [16] or Topas [20] would reduce the propagation loss of the guided core mode even further.

Figure 6.4(a) shows the effect of the cladding tubes' absorption on the propagation loss of the core mode. PMMA tubes are compared with ideal lossless tubes and highly transparent ones. The latter represent a generic low loss THz material, such as Zeonex or Topas, with an imaginary part of the refractive index about

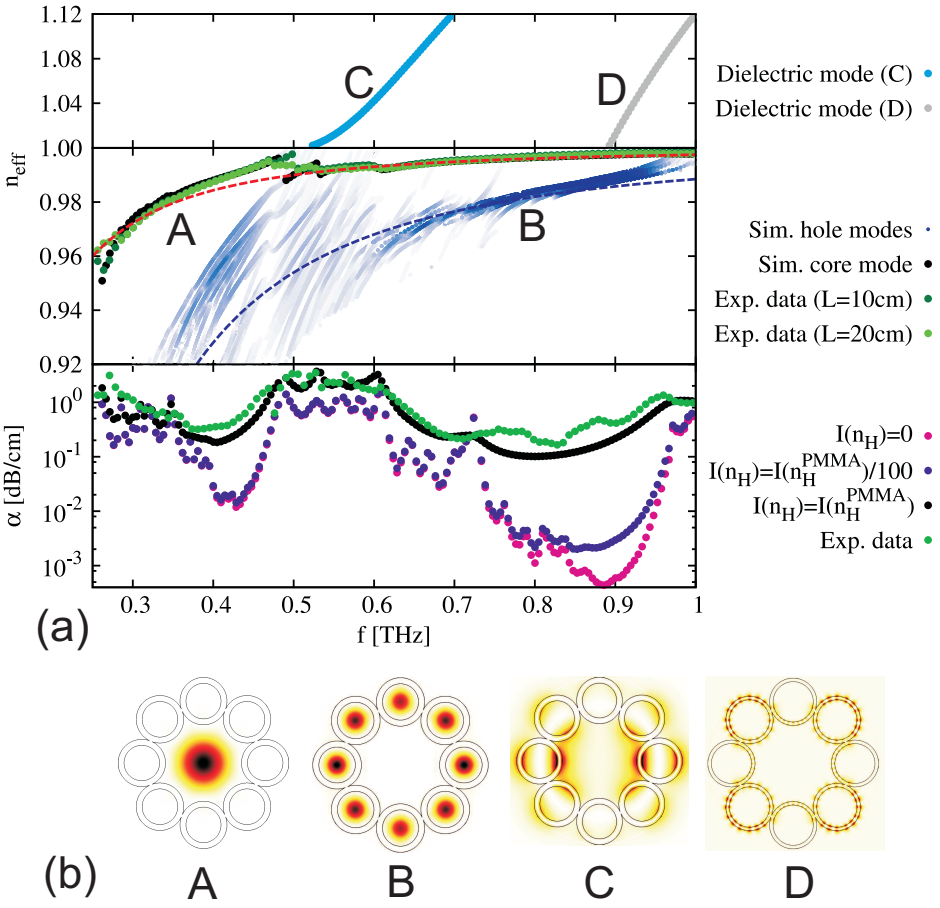

Figure 6.4: (a) Top and middle panels show the numerical dispersion curves for two dielectric modes with different periodicity along the transverse direction, the core mode and hole modes. For the hole modes the color intensity is proportional to the power inside the hole regions normalized with respect to the total power of the mode. Experimental data is also shown. Bottom panel shows numerical propagation loss for the core mode with different values of $\Im(n_H)$ and also experimentally measured loss. (b) Example images for the three different classes of modes supported by the waveguide.

a hundred times lower than PMMA [16, 20]. In the first transmission window, the difference of more than an order of magnitude between PMMA and lossless tubes shows that PMMA absorption dominates the loss. On the contrary in the case of low loss tubes, the absorption is negligible. In the second transmission window, by using low loss tubes instead of PMMA, a reduction of about two orders of magnitude is obtainable. However, the additional loss obtained from the low-loss tubes compared to the lossless tubes is no longer negligible. Overall, this analysis shows that although the absolute value of loss is higher in the first transmission window, the effects of absorption in the cladding tubes are more severe in the second transmission window. Even though these highly transparent polymers would allow a further reduction of the propagation loss, the purpose of this chapter is not to optimize transmission. The goal is to investigate the potential of CTLFs in reducing the absorption caused by the dielectric material of the cladding and their bending loss properties.

As shown in Fig. 6.4(b) and also in the previous chapters, CTLFs also support hole modes (labelled B). In chapter 2 it was shown that, in the straight fiber, they do not contribute the the confinement mechanism of the fundamental core mode. Indeed, despite both core and hole modes are guided in air, owing to the geometrical constraint $R_{co} > r_{int}$, the two are never phase matched. However, in chapter 2 it was also shown that, through a proper choice in the number of cladding tubes, hole modes can be exploited to achieve effectively single mode propagation by increasing the propagation loss of high order core modes. On the contrary, in section 5.4 it was shown that in bent CTLFs the phase matching condition with the core mode is possible. In this case extra loss peaks appear in the confinement loss spectrum of the fundamental core mode.

In order to investigate the performance of the manufactured fiber in a flexible THz setup, in the section the bending characterization of the longest sample is shown.

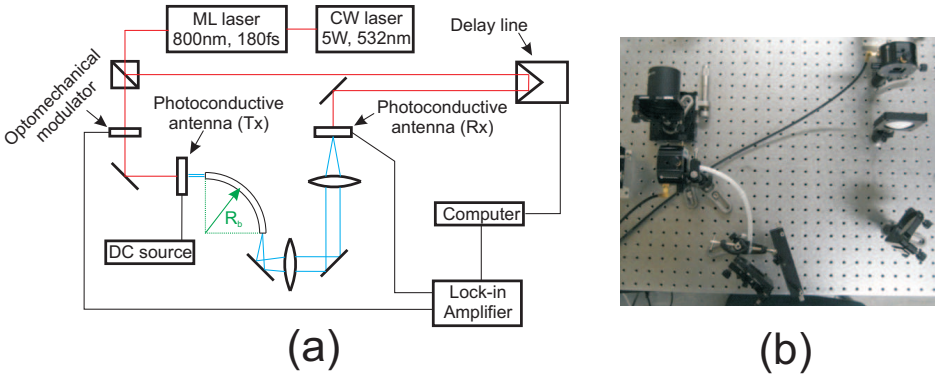

Figure 6.5: (a) THz-TDS setup that have been used to characterize the 20 cm fiber sample for the bending. (b) A picture of the setup.

6.3 Bending loss

The 20 cm long CTLF sample was used for the bend-loss characterization, and a schematic and a photograph of the experiment are shown in Figs. 6.5(a,b). The setup is basically identical to that used for the characterization of the straight fiber, however the THz path was changed to accommodate for the bent fibre. The CTLF's input remained adjacent to the transmitter antenna, but the output was shifted in order to achieve the desired bending radius R_b. Two mirrors were used to redirect the output beam to the receiver. Figure 6.5(b) shows the experimental setup in the case of a bending radius $R_b = 10$ cm, roughly corresponding to a 90° bend. Two clamps were used to hold the ends of the fibre, thus limiting the actual bendable length of the fiber to $L_B = 16$ cm.

For each bending radius R_b an experimental magnitude spectrum $E_{R_b}(f)$ was obtained, and the performance of the fiber were evaluated by considering the normalized transmission:

$$NT(f) = \frac{E_{R_b}(f)}{E_0(f)}, \tag{6.9}$$

where, as for the straight case, $E_0(f)$ represents the magnitude of the free space pulse.

Normalized transmissions for $R_b = \{10, 30, \infty\}$ cm are shown in Fig. 6.6. As expected from the numerical analysis of section 5.4, in both transmission windows the low frequency edges are substantially insensitive to bending, whereas the high

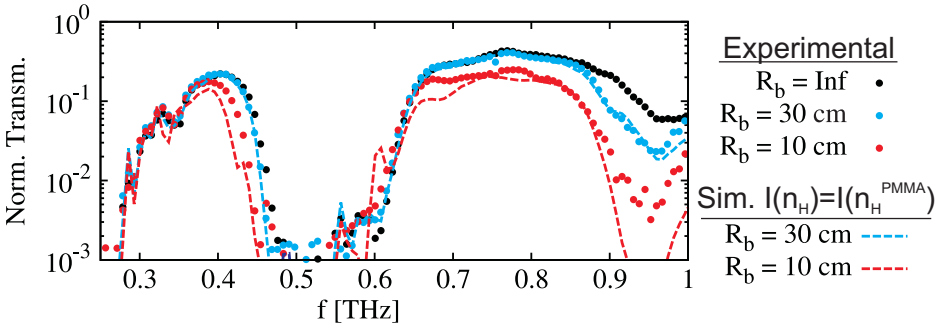

Figure 6.6: (a) Experimental and numerical normalized transmission of the 20 cm TLF sample for different bending radii. (b) Comparison of propagation loss in case of bending for CTLFs with transparent and PMMA tubes.

frequency edges shift toward lower frequencies as R_b decreases. Moreover, the first transmission window is less sensitive to the bending than the high order ones. In the first transmission window, $R_b = 10$ cm is required to observe a clear shift of the high frequency edge, whereas in the second window the shift is apparent with $R_b = 30$ cm. Apart from the high frequency edge shift at $R_b = 10$ cm, the normalized transmission in the first window is otherwise unaffected by the bending. The second window, on the contrary, is more sensitive. When $R_b = 30$ cm the normalized transmission separates from the straight case only for $f > 0.85$ THz. A reduction of the bending radius down to 10 cm causes a decrease in transmission over essentially the entire transmission window.

As for the straight case, Fig. 6.6 compares also these experimental results with the numerical ones obtained in section 5.4 for the CTLF with real PMMA cladding tubes. By considering the numerical bending losses $BL(f)$ as given by Eq. (5.26) and the experimental spectral magnitude $E_{R_b=\infty}(f)$ for the straight case, numerical normalized transmission was computed as:

$$\widetilde{NT}(f) = \frac{E_{R_b=\infty}(f)}{E_0(f)} e^{-BL(f)L_B}. \tag{6.10}$$

Excellent agreement is found between the numerical and the experimental normalized transmission curves for $R_b = 30$ cm, whereas some discrepancy appear for the $R_b = 10$ cm one. As highlighted also in Fig. 6.5(b), for such a tight bending radius the curvature of the fiber is not uniform along the whole fiber

length. This might result in the higher experimental transmission with respect to the expected one as shown in Fig. 6.6.

Unfortunately extra loss peaks due to the resonances between core and hole modes are not visible on Fig. 6.6. As explained in section 5.4, this is due to the high absorption of the PMMA tubes used for the cladding which greatly reduces the effects of these extra resonances.

In conclusion, the experimental results shown in this chapter confirm and highlight the main features of the CTLF-CT structure proposed in this thesis:

- a strong reduction of the absorption loss thanks to the hollow core;
- broadband waveguiding characteristics thanks to the inhibited coupling confinement mechanism;
- easy manual assemblage giving a compact and flexible waveguide;
- reasonably low sensitivity to the bending.

These features suggest that the proposed CTLF-CTs can be used is pulsed and dynamic THz setups, such as imaging or sensing.

Chapter 7

Conclusions

The increasing number of applications for that have been proposed for the THz range in recent years, requires for a proper flexible, broadband and low loss waveguide for the delivery of THz radiation. Classical waveguides (metal waveguides or solid core fibers), indeed, can not be used owing to the limited conductivity of metals and to the high absorption of dielectrics at THz frequencies. Therefore innovative solutions have recently been proposed in the literature. Among them, hollow core waveguides seem to be the most promising solution to overcome these limitations by confining the electromagnetic radiation in the central part of the fiber which is made of air.

Therefore this thesis concerned with the analysis of the waveguiding mechanism for a particular kind of hollow core fibers in which the cladding is composed by a lattice of dielectric tubes. These fibers belong to the general class of inhibited coupling fibers, in which the electromagnetic radiation is confined inside the core region via the inhibition of the coupling between the core and the cladding modes. An analytical description of the former is relatively easy since many solutions have already been proposed in the literature for similar hollow core fibers. No such an accurate description exists, however, for the dielectric modes.

The core idea of this thesis is to simplify the analysis of cladding modes by investigating the spectral properties of the single dielectric tubes that compose it. Since the stand alone dielectric tube is known analytically, the great improvement

of this model with respect to the previous ones is that it allows to completely predict the effects of tubes' geometrical and physical parameters on the spectral properties of the guided core mode. In detail, it allows to determine

- conditions for the existence of transmission windows,
- conditions for effectively single mode guidance,

which are extremely important for the design of an hollow core, broadband and single moded THz fiber.

This theoretical model was then extended in order to consider also perturbations of the ideal structure. At first a polygonal shape was considered for the the cladding tubes instead of the initial circular one. This allowed for a comparison also with other kind of inhibited coupling fibers (such as kagome fibers) that have recently been proposed in the literature. Once again, the analysis of the complex microstructured cladding started from that of the stand alone polygonal tube and the comparison with its circular counterpart. It was found that this polygonal shape causes many detrimental extra Fano-like resonances in the confinement loss spectrum of the guided core mode. By considering the polygonal shape as a perturbed version of the circular one a theoretical model was then proposed showing that the spectral positions of these extra resonances are actually connected to the number N of sides in the polygon. At the same time it confirmed also that circular shaped tubes are much desirable for a low loss and broadband waveguiding, thus concluding general designing and manufacturing guidelines.

Perturbation analysis was then extended to account also for other kind of non idealities, such as ellipticity of the fiber's core, bending and scaling. The former is particularly important from a manufacturing point of view, since it may be caused by a non perfect displacement of the cladding tubes around the hollow core. However, all the ellipticity induced effects (birefringence, polarization dependent loss and group velocity dispersion) are reasonably small in magnitude and, more importantly, they are minimized in the middle of the transmission windows. This confirmed that the proposed fibers are not much sensitive to elliptical perturbations.

Similarly, being flexibility one of the main features for the waveguide proposed in this thesis, bending analysis is also extremely important. Through a thorough numerical investigation, it was shown that the bending loss of CTLFs are affected by two different phenomena: a reduction of the transmission bandwidth and extra resonances with cladding hole modes. Both of them showed to depend on the bending radius R_b: for the former it affects the spectral width of the transmission window, whereas for the latter the spectral position of extra resonances. Theoretical models were finally proposed in order to quantify these relations and predict how bending changes spectral properties for the guided core mode.

All the numerical and theoretical analyses proposed in this thesis were presented in a normalized frequency F. Therefore, all the models and conclusions that were drawn are absolutely general and they were not limited to the THz spectral region. As a consequence, through a proper geometrical scaling, the same fiber's structure can be used also for other frequency ranges. However, as shown for many other hollow core waveguides in the literature, even though this transformation does not affect the confinement mechanism, it changes the propagation loss of the guided core mode. Therefore, a thorough analysis on the propagation loss dependency on both core radius R_{co} and working frequency f was finally proposed.

Finally the manufacturing and characterization of a real CTLF was proposed. Cladding tubes were obtained starting from polymethylmethacrylate (PMMA) preforms, whereas the high fiber's flexibility was preserved by the removal of most part of the rigid dielectric jacket and the substitution with an heat shrink tube. The experimental characterization for the first two transmission windows showed that, despite the extremely high absorption of PMMA at THz frequencies, the hollow core allows to greatly reduce the propagation loss. Gains are the order of 31 times (0.3 dB/cm) at 0.375 THz and 270 times (0.16 dB/cm) at 0.828 THz. Bending characterization, on the contrary, was performed for bending radii down to 10 cm. According to the theoretical analysis, main bending effects were connected to slight reductions of the transmission bandwidths, but they appeared only for tight bend radii ($R_b \approx 10$ cm). Finally, together with the

theoretical analysis proposed in this thesis, these experimental results confirm that the proposed waveguide can effectively been used as a low loss, broadband and flexible waveguide in real THz dynamic setups.

Appendix A

Fano resonances in polygonal tube fibers

The condition (4.10) such that the coupling integral (4.7) is non-zero can be obtained by expressing the electric field components as a product of two functions, each individual functions of r and ϕ [53, 110]:

$$\begin{aligned} E_x^{co}(r,\phi) &= R_{x_1}^{co}(r)\cos(\mu\phi) + R_{x_2}^{co}(r)\sin(\mu\phi); \\ E_x^{di}(r,\phi) &= R_{x_1}^{di}(r)\cos(\xi\phi) + R_{x_2}^{di}(r)\sin(\xi\phi); \end{aligned} \tag{A.1}$$

with $x = \{r, \phi, z\}$. By substituting (A.1) into (4.7), twelve addends, four for each component, are obtained. For example by considering longitudinal components the four terms are:

$$\begin{aligned} &\int_0^{2\pi} \cos(\mu\phi)\cos(\xi\phi) I_{z_{1,1}}(\phi) + \cos(\mu\phi)\sin(\xi\phi) I_{z_{1,2}}(\phi) \\ &+ \sin(\mu\phi)\cos(\xi\phi) I_{z_{2,1}}(\phi) + \sin(\mu\phi)\sin(\xi\phi) I_{z_{2,2}}(\phi) d\phi \end{aligned} \tag{A.2}$$

where

$$I_{z_{i,j}}(\phi) = \int_0^{\infty} \Delta\varepsilon(r,\phi) R_{z_i}^{co}(r) R_{z_j}^{di}(r) r dr, \tag{A.3}$$

with $i, j = 1, 2$. Replacing the expression of $\Delta\varepsilon(r, \phi)$ given by Eq. (4.3) into Eq. (A.3) it yields:

$$I_{z_{i,j}}(\phi) = \varepsilon_0(n_1^2 - n_2^2)\left\{\tilde{n}_{int}^2 \int_{\rho_p^{int}(\phi)}^{\rho_c^{int}} R_{z_i}^{co}(r) R_{z_j}^{di}(r) r\, dr - \tilde{n}_{ext}^2 \int_{\rho_p^{ext}(\phi)}^{\rho_c^{ext}} R_{z_i}^{co}(r) R_{z_j}^{di}(r) r\, dr\right\}, \quad \text{(A.4)}$$

being $\tilde{n}_{int} = (n_1/n_2)^{\text{sign}[\rho_p^{int}(\phi) - \rho_c^{int}]}$ and $\tilde{n}_{ext} = (n_1/n_2)^{\text{sign}[\rho_c^{ext} - \rho_p^{ext}(\phi)]}$. Since in (A.4) the integrand functions do not vary along the azimuthal direction, the only dependence by ϕ is given by $\rho_p^{int}(\phi)$ and $\rho_p^{ext}(\phi)$ functions which are periodic in ϕ with period of $2\pi/N$. This makes also $I_{r_{i,j}}(\phi)$ periodic with the same period and it can be expressed by means of its Fourier expansion:

$$I_{z_{i,j}}(\phi) = \sum_{m=0}^{\infty} P_{z_{i,j}}^m \sin\left(mN\phi + p_{0_{z_{i,j}}}^m\right). \quad \text{(A.5)}$$

By substituting the $m - th$ harmonic component of $I_{z_{i,j}}(\phi)$ into (A.2) it yields:

$$\begin{aligned}
&P_{z_{1,1}}^m \int_0^{2\pi} \cos(\mu\phi)\cos(\xi\phi)\sin\left(mN\phi + p_{0_{z_{1,1}}}^m\right) d\phi \\
&+P_{z_{1,2}}^m \int_0^{2\pi} \cos(\mu\phi)\sin(\xi\phi)\sin\left(mN\phi + p_{0_{z_{1,2}}}^m\right) d\phi \\
&+P_{z_{2,1}}^m \int_0^{2\pi} \sin(\mu\phi)\cos(\xi\phi)\sin\left(mN\phi + p_{0_{z_{2,1}}}^m\right) d\phi \\
&+P_{z_{2,2}}^m \int_0^{2\pi} \sin(\mu\phi)\sin(\xi\phi)\sin\left(mN\phi + p_{0_{z_{2,2}}}^m\right) d\phi. \quad \text{(A.6)}
\end{aligned}$$

By integrating these integrals, it yields that at least one of them is non-zero if μ, ξ, mN satisfy one the following conditions:

$$\begin{cases} mN + \mu - \xi = 0; \\ mN - \mu + \xi = 0; \\ mN + \mu + \xi = 0; \\ mN - \mu - \xi = 0. \end{cases} \quad \text{(A.7)}$$

The third condition is never satisfied since mN, μ, ξ are all positive; the second one can be only satisfied to high order core modes with $\mu > mN$, but they are of little practical interest. Thus, rewriting only the first and fourth conditions, it yields:

$$\xi = mN \pm \mu.$$

Following the same procedure for the other height terms of the radial and azimuthal components, with the only difference that $\tilde{n}_{int,ext}$ are now equal to 1, the same condition is obtained.

It is important to point out that the above condition has been obtained without hypothesis on the shape of the perturbation $\Delta\varepsilon$. The only condition is that $\Delta\varepsilon$ must be periodic.

Appendix B

Marcatili's formula for solid core tube fibers

Marcatili's formula has been widely used in the literature to describe the dispersion properties of the core mode of hollow core waveguides [54]. The main limitation of this formula is that it was developed assuming that the core is made of air ($n_L = n_{air} = 1$). In this appendix Marcatili's formula is extended to take into account also hollow core waveguides with a generic refractive index core.

Consider a circular waveguide of radius R and refractive index n_L embedded in an another dielectric medium of infinite extent and refractive index n_H. Here, for simplicity, both n_H and n_L are real and $n_L < n_H$. Owing to the geometry of the problem, a cylindrical coordinate system is assumed. Two propagation constants, K_τ ($\tau = \{L, H\}$) and β, can be defined: the former is directed along the transverse plane of the waveguide, while the latter along the axial one. These two constants satisfy the relation $K_0^2 n_\tau^2 = K_\tau^2 + \beta^2$, where $K_0 = 2\pi f/c$ is the propagation constant in free space. With these assumptions, it can be shown that the dispersion relation for the modes guided inside the internal cylinder satisfies [81]:

$$\left[\frac{J'_\nu(K_L R)}{J_\nu(K_L R)} - \frac{K_L}{K_H}\frac{H_\nu^{(1)\prime}(K_H R)}{H_\nu^{(1)}(K_H R)}\right]\left[\frac{J'_\nu(K_L R)}{J_\nu(K_L R)} - \frac{K_L}{K_H}\frac{n_H^2}{n_L^2}\frac{H_\nu^{(1)\prime}(K_H R)}{H_\nu^{(1)}(K_H R)}\right] = \left[\frac{\nu\beta}{K_L^2 R^2}\left(\frac{K_L^2}{K_H^2} - 1\right)\right]^2, \tag{B.1}$$

where $J_\nu(x)$ and $H_\nu^{(1)}(x)$ are the Bessel and Hankel functions of the first kind. Solving Eq. (B.1) means finding the propagation constants β of the guided modes. Two hypotheses can now be introduced to simplify calculations: first, the core radius is much bigger than the working wavelength (i.e. $K_0 R >> 1$) and, second, modes guided inside the internal cylinder have a propagation constant which is very close to that of the bulk material (i.e. $\beta \approx K_0 n_L$). Neglecting all powers of K_L/K_H greater than one, and introducing the following approximation:

$$\frac{H_\nu^{(1)\prime}(K_H R)}{H_\nu^{(1)}(K_H R)} \approx i, \tag{B.2}$$

it is possible to reduce Eq. (B.1) to the following form:

$$J_{\nu-1}(K_L R) = i \frac{\eta}{\sqrt{(\frac{n_H}{n_L})^2 - 1}} \frac{K_L}{K_0 n_L} J_\nu(K_L R), \tag{B.3}$$

where:

$$\eta = \begin{cases} \frac{1}{2}\left[1 + (\frac{n_H}{n_L})^2\right] & \text{for } HE_{\nu\mu} \text{ and } EH_{\nu\mu} \text{ modes} \\ 1 & \text{for } TE_{0\mu} \text{ modes} \\ (\frac{n_H}{n_L})^2 & \text{for } TM_{0\mu} \text{ modes} \end{cases} \tag{B.4}$$

Under the assumptions already made, the term on the right hand side of Eq. (B.3) is in general small. Therefore, a perturbation technique can be applied to solve Eq. (B.3) keeping only the first term of the perturbation obtaining [54]:

$$K_L \approx \frac{u_{\nu\mu}}{R}\left[1 - i\nu \frac{1}{K_0 n_L R} \frac{\eta}{\sqrt{(\frac{n_H}{n_L})^2 - 1}}\right], \tag{B.5}$$

where $u_{\nu,\mu}$ is the μ-th zero of the function $J_{\nu-1}(x)$. It is now straightforward to obtain propagation constants for the guided modes:

$$\beta = Re\left\{\sqrt{K_0^2 n_L^2 - K_L^2}\right\} \approx \frac{2\pi f}{c} n_L \left[1 - \frac{1}{2}\left(\frac{u_{\nu\mu} c}{2\pi f R n_L}\right)^2\right], \tag{B.6}$$

and then finally

$$n_{eff} = \frac{\beta}{K_0} = n_L - \frac{1}{2}\left(\frac{u_{\nu\mu} c}{2\pi f R \sqrt{n_L}}\right)^2. \tag{B.7}$$

Appendix C

$1/R_{CO}$ dependency of the propagation loss on fiber's scaling

In chapter 5 it has been shown that when a CTLF-CT is scaled according to the transformation proposed by Eq. (5.11), the propagation loss of the fundamental core mode scales as $1/R_{co}$. In order to understand the physical reason of this effect, a schematic representation of this transformation has been sketched in Fig. C.1. Here K_0 represents the free space wave vector defined as

$$K_0 = \frac{2\pi f}{c}, \tag{C.1}$$

whereas β is the wave vector along the propagation direction. In general, in waveguides analysis, their ratio is represented by the effective index n_{eff}, which satisfies:

$$n_{eff} = \frac{\beta}{K_0} = \cos(\theta). \tag{C.2}$$

Through this thesis it has been widely shown that the Marcatili's formula given by Eq. (2.2) represents a very good approximation for the effective index of the fundamental core mode. When the scaling transformation of Eq. (5.11) is taken into account, it is straightforward to show that the effective index of the

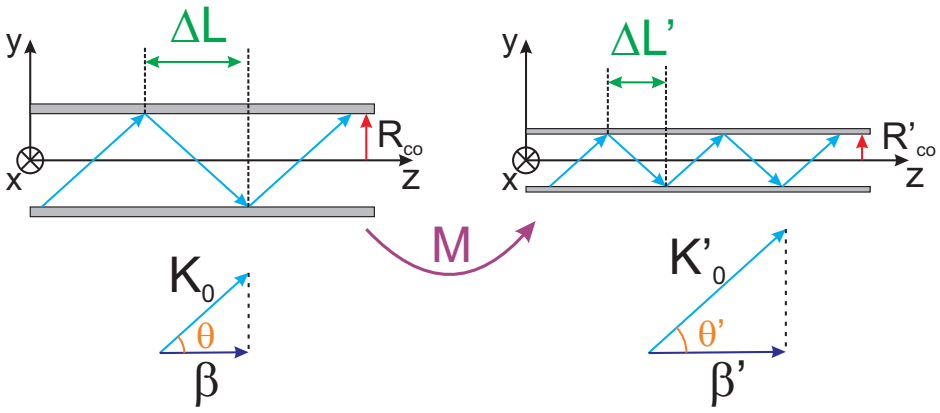

Figure C.1: Transverse section along the propagation direction of an ideal hollow core waveguide (left) and its scaled version (right) according to Eq. (5.11).

fundamental core mode is not affected by this change, which means:

$$n_{eff} = n'_{eff} \quad \rightarrow \quad \theta = \theta'. \tag{C.3}$$

Owing to the transformation, $R'_{co} = MR_{co}$, which means that the distance between two successive bounces on the cladding boundary is given by:

$$\Delta L' = \frac{R'_{co}}{\tan\theta'} = \frac{MR_{co}}{\tan\theta} = M\Delta L \tag{C.4}$$

Due to the non perfect reflection of the core mode upon the cladding boundary, after a traveled distance Δz, the electromagnetic radiation is reduced by a factor [44]:

$$e^{-\alpha\Delta z} = R(\theta)^{\Delta z/\Delta L}, \tag{C.5}$$

where $R(\theta)$ is the reflection coefficient at each bounce and it has been assumed to depend only on the angle but not on the frequency for simplicity. As a consequence, the leakage loss is given by:

$$\alpha = -\frac{1}{\Delta L}\frac{\ln\left[R(\theta)\right]}{\Delta z} \quad \rightarrow \quad \alpha \propto \frac{1}{\Delta L}. \tag{C.6}$$

It now straightforward to estimate the effect of the scaling on the leakage loss of the guided core mode:

$$\frac{\alpha}{\alpha'} = \frac{\Delta L'}{\Delta L} \quad \rightarrow \quad \alpha' = \frac{1}{M}\alpha, \tag{C.7}$$

which is exactly what it has been shown in Fig. 5.10.

Bibliography

[1] A. G. Davies, E. H. Linfield, and M. B. Johnston, "The development of terahertz sources and their applications," *Phys. Med. Biol.*, vol. 47, no. 21, pp. 3679–3689, 2002.

[2] G. P. Gallerano and S. Biedron, "Overview of terahertz radiation sources," in *Proceedings of the* 2004 *FEL conference*, pp. 216–221, 2004.

[3] C. Worrall, J. Alton, M. Houghton, S. Barbieri, H. E. Beere, D. Ritchie, and C. Sirtori, "Continuous wave operation of a superlattice quantum cascade laser emitting at 2 thz," *Opt. Expr.*, vol. 14, no. 1, pp. 171–181, 2006.

[4] A. A. Danylov, A. R. Light, J. Waldman, N. R. Erickson, X. Qian, and W. D. Goodhue, "2.32 thz quantum cascade laser frequencylocked to the harmonic of a microwave synthesizer source," *Opt. Expr.*, vol. 20, no. 25, pp. 27908–27914, 2012.

[5] P. U. Jepsen, R. H. Jacobsen, and S. R. Keiding, "Generation and detection of terahertz pulses from biased semiconductor antennas," *J. Opt. Soc. Am. B*, vol. 13, no. 11, pp. 2424–2435, 1996.

[6] D. Saeedkia, "Terahertz photoconductive antennas: Principles and applications," in *Antennas and Propagation (EUCAP), Proceedings of the 5th European Conference on*, pp. 3326–3328, april 2011.

[7] C. broadband terahertz generation with conventional laser diodes, "D. molter and a.wagner and s. weber and j. jonuscheit and r. beigang," *Opt. Expr.*, vol. 19, no. 6, pp. 5290–5296, 2011.

[8] N. Karpowicz, X. Lu, and X. C. Zhang, "Terahertz gas photonics," *J. Mod. Optic.*, vol. 56, no. 10, pp. 1137–1150, 2009.

[9] J. Dai, J. Liu, and X. C. Zhang, "Terahertz wave air photonics: terahertz wave generation and detection with laser-induced gas plasma," *J. Quantum Elect.*, vol. 17, no. 1, pp. 183–190, 2011.

[10] D. Jianming, X. Xiw, and X. C. Zhang, "Detection of broadband terahertz waves with a laser-induced plasma in gases," *Phys. Rev. Lett.*, vol. 97, p. 103903, 2006.

[11] H. Wu, H. Liu, N. Huang, Q. Sun, and J. Wen, "High-power picosecond terahertz-wave generation in photonic crystal fiber via four-wave mixing," *Appl. Opt.*, vol. 50, no. 27, pp. 5338–5343, 2011.

[12] D. D. Yavuz and J. J. Weber, "Tunable source of terahertz radiation using molecular modulation," *Opt. Lett.*, vol. 37, no. 20, pp. 4191–4193, 2012.

[13] M. Asada, S. Szuki, and N. Kishimoto, "Resonant tunneling diodes for sub-terahertz and terahertz oscillators," *Jap. Soc. Appl. Phys.*, vol. 47, no. 6, pp. 4375–4384, 2008.

[14] K. Ishigaki, M. Shiraishi, S. Suzuki, M. Asada, N. Nishiyama, and S. Arai, "Direct intensity modulation and wireless data transmission characteristics of terahertz-oscillating resonant tunnelling diodes," *Electronics Letters*, vol. 48, pp. 582–583, 10 2012.

[15] Y. Jin, G. Kim, and S. Jeon, "Terahertz dielectric properties of polymers," *J. Korean Phys. Soc.*, vol. 49, pp. 513–517, 2006.

[16] J. Anthony, R. Leonhardt, A. Argyros, and M. C. J. Large, "Characterization of a microstructured zeonex terahertz fiber," *J. Opt. Soc. Am. B*, vol. 28, no. 5, pp. 1013–1018, 2011.

[17] J. Anthony, R. Leonhardt, S. G. Leon-Saval, and A. Argyros, "Thz propagation in kagome hollow-core microstructured fibers," *Opt. Expr.*, vol. 19, no. 19, pp. 18470–18478, 2011.

[18] A. Tuniz, B. T. Kuhlmey, R. Lwin, A. Wang, J. Anthony, R. Leonhardt, and S. C. Fleming, "Drawn metamaterials with plasmonic response at terahertz frequencies," *Appl. Phys. Lett.*, vol. 96, no. 19, p. 191101, 2010.

[19] A. Argyros, R. Lwin, S. G. Leon-Saval, J. Poulin, L. Poladian, and M. C. J. Large, "Low loss and temperature stable microstructured polymer optical fibers," *J. Light. Tech.*, vol. 30, no. 1, pp. 192–197, 2012.

[20] K. Nielsen, H. K. Rasmussen, A. J. L. Adam, P. C. M. Planken, O. Bang, and P. U. Jepsen, "Bendable, low loss topas fibers for the terahertz frequency range," *Opt. Express*, vol. 17, no. 10, pp. 8592–8601, 2009.

[21] N. Laman and D. Grischkowsky, "Terahertz conductivity of thin metal films," *Appl. Phys. Lett.*, vol. 93, Aug 2008.

[22] M. A. Ordal, L. L. Long, R. J. Bell, S. E. Bell, R. R. Bell, J. R. W. Alexander, and C. A. Ward, "Optical properties of the metals Al, Co, Cu, Au, Fe, Pb, Ni, Pd, Pt, Ag, Ti, and W in the infrared and far infrared," *Appl. Opt.*, vol. 22, pp. 1099–1119, Apr 1983.

[23] D. M. Pozar, *Microwave engineering*. Wiley, third ed., 2005.

[24] R. Mendis and D. Grischkowsky, "Undistorted guided-wave propagation of subpicosecond terahertz pulses," *Opt. Lett.*, vol. 26, pp. 846–848, Jun 2001.

[25] M. Mbonye, R. Mendis, and D. M. Mittleman, "Inhibiting the te_1-mode diffraction losses in terahertz parallel-plate waveguides using concave plates," *Opt. Expr.*, vol. 20, no. 25, pp. 27800–27809, 2012.

[26] K. Wang and D. M. Mittleman, "Guided propagation of terahertz pulses on metal wires," *J. Opt. Soc. Am. B*, vol. 22, no. 9, pp. 2001–2008, 2005.

[27] T. E. H. Pahlevaninezhad, Darcie, and B. Heshmat, "Two-wire waveguide for terahertz," *Opt. Expr.*, vol. 18, no. 7, pp. 7415–7420, 2010.

[28] J. Anthony, R. Leonhardt, and A. Argyros, "Thz guidance in hybrid hollow core fibers with embedded indium wires," in *IRMMW-THz, Wollongong, Australia*, Sept 2012.

[29] A. Markov, S. Gorgutsa, H. Qu, and M. Skorobogatiy, "Practical metal-wire thz waveguides," *ArXiv e-prints*, June 2012.

[30] T. I. Jeon, J. Zhang, and D. Grischkowsky, "Thz sommerfeld wave propagation on a single metal wire," *Appl. Phys. Lett.*, vol. 86, no. 16, p. 161904, 2005.

[31] M. Mbonye, R. Mendis, and D. M. Mittleman, "A terahertz two-wire waveguide with low bending loss," *Appl. Phys. Lett.*, vol. 95, no. 23, p. 233506, 2009.

[32] S. Atakaramians, S. A. Vahid, B. M. Fischer, H. Ebendorff-Heidepriemb, T. Monro, and D. Abbott, "Microwire fibers for low loss thz transmission," *Proc. of SPIE*, vol. 6414, no. 64140I, 2007.

[33] M. Rozé, B. Ung, A. Mazhorova, M. Walther, and M. Skorobogatiy, "Suspended core subwavelength fibers: towards practical designs for low-loss terahertz guidance," *Opt. Expr.*, vol. 19, pp. 9127–9138, May 2011.

[34] S. Atakaramians, S. A. V., H. Ebendorff-Heidepriem, M. Nagel, B. M. Fischer, D. Abbott, and T. M. Monro, "Thz porous fibers: design, fabrication and experimental characterization," *Opt. Expr.*, vol. 17, pp. 14053–15062, Aug 2009.

[35] S. Atakaramians, S. A. V., B. M. Fischer, D. Abbott, and T. M. Monro, "Porous fibers: a novel approach to low loss thz waveguides," *Opt. Expr.*, vol. 16, pp. 8845–8854, Jun 2008.

[36] F. Couny, F. Benabid, P. J. Roberts, P. S. Light, and M. G. Raymer, "Generation and photonic guidance of multi-octave optical-frequency combs," *Science*, vol. 318, pp. 118–121, 2007.

[37] T. Birks, P. Roberts, P. Russell, D. Atkin, and T. Shepherd, "Full 2-d photonic bandgaps in silica/air structures," *Elect. Lett.*, vol. 31, no. 22, pp. 1941–1943, 1995.

[38] R. F. Cregan, B. J. Mangan, J. C. Knight, T. A. Birks, P. S. J. Russell, P. J. Roberts, and D. C. Allan, "Single-mode photonic band gap guidance of light in air," *Science*, vol. 285, no. 5433, pp. 1537–1539, 1999.

[39] A. Dupuis, K. Stoeffler, B. Ung, C. Dubois, and M. Skorobogatiy, "Transmission measurements of hollow-core thz bragg fibers," *J. Opt. Soc. Am. B*, vol. 28, no. 4, pp. 896–907, 2011.

[40] Z. Wu, W. R. Ng, M. E. Gehm, and H. Xin, "Terahertz electromagnetic crystal waveguide fabricated by polymer jetting rapid prototyping," *Opt. Expr.*, vol. 19, no. 5, pp. 3962–3972, 2011.

[41] P. Doradla, C. S. Joseph, J. Kumar, and R. H. Giles, "Characterization of bending loss in hollow flexible terahertz weaveguides," *Opt. Express*, vol. 20, no. 17, pp. 19176–19184, 2012.

[42] E. Nguema, D. Fèrachou, G. Humbert, J. L. Auguste, and J. M. Blondy, "Broadband terahertz transmission within the air channel of thin-wall pipe," *Opt. Lett.*, vol. 36, no. 10, pp. 1782–1784, 2011.

[43] J. T. Lu, C. H. Lai, T. F. Tseng, H. Chen, Y. F. Tsai, I. J. Chen, Y. J. Hwang, H. C. Chang, and C. K. Sun, "Terahertz polarization-sensitive rectangular pipe waveguides," *Opt. Express*, vol. 19, no. 22, pp. 21532–21539, 2011.

[44] C. H. Lai, B. You, J. Y. Lu, T. A. Liu, J. L. Peng, C. K. Sun, and H. C. Chang, "Modal characteristics of antiresonant reflecting pipe waveguides for terahertz waveguiding," *Opt. Express*, vol. 18, no. 1, pp. 309–322, 2010.

[45] C. S. Ponseca Jr., R. Pobre, E. Estacio, N. Sarukura, A. Argyros, M. C. J. Large, and M. A. van Eijkelenborg, "Transmission of terahertz radiation using microstructured polymer optical fiber," *Opt. Lett.*, vol. 33, no. 9, pp. 902–904, 2008.

[46] D. S. Wu, A. Argyros, and S. G. Leon-Saval, "Reducing the size of hollow terahertz waveguides," *J. Lightwave Technol.*, vol. 29, no. 1, 2011.

[47] Y. Y. Wang, N. V. Wheeler, F. Couny, P. J. Roberts, and F. Benabid, "Low loss broadband transmission in hypocycloid-core kagome hollow-core photonic crystal fiber," *Opt. Lett.*, vol. 36, no. 5, pp. 669–671, 2011.

[48] A. Argyros and J. Pla, "Hollow-core polymer fibres with a kagome lattice: potential for transmission in the infrared," *Opt. Express*, vol. 15, no. 12, pp. 7713–7719, 2007.

[49] A. Argyros, S. G. Leon-Saval, J. Pla, and A. Docherty, "Antiresonance and inhibited coupling in hollow core square lattice optical fibres," *Opt. Expr.*, vol. 16, no. 8, pp. 5642–5648, 2008.

[50] F. Couny, P. J. Roberts, T. A. Birks, and F. Benabid, "Square-lattice large-pitch hollow-core photonic crystal fiber," *Opt. Express*, vol. 16, no. 25, pp. 20626–20636, 2008.

[51] A. D. Pryamikov, A. S. Biriukov, A. F. Kosolapov, V. G. Plotnichenko, S. L. Semjonov, and E. M. Dianov, "Demonstration of a waveguide regime for a silica hollow-core microstructured optical fiber with a negative curvature of the core boundary in the spectral region $> 3.5\mu m$," *Opt. Expr.*, vol. 19, no. 2, pp. 1441–1448, 2011.

[52] J. Lu, C. Yu, H. Chang, H. Chen, Y. Li, C. Pan, , and C. Sun, "Terahertz air-core microstructure fiber," *Appl. Phys. Lett.*, vol. 92, no. 6, p. 64105, 2008.

[53] M. Kharadly and J. Lewis, "Properties of dielectric-tube waveguides," *Proc. IEE*, vol. 116, no. 2, pp. 214–224, 1969.

[54] E. A. J. Marcatili and R. A. Schmeltzer, "Hollow metallic and dielectric waveguides for long distance optical transmission and lasers," *Bell Syst. Tech. J.*, vol. 43, pp. 1973–1809, 1964.

[55] L. Vincetti, V. Setti, and M. Zoboli, "Terahertz tube lattice fibers with octagonal symmetry," *Photon. Techn. Lett.*, vol. 22, no. 13, pp. 972–974, 2010.

[56] L. Vincetti and V. Setti, "Waveguiding mechanism in tube lattice fibers," *Opt. Expr.*, vol. 18, no. 22, pp. 23133–23146, 2010.

[57] L. Vincetti and V. Setti, "Fano resonances in polygonal tube fibers," *J. Lightw. Tech.*, vol. 30, no. 1, pp. 31–37, 2012.

[58] L. Vincetti and V. Setti, "Confinement loss in kagome and tube lattice fibers: comparison and analysis," *J. Lightw. Techn.*, vol. 30, no. 10, pp. 1470–1474, 2012.

[59] L. Vincetti and V. Setti, "Extra loss due to fano resonances in inhibited coupling fibers based on lattice of tubes," *Opt. Expr.*, vol. 20, no. 13, pp. 14350–14361, 2012.

[60] L. Vincetti and V. Setti, "Elliptical hollow core tube lattice fibers for terahertz applications," *Opt. Fiber. Tech.*, vol. 19, no. 1, pp. 31–34, 2013.

[61] V. Setti, L. Vincetti, and A. Argyros, "Flexible tube lattice fibers for terahertz applications," *in press on Opt. Expr.*, 2013.

[62] V. Setti, L. Vincetti, and A. Argyros, "Bending loss in tube lattice fibers for terahertz applications," *IRMMW-THz, University of Wollongong, Wollongong, NSW, Australia,* $23-28$ *September*, 2012.

[63] A. Argyros, V. Setti, J. Anhtony, L. Vincetti, and R. Leonhardt, "Polymer and polymer-metal microstructured waveguides for thz radiation," *ETOPIM, Marseille, France,* $2-7$ *September*, 2012.

[64] L. Vincetti, V. Setti, and M. Zoboli, "Fano resonances in kagome fibers," *SPIE Europe, Square Brussels Meeting Centre, Brussels, Belgium,* $16-19$ *April*, 2012.

[65] L. Vincetti, V. Setti, and M. Zoboli, "Elliptical tube waveguides," *SPIE Europe, Square Brussels Meeting Centre, Brussels, Belgium,* $16-19$ *April*, 2012.

[66] L. Vincetti, V. Setti, and M. Zoboli, "Analysis of the confinement loss in kagome fibers," *Progress in Electromagnetic Research Symposium (PIERS), Kuala Lumpur, Malaysia,* $27-30$ *March*, 2012.

[67] L. Vincetti, V. Setti, and M. Zoboli, "Birefringence in elliptical tube fibers," *Progress in Electromagnetic Research Symposium (PIERS), Kuala Lumpur, Malaysia,* $27-30$ *March*, 2012.

[68] L. Vincetti, V. Setti, and M. Zoboli, "Confinement loss of tube lattice and kagome fibers," *Specialty Opticals Fibers (SOF), Toronto, Canada,* $12-16$ *June*, 2011.

[69] L. Vincetti, V. Setti, and A. Polemi, "Propagating and radiating properties of broadband hollow core fibers in terahertz spectral region," *European Conference on Antennas and Propagation (EuCAP), Barcelona, Spain,* $12-16$ *April*, 2010.

[70] L. Vincetti, V. Setti, and M. Zoboli, "Optimization of the core-cladding interface in kagome fibers," *Fotonica, Pisa, Firenze, May* $15-17$, 2012.

[71] L. Vincetti, V. Setti, and M. Zoboli, "Elliptical hollow core fibers for terahertz applications," *Fotonica, Pisa, May* $15-17$, 2012.

[72] L. Vincetti, V. Setti, and M. Zoboli, "Analysis of the waveguiding mechanism in tube lattice fibers," *XVIII Riunione Nazionale di Elettromagnetismo (RiNEm), Benevento, September* $6-10$, 2010.

[73] L. Vincetti, V. Setti, and M. Zoboli, "Fibre ottiche a nucleo cavo con simmetria ottagonale per applicazioni terahertz," *Fotonica, Pisa, May* $25-27$, 2010.

[74] S. Février, F. Gérôme, A. Labruyère, B. Beaudou, G. Humbert, and J.-L. Auguste, "Ultraviolet guiding hollow-core photonic crystal fiber," *Opt. Lett.*, vol. 34, no. 19, pp. 2888–2890, 2009.

[75] S. Février, B. Beaudou, and P. Viale, "Understanding origin of loss in large pitch hollow-core photonics crystal fibres and their design simplification," *Opt. Express*, vol. 18, no. 5, pp. 5142–5150, 2010.

[76] G. J. Pearce, G. S. Wiederhecker, C. G. Poulton, S. Burger, and P. S. Russell, "Models for guidance in kagome-structured hollow-core photonic crystal fibres," *Opt. Express*, vol. 15, no. 20, pp. 12680–12685, 2007.

[77] L. Chen, G. J. Pearce, T. A. Birks, and D. M. Bird, "Guidance in kagome-like photonic crystal fibres i: analysis of an ideal fibre structure," *Opt. Express*, vol. 19, no. 7, pp. 6945–6956, 2011.

[78] L. Chen and D. M. Bird, "Guidance in kagome-like photonic crystal fibres ii: perturbation theory for a realistic fibre structure," *Opt. Express*, vol. 19, no. 7, pp. 6957–6968, 2011.

[79] S. Selleri, L. Vincetti, A. Cucinotta, and M. Zoboli, "Complex fem modal solver of optical waveguides with pml boundary conditions," *Opt. Quant. Elect.*, vol. 33, no. 4-5, pp. 359–371, 2001.

[80] D. Chen and H. Chen, "A novel low-loss terahertz waveguide: Polymer tube," *Opt. Express*, vol. 18, no. 4, pp. 3762–3767, 2010.

[81] J. A. Stratton, *Electromagnetic theory*. McGraw Hill, 1941. section 9.15.

[82] K. Saitoh, N. Mortensen, and M. Koshiba, "Air-core photonic band-gap fibers: the impact of surface modes," *Opt. Express*, vol. 12, no. 3, pp. 394–400, 2004.

[83] P. L. François and C. Vassallo, "Finite cladding effects in w fibers: a new interpretation of leaky modes," *Applied Optics*, vol. 22, no. 19, pp. 3109–3120, 1983.

[84] F. Benabid, P. J. Roberts, F. Couny, and P. S. Light, "Light and gas confinement in hollow-core photonic crystal fibre based photonic microcells," *J. Eur. Opt. Soc.*, vol. 4, no. 09004, 2009.

[85] L. Vincetti, "Numerical analysis of plastic hollow core microstructured fiber for terahertz applications," *Opt. Fiber Tech.*, vol. 15, no. 4, pp. 398–401, 2009.

[86] T. Grujic, B. T. Kuhlmey, A. Argyros, S. Coen, and M. de Sterke, "Solid-core fiber with ultra-wide bandwidth transmission window due to inhibited coupling," *Opt. Express*, vol. 18, no. 25, pp. 25556–25566, 2010.

[87] J. M. Stone, G. J. Pearce, F. Luan, T. A. Birks, J. C. Knight, A. K. George, and D. M. Bird, "An improved photonic bandgap fiber based on an array of rings," *Opt. Expr.*, vol. 14, no. 13, pp. 6291–6296, 2006.

[88] P. Steinvurzel, C. M. de Sterke, M. K. Steel, B. T. Kuhlmey, and B. J. Eggleton, "Single scatterer fano resonances in solid core photonic band gap fibers," *Opt. Expr.*, vol. 14, no. 19, pp. 8797–8811, 2006.

[89] L. Vincetti, "Single-mode propagation in triangular tube lattice hollow-core terahertz fibers," *Opt. Commun.*, vol. 283, no. 6, pp. 979–984, 2010.

[90] J. Fini, "Design of solid and microstructure fibers for suppression of higher-order modes," *Opt. Express*, vol. 13, no. 9, pp. 3477–3490, 2005.

[91] K. Saitoh, N. Florous, T. Murao, and M. Koshiba, "Design of photonic band gap fibers with suppressed higher-order modes: Towards the development of effectively single mode large hollow-core fiber platforms," *Opt. Express*, vol. 14, no. 16, pp. 7342–7352, 2006.

[92] M. Naftaly and R. E. Miles, "Terahertz time-domain spectroscopy for material characterization," *Proc. IEEE*, vol. 95, no. 8, p. 16581665, 2007.

[93] M. Goto, A. Quema, H. Takahashi, S. Ono, and N. Sarukura, "Teflon photonic crystal fiber as terahertz waveguide," *Jpn. J. Appl. Phys.*, vol. 43, no. 2B, pp. 317–319, 2004.

[94] J. R. Birch, J. D. Dromey, and J. Lesurf, "The optical constants of some common low-loss polymers between 4 and 40 cm^{-1}," *Infrared Phys.*, vol. 21, no. 4, pp. 225–228, 1981.

[95] C. Winnewisser, F. Lewen, and H. Helm, "Transmission characteristics of dichroic filters measured by thz time-domain spectroscopy," *Appl. Phys.*, vol. 66, no. 6, pp. 593–598, 1998.

[96] L. Dong, B. K. Thomas, S. Suzuki, and L. Fu, "Extending transmission bandwidth of air-core photonic bandgap fibers," *Opt. Fiber Tech.*, vol. 16, no. 6, pp. 442–448, 2010.

[97] A. F. Kosolapov, A. D. Pryamikov, A. S. Biriukov, V. S. Shiryaev, M. S. Astapovich, G. E. Snopatin, V. G. Plotnichenko, M. F. Churbanov, and E. M. Dianov, "Demonstration of CO_2-laser power delivery through chalcogenide-glass fiber with negative-curvature hollow core," *Opt. Expr.*, vol. 19, no. 25, pp. 25723–25728, 2011.

[98] F. Poletti, J. R. Hayes, and D. J. Richardson, "Low loss antiresonant hollow core fibres," in *Specialty Optical Fibers*, p. SOWB1, 2011.

[99] X. Jiang, T. G. Euser, A. Abdolvand, F. Babic, F. Tani, N. Y. Joly, J. C. Travers, and P. S. J. Russel, "Single-mode hollow-core photonic crystal fiber made from soft glass," *Opt. Expr.*, vol. 19, no. 16, pp. 15438–15444, 2011.

[100] S. Johnson, M. Ibanescu, M. Skorobogatiy, O. Weisberg, T. Engeness, M. Soljacic, S. Jacobs, J. Joannopoulos, and Y. Fink, "Low-loss asymptotically single-mode propagation in large-core omniguide fibers," *Opt. Express*, vol. 9, no. 13, pp. 748–779, 2001.

[101] P. J. Roberts, F. Benabid, F. Couny, and P. S. Light, "Dispersion properties of kagome hollow-core fibers," in *Proc. CLEO*, May 4-9, 2008.

[102] U. Fano, "Effects of configuration interaction on intensities and phase shifts," *Phys. Rev.*, vol. 24, no. 6, pp. 1866–1878, 1961.

[103] S. Glasberg, A. Sharon, D. Rosenblatt, and A. A. Friesem, "Spectral shifts and line-shapes asymmetries in the resonant response of grating waveguide structures," *Opt. Comm.*, vol. 145, pp. 291–299, 1998.

[104] S. S. Wang, R. Magnusson, J. Bagby, and M. G. Moharam, "Guided-mode resonances in planar dielectric-layer diffraction gratings," *J. Opt. Soc. Am. A*, vol. 7, no. 8, pp. 1470–1474, 1990.

[105] S. Fan, W. Suh, and J. D. Joannopoulos, "Temporal coupled-mode theory for the fano resonance in optical resonators," *J. Opt. Soc. Am. A*, vol. 20, no. 3, pp. 569–572, 2002.

[106] S. Fan and J. D. Joannopoulos, "Analysis of guided resonances in photonic crystal slabs," *Phys. Rev. B*, vol. 65, 2002.

[107] S. L. Chuang, "A coupled mode formulation by reciprocity and a variational principle," *J. Lightw. Technol.*, vol. 5, no. 1, pp. 5–15, 1987.

[108] W. Huang and J. Mu, "Complex coupled-mode theory for optical waveguides," *Opt. Express*, vol. 17, no. 21, pp. 19134–19152, 2009.

[109] A. B. Manenkov, "Quasi optics of waveguides with selective reflecting dielectric walls," *Proc. of the Fifth Colloquim on Microwave Communications, Budapest, Hungary*, June 1974.

[110] P. Yeh, A. Yariv, and E. Marom, "Theory of bragg fiber," *J. Opt. Soc. Am.*, vol. 68, no. 9, pp. 1196–1201, 1978.

[111] S. Henry, R. C. L.M. Zurk, and P. Hanaway, "Measurement and modeling of dielectric tube waveguides for terahertz pulses," in *Proc. of SPIE*, 2009.

[112] K. J. Rowland, S. A. V., and T. M. . Monro, "Bandgaps and antiresonances in integrated-arrows and bragg fibers; a simple model," *Opt. Express*, vol. 16, no. 22, pp. 17935–17951, 2008.

[113] N. M. Litchinitser, S. C. Dunn, B. Usner, B. J. Eggleton, T. P. White, R. C. McPhedran, and C. M. de Sterke, "Resonances in microstructured optical waveguides," *Opt. Express*, vol. 11, no. 10, pp. 1243–1251, 2003.

[114] M. Skorobogatiy, M. Ibanescu, S. G. Johnson, O. Wiesberg, T. D. Engeness, M. Soljacic, S. A. Jacobs, and Y. Fink, "Analysis of general geometric scal-

ing perturbations in a transmitting waveguide: fundamental connection between polarization-mode dispersion and grou-velocity dispersion," *J. Opt. Soc. Am. B*, vol. 19, no. 12, pp. 2867–2875, 2002.

[115] B. T. Kuhlmey, K. Pathmanandavel, and R. C. McPhedran, "Multipole analysis of photonic crystal fibers with coated inclusions," *Opt. Expr.*, vol. 14, no. 22, pp. 10851–10864, 2006.

[116] G. Ren, Y. Gong, P. Shum, X. Yu, J. Hu, G. Wang, M. O. L. Chuen, and V. Paulose, "Low-loss air-core polarization maintaining terahertz fiber," *Optics Express*, vol. 16, no. 18, pp. 13593–13598, 2008.

[117] M. Cho, J. Kim, H. Park, Y. Han, K. Moon, E. Jung, and H. Han, "Highly birefringence terahertz polarization maintaining plastic photonic crystal fibers," *Opt. Express*, vol. 16, no. 1, pp. 7–12, 2008.

[118] M. C. Beard, G. M. Turner, and C. A. Schmuttenmaer, "Terahertz spectroscopy," *J. Phys. Chem.*, vol. 106, no. 29, pp. 7146–7159, 2002.

[119] B. Beaudou, F. Gerome, Y. Wang, M. Alharbi, T. Bradley, G. Humbert, J. L. Auguste, J. M. Blondy, and F. Benabid, "Milli-joule laser pulse delivery for spark ignition through kagome fiber," in *CLEO*, p. CM3N.4, 2012.

[120] Y. Y. Wang, X. Peng, M. Alharbi, C. F. Dutin, T. D. Bradley, F. Gérôme, M. Mielke, T. Booth, and F. Benabid, "Design and fabrication of hollow-core photonic crystal fibers for high-power ultrashort pulse transportation and pulse compression," *Opt. Lett.*, vol. 37, no. 15, pp. 3111–3113, 2012.

[121] J. Olszewski, M. Szpulak, and W. Urbańczyk, "Effect of coupling between fundamental and cladding modes on bending losses in photonic crystal fibers," *Opt. Express*, vol. 13, no. 16, pp. 6015–6022, 2005.

[122] F. Gérôme, R. Jamier, J. L. Auguste, G. Humbert, and J. M. Blondy, "Simplified hollow-core photonic crystal fiber," *Opt. Lett.*, vol. 35, no. 8, pp. 1157–1159, 2010.

[123] A. D. Pryamikov, A. F. Kosolapov, V. G. Plotnichenko, and E. M. Dianov, *Transmission of CO2 laser radiation through class hollow core microstructured fibers*, ch. 8, pp. 227–247. InTech, 2012.

[124] F. Yu, W. J. Wadsworth, and J. C. Knight, "Low loss silica hollow core fibers for $3-4\ \mu m$ spectral region," *Opt. Express*, vol. 20, no. 10, pp. 11153–11158, 2012.

[125] M. Miyagi and S. Kawakami, "Losses and phase constant changes caused by bends in the general class of hollow waveguides for the infrared," *Appl. Opt.*, vol. 20, no. 24, pp. 4221–4226, 1981.